DEVELOPMENT OF FIBER BRAGG GRATING BASED NOVEL ALL-OPTICAL SENSORS FOR STRUCTURAL HEALTH MONITORING

A Thesis Submitted

in Partial Fulfillment of the Requirements for the Degree of

DOCTOR OF PHILOSOPHY

by

DEBABRATA PAUL

(Roll no: 186121009)

Supervisor:

Prof. Sunil K. Khijwania

Department of Physics

Indian Institute of Technology Guwahati

Guwahati-781039, Assam, India

Dedicated to my baba and maa

STATEMENT

I hereby declare that the research work presented in this thesis entitled "**DEVELOPMENT OF FIBER BRAGG GRATING BASED NOVEL ALL-OPTICAL SENSORS FOR STRUCTURAL HEALTH MONITORING**", is carried out by me under the supervision of **Prof. Sunil K. Khijwania**, Professor, Department of Physics, Indian Institute of Technology Guwahati. The contents of this thesis have not been submitted to any other institute or university for the award of any degree.

Date ……..

Debabrata Paul
(186121009)

Research Scholar
Department of Physics
Indian Institute of Technology Guwahati
Guwahati-781039, Assam
India

CERTIFICATE

This is to certify that work contained in the thesis entitled "**DEVELOPMENT OF FIBER BRAGG GRATING BASED NOVEL ALL-OPTICAL SENSORS FOR STRUCTURAL HEALTH MONITORING**", by Mr. Debabrata Paul (Roll no: 186121009), a student of Department of Physics, Indian Institute of Technology Guwahati, for the award of degree of Doctor of Philosophy, has been carried out under my supervision. The contents of this thesis have not been submitted to any other institute or university for the award of any degree.

Date ……..

Prof. Sunil K. Khijwania

Professor, Department of Physics
Indian Institute of Technology Guwahati
Guwahati-781039, Assam
India

ACKNOWLEDGEMENTS

First and foremost, I would like to express my sincere gratitude to my respected supervisor, **Prof. Sunil K. Khijwania** for providing me the opportunity to work under his supervision. He has supported me throughout my research journey with his knowledge, invaluable guidance, continuous support, and encouragement. Beyond his mentorship, I deeply admire him as an exemplary teacher and physicist, whose dedication to knowledge and teaching has been a great source of inspiration for me.

I am also immensely grateful to my Doctoral Committee (DC) members, **Prof. A. Srinivasan**, **Prof. Gagan Kumar** and **Dr. Amit Shelke**, for their valuable time, constructive feedback, and insightful discussions that helped refine my research at every stage. I would also like to sincerely thank **Prof. Subhaditya Bhattacharya**, whose constant support, encouragement, and guidance have been invaluable throughout my journey.

I am deeply grateful to all the members in Fiber Optics lab (Dr. Sunil Mohan, Manish Singh Negi, Fatima Banoo and Subham Koley), for their constant help, insightful academic discussions, and the enthusiasm they brought to our academic interactions. Their support and collaboration have made this journey more enriching. Beyond academics, their companionship and unwavering support have helped me overcome challenges and stay motivated during difficult times. I would also like to thank all my colleagues and friends in the Department of Physics, Indian Institute of Technology Guwahati, for their insightful discussions, encouragement, and support during this journey.

My heartfelt appreciation goes to my family, for their unconditional love, sacrifices, encouragement, emotional support, and unwavering belief in me. Without their faith and support, this journey would not have been possible.

Amidst the equations, experiments, and endless research challenges, there has been one constant companion in my journey—**the game of cricket**. In my toughest times, it became my escape, my reset button. The sound of bat meeting ball, the competitions on the field, the endless plannings, and the rhythm of the game reminded me why I must keep playing—both in cricket and in my journey.

In the grand test match of life, this thesis is just one inning, and the game goes on.

ABSTRACT

This thesis focuses on the development of novel all-optical Fiber Bragg Grating (FBG)-based tilt and liquid level sensors, which are crucial for structural health monitoring (SHM). The primary objective is to create sensors with high sensitivity, superior angular resolution, and minimal measurement discrepancies while ensuring reversibility and temperature insensitivity for real-field applications. The novelty of this research lies in the innovative sensor designs that combine tunable response characteristics with inherent temperature insensitivity. Initially, a novel, all-optical, temperature-insensitive non-pendulum type FBG-based tilt sensor is developed. This sensor allows tuning of its response characteristics through variable loaded mass. The modulation of wavelength separation between two FBGs in response to applied tilt inherently eliminates temperature sensitivity. The sensor demonstrates excellent sensitivity (0.0300 nm/°), high accuracy (±0.033°), minimal discrepancy (±0.001 nm) and angular resolution (0.067°), with experimental results aligning closely with theoretical predictions. To further enhance performance, another innovative design strategy to achieve temperature-insensitive, FBG-based tilt sensor is proposed, featuring improved sensitivity (0.0415 nm/°) across dynamic range of ±10°. This design also offers tunable response characteristics via adjustable mass, achieving high accuracy (±0.024°), minimal deviation (±0.001 nm), and superior angular resolution of 0.012°. The sensor exhibits high degree of reversibility along with high repeatability and reliability across its operational range. Advancing the design further, another novel, temperature-insensitive FBG-based tilt sensor is developed, achieving remarkable sensitivity (0.3198 nm/°), outstanding accuracy (±0.0031°), minimal discrepancy (±0.001 nm), and exceptional angular resolution (0.0016°). This sensor also offers tunable response characteristics, with experimental results validating its high reversibility. The novelty here is in the simplified design that achieves superior performance without any compromise. In the next step, an etched FBG (EFBG) based temperature-insensitive, simple, all-optical

novel tilt sensor design is proposed. The sensor works by exploiting the effective refractive index (RI) sensitivity of an EFBG in order to achieve intensity modulation of the FBG spectrum. This scheme is used for tilt sensing for the first time to the best of author's knowledge. The sensor achieves a theoretical sensitivity of 1.20 dB/°, which is further enhanced to 2.41 dB/° in an improved design. Both sensors effectively measure the magnitude and direction of tilt within a ±10° range, demonstrating excellent reliability and temperature insensitivity. The innovative use of effective RI sensitivity introduces a new dimension in tilt sensing technology. In the final phase, an all-optical FBG-based temperature-insensitive liquid level sensor utilizing Archimedes' principle is developed to deliver high sensitivity (77.5 pm/cm) and high resolution (0.006 cm). This sensor exhibits minimal discrepancy (±0.01 nm) across a 30 cm dynamic range and exceptional accuracy (<0.03% FSR). This sensor offers tunable response characteristics, with experimental results validating its high reliability and reversibility. The novelty of this design lies in its application of buoyancy principles to achieve precise and reliable liquid level measurements. Overall, this research successfully presents advanced, high-performance all-optical FBG-based sensors for tilt and liquid level measurements, significantly contributing to the field of structural health monitoring through innovative design strategies and novel sensing mechanisms.

List of Contents

List of Figures

List of Tables

List of Abbreviation

DWDM	Dense wavelength-division multiplexing
EM	Eletro-magnetic
EMI	Electromagnetic interference
FBG	Fiber Bragg grating
FSR	Full scale reading
HF	Hydrofluric
HP	Horizontal Plate
ICC	Information-carrying capacity
LDV	Laser Doppler vibrometer
LPG	Long period grating
MEMS	Micro-electromechanical systems
OFS	Optical fiber sensors
RF	Radio-frequency
RHS	Right hand side
RI	RI
SHM	Structural health monitoring
SMF	Single mode fiber
STU	Strain tuning unit
TDM	Time-division multiplexing
UV	Ultraviolet
VP	Vertical Plate

List of Symbols

$\hbar$	Reduced Planck constant
ω	Angular frequency
β	Propagation constant
K	Grating wave-vector
Λ	Grating Pitch
λ_B	Bragg wavelength
n_{eff}	Effective RI
ϵ	Longitudinal strain
P_e	Photo-elastic coefficient
α	Thermal expansion coefficient
ξ	Thermo-optic coefficient
τ	Torque
κ	Coupling coefficient

Chapter 1 : Introduction and Literature Review

Sensors facilitate the acquisition of valuable information about various parameters, which are very crucial for controlling and monitoring industrial, scientific, and environmental processes. Effective control of these processes depends on acquiring information about specific parameters, which is made possible through the employment of appropriate sensing devices, known as sensors. The word “sensor” originates from the Latin word “sentire”, which broadly translates to “perceive”. By definition, a sensor is a device that converts a change in the magnitude of one physical parameter into a corresponding shift in the magnitude of another parameter, which can be measured more conveniently and much accurately [1]. Extensive research over the past decades has focused on developing ultra-precise, reversible, and repeatable sensors for diverse applications. Nowadays, millions of sensors are deployed worldwide, and it is hard to imagine any area of engineering that does not utilize sensing technology.

The origin of sensor can be traced to nature. There are various elements in nature that respond inherently to certain external perturbations. For example, the volume of mercury changes with temperature variations due to its inherent thermal expansion coefficient, while certain naturally magnetic ores align in response to magnetic fields, due to their inherent magnetic properties. In conventional/traditional sensors, these inherent properties of materials are exploited, which leads to unique response characteristics when external perturbation is applied. Apart from these, various other inherent properties of specific materials are also exploited by the conventional/traditional sensors. For example, there are strain gauges that utilize piezoelectric effects where piezo-resistors adjust resistance in response to strain. Additionally, piezoelectric materials generate a voltage when pressure is applied, forming the basis of conventional pressure sensors. Another example of conventional sensors is capacitive

sensors, that measure changes in capacitance when exposed to various external parameters such as humidity [2], strain [3], acceleration [4] etc. While these conventional/traditional sensors offer high precision and sensitivity, they come with certain significant drawbacks. Their performance is heavily dependent on surrounding conditions; i.e., they perform well under specific conditions but their performance is hampered drastically in the presence of strong environmental electromagnetic (EM) or radio-frequency (RF) signals. Additionally, they are practically ineffective in hazardous environments and lack multiplexing and remote sensing capabilities. These limitations cause them to fall short of expectations from the point of view of real-field application. Furthermore, these limitations have driven a search for alternative technologies that offer high sensitivity, long-lasting durability, immunity to interference, functionality in hazardous environments, and support for remote monitoring and multiplexing, paving the way for advanced sensor innovations.

One potential way to overcome these shortcomings is to shift sensing to the optical domain. Here, being optical in nature, the sensing signal (light-wave) is completely unaffected by surrounding electromagnetic (EM) radiation, thereby immediately addressing several drawbacks of conventional sensors. Optical sensors measure variations in a given parameter by accurately mapping them to changes in optical characteristics such as intensity, wavelength, or phase of the light-wave. Since, the first optical sensor reported in 1930 [5], various other optical sensors were developed by exploiting intensity variation through external parameter induced absorption of the optical signal. Highly precise optical sensors have been proposed for detecting chemical and gas concentrations. In these applications, fluorescence characteristics of specific dyes are utilized to detect gases like CO_2 and O_2 [6], [7]. In another research, laser Doppler vibrometer (LDV) has been demonstrated to accurately measure the displacement of bridges [8]. Optical sensors, based on triangulation and optical beam deflection, have also been reported for displacement monitoring [9]. In one example, laser and holography techniques

were used to monitor inclination [10]. While these optical sensors offer better sensitivity and overcome some limitations of conventional sensors, they have their own drawbacks. Generally, they are bulky, complex, and possess high alignment sensitivity. Their performance can be severely degraded in adverse weather conditions such as fog or rain. Furthermore, they cannot be used in hazardous environments with intense radiation, high voltage, or high temperatures. Remote sensing and multiplexing capabilities are also not feasible with these sensors. Thus, such optical sensors possess limitations for the purpose of using in various real-field applications. Consequently, a sensor that offer optimal sensitivity, along with long-term performance durability, immunity to EM/RF interference, and the capability to operate in hazardous environments while offering remote sensing and multiplexing is crucial for real-field applications.

With the adoption of fiber optics, sensing technology was revolutionized. The discovery of optical fiber in the early seventies, due to the pioneering work of George Hockham and Charles Kao, marked a major breakthrough for the telecommunications industry. However, during the early stages of development in fiber optics technology, an unexpected sensitivity of optical fibers to external factors such as bends, micro-bends, and pressure was observed. Initially, considerable efforts were made trying to mitigate these sensitivities, as it was reducing the efficiency of telecommunications systems. However, researchers quickly recognized the potential to harness the inherent sensitivity of optical fibers for sensing various parameters of interest. Thus, the field of optical fiber sensing was born. The subsequent advancements in fiber optics technology, coupled with the rapid progress in optoelectronic industries, led to the availability of low-loss optical fibers across different wavelength ranges and highly sophisticated optical sources and interrogators. This convergence of technological breakthroughs propelled the development of optical fiber sensors for a wide array of applications, spanning disciplines from engineering (civil, mechanical, aeronautical, chemical,

electrical, automotive, etc.) to biomedical sciences, general sciences, environmental monitoring and even homeland security. The inherent advantages offered by optical fiber sensing technology have spurred global interest in research and development in the field of optical fiber sensors (OFS). Some of the key benefits of optical fiber sensors are mentioned below [11], [12]:

1. Fiber optic sensors offer unparalleled sensitivity, allowing for the detection of extremely minute changes in the physical parameters they are designed to monitor.
2. Easy to miniaturize, enabling the development of compact, lightweight, and flexible optical fiber sensors.
3. Being optical, the primary signal is not subjected to any electromagnetic interference (EMI). This makes OFSs inherently immune to EMI, ensuring high reliability.
4. Low-loss optical fiber, along with the conjugation of fiber amplifiers allows propagation of light over thousands of kilometers. This capability supports dense wavelength-division multiplexing (DWDM) systems, achieving over 100 Tb/s-km in optical fiber communication. Such extensive data transmission over long distances also facilitates effective remote sensing.
5. Huge bandwidth of optical fibers provides unparalleled information-carrying capacity (ICC), surpassing electrical systems. This enables: (a) multiplexing large number of optical fiber sensors into one single fiber transmission line (b) distributed and quasi-distributed sensing, and (c) multi-parameter sensing capabilities.
6. Optical fibers are highly durable and resistant to corrosion. This makes them suitable for long-term deployments over wider temperature range even in harsh and hazardous environments.

7. As optical fiber is made of insulating materials, OFSs are inherently electrically isolated from the interrogating electronics.
8. Their small size and lightweight nature make optical fiber sensors easy to surface-mount or embed within composite materials without intrusion.

These advantages, compared to conventional and optical sensors, have led to the widespread adoption of optical fiber sensors across diverse real-field applications, where accurate and reliable measurements are paramount [13], [14]. Optical fiber sensors have been realised to detect a wide array of physical parameters of practical importance, including pressure [15], inclination [16], liquid-level [17], [18], temperature [19], displacement [20], acceleration [21], electric current [22], voltage [23], cracks in concrete [24], strain [25], RI [26], rotation [27], acoustic [28], pH [29], antibodies [30], relative humidity [31], torsion [32] etc., with high precision and sensitivity.

Optical fiber sensors can be broadly classified into two categories: extrinsic sensors (hybrid) and intrinsic (all-fiber) sensors, depending on the role of optical fiber in the sensing system [33]. In extrinsic sensors, the optical fiber serves primarily as a medium to transmit the light-wave signal to and from an external sensing head, where the modulation of the optical signal (due to an external perturbation) occurs outside the fiber itself [34]. Conversely, in intrinsic sensors, the fiber itself functions as the sensing element. In this case, the environmental or external perturbation directly modulates one of the inherent characteristics of the light-wave signal within the fiber, such as phase, polarization, wavelength, or intensity [35]. Intrinsic fiber sensors can further be subdivided as intensity-modulation-based, wavelength-modulation-based, phase-modulation-based, or polarization-modulation-based, depending on which characteristic of the light-wave signal is being modulated. Among these, intensity, phase, and wavelength modulation are the most commonly used techniques due to their ease of implementation and popularity among researchers.

While optical fiber sensors using intensity-modulation schemes are easy to fabricate and popular, their performance is affected by fluctuations in the light source power. Consequently, these sensors are often impractical for real-world applications, remote sensing and multiplexing. In contrast, the wavelength-modulation scheme is the most suitable mechanism to harness the advantages of fiber optics (e.g., high bandwidth, enormous ICC, DWDM etc.) to its full potential. For OFSs that exploit wavelength-modulation technique, the sensed information is encoded in wavelength. Wavelength-modulation schemes can be implemented in various ways, such as through wavelength-dependent absorption, luminescence, dispersion, interference, and scattering. Since the invention and subsequent advancements of fiber Bragg gratings (FBGs), they have become synonymous with optical sensing technology due to their practical advantages in real-field applications [36].

Fiber Bragg grating (FBG) or a short period grating is an intra-core periodic RI (RI) perturbation along a specified small length of a single-mode fiber, that facilitates a strong coupling between identical or nearly identical contra-propagating fiber modes [37]. When broadband light is launched into the core of a single mode fiber where a FBG is inscribed, it gets scattered from each of the grating planes and suffers very weak reflection. If the phase matching condition (Bragg condition) is not satisfied, the reflected light from each of the subsequent grating planes becomes progressively out of phase, eventually cancelling each other out. However, when the Bragg condition is satisfied, the reflected light from each grating planes would be in phase and adds constructively in the backward direction, giving rise to a strong back-reflected peak, centred at a specific wavelength determined by the grating parameters. On the contrary, the other wavelength components get transmitted through the grating, resulting in the transmission spectrum of the FBG, as shown in Fig. 1.1 [38].

The Bragg condition reflects the principles of energy and momentum conservation [39]. Energy conservation ($\hbar\omega_f = \hbar\omega_i$) dictates that the frequency of the forward and backward radiations to be identical. Meanwhile, momentum conservation stipulates that the propagation constant of the incident radiation ($\overrightarrow{\beta_i}$) plus the grating wave-vector ($\vec{K}$) must equal the propagation constant of the scattered radiation ($\overrightarrow{\beta_s}$). This can be written as,

$$\overrightarrow{\beta_i} + \vec{K} = \overrightarrow{\beta_s} \tag{1.1}$$

Here, $\vec{K}$ has a direction normal to the grating planes. The magnitude of $\vec{K}$ is $2\pi/\Lambda$, where Λ is the grating pitch. Moreover, the propagation constants for incident and scattered radiation are equal in magnitude and opposite in direction, $\overrightarrow{\beta_i} = -\overrightarrow{\beta_s}$. Considering the scattered wavelength that satisfies the Bragg condition is denoted by λ_B (Bragg wavelength), we can write $\beta_s = 2\pi n_{eff}/\lambda_B$. Here, n_{eff} is the effective RI of the fundamental mode. Hence, the momentum conservation condition can be rewritten as,

$$\lambda_B = 2n_{eff}\Lambda \tag{1.2}$$

In a standard optical fiber, n_{eff} can only be modulated by applying strain or temperature perturbations exploiting strain-optic or thermo-optic effects. However, due to the finite

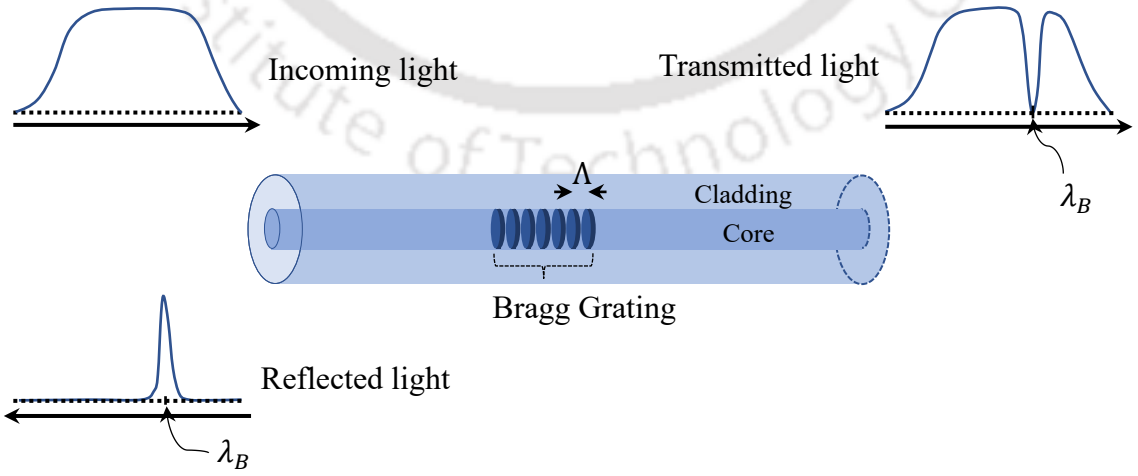

Figure 1.1: *Schematics diagram of fiber Bragg grating principle*

elasticity and thermal expansion coefficient of the fiber material, the grating pitch can also be modulated by variations in strain or temperature across the grating region. These strain and temperature-induced effects on n_{eff} and Λ result in a shift in the Bragg wavelength (λ_{B}). Using Eq. (1.2), this Bragg wavelength shift can be expressed mathematically as [40],

$$\frac{\Delta\lambda_{\text{B}}}{\lambda_{\text{B}}} = \left(\frac{1}{n_{eff}}\frac{\partial n_{eff}}{\partial \epsilon} + \frac{1}{\Lambda}\frac{\partial \Lambda}{\partial \epsilon}\right)\Delta\epsilon + \left(\frac{1}{n_{eff}}\frac{\partial n_{eff}}{\partial T} + \frac{1}{\Lambda}\frac{\partial \Lambda}{\partial T}\right)\Delta T \tag{1.3}$$

Here, $\Delta\epsilon$ represents the change in longitudinal strain and ΔT represents the change in temperature. The first term in bracket on the RHS represents the strain effect on the Bragg wavelength shift, which consists of strain induced change in the RI (strain-optic effect) and strain induced change in the grating pitch. The second term in bracket corresponds to the temperature effect on the Bragg wavelength shift, that consists of temperature induced change in the RI (thermo-optic effect) and temperature induced change in the grating pitch. The above equation can be simplified to [40],

$$\frac{\Delta\lambda_{\text{B}}}{\lambda_{\text{B}}} = (1 - P_e)\Delta\epsilon + (\alpha + \xi)\Delta T \tag{1.4}$$

Here, P_e is the photo-elastic coefficient of the fiber, α and ξ denote the thermal expansion coefficient and thermo-optic coefficient, respectively. As observed in Equation (1.4), FBG sensors employ wavelength modulation through strain and temperature induced effects when subjected to the applied strain and temperature perturbations. This makes FBG an inherent strain and temperature sensor. To design an FBG sensor capable of independently measuring strain and temperature, it is crucial to devise a smart mechanism to decouple these two informations. Various strategies/designs have been effectively employed to isolate the impact of one parameter from the measurement, especially temperature [41]–[43]. Another characteristic of FBG is its insensitivity to the ambient RI. However, if the cladding diameter in the region carrying FBG is reduced enough, the effective RI of the propagating mode gets

modulated in accordance with the RI of the surrounding medium. This makes FBG with thinned cladding to be not only sensitive towards strain and temperature but also to the ambient RI. These distinct characteristics of FBGs make them a preferred option for a wide range of sensing applications across diverse fields spanning various engineering, industrial and biomedical applications [44].

In addition to the inherent advantages of fiber optics, Fiber Bragg Grating (FBG) sensors offer several unique benefits. One of the key advantages is their immunity to source power fluctuations, which provides FBG sensors with an inherent self-referencing capability [45]. FBGs also enable the multiplexing of a large number of sensors on a single fiber channel and seamlessly integrate with techniques such as DWDM, spatial-division multiplexing, time-division multiplexing (TDM) [46]. This enables FBG sensors to support quasi-distributed sensing of various parameters of practical interest, by associating each spectral segment with a specific spatial location [47]. These substantial advantages have made FBG sensors a preferred and indispensable solution across various engineering and industrial applications, including structural health monitoring (SHM), mechanical and aeronautical engineering, communication engineering, and biomedical/micro-fluidics. Among all the monitoring and sensing systems across wide range of engineering and industrial applications, SHM stands out as one of the most significant fields where OFSs (especially FBG sensors) are experiencing phenomenal growth, particularly due to a rising demand of safe structures.

The diverse advancements in global human civilization as well as in science and technology have led to an unprecedented increase in civil infrastructures. However, during the course of their lifetimes, all types of civil infrastructures, such as bridges, tunnels, dams, railways, aerospace structures, wind turbines, oil and gas wells, as well as our houses and high-rise buildings, can experience adverse changes in their structural health due to potential damage or deterioration. This damage can be caused by several factors, including environmental

degradation, wear and tear, design and construction errors, overloads, and unexpected events like earthquakes or tsunamis etc. [48]. These adverse changes (damage/deterioration) are not possible to be anticipated beforehand during the design and realisation of such infrastructures. Therefore, to ensure a safe and efficient use of these structures, along with regular inspection and maintenance of their structural health, continuous health monitoring becomes essential. An SHM system involves the integration of robust, reliable, and intelligent devices to continuously monitor the state of the health of civil infrastructures in real-time through the measurement of various parameters affecting them. This enables timely interventions as well, when necessary. SHM is achieved by recording, analysing, localizing, and predicting the conditions leading to structural loading and damage in such a way that non-destructive testing becomes an integral part of the monitoring process [48], [49]. Such monitoring that includes continuous and real-time inspection on various parameters cannot be done manually with unaided eye. Such processes are inaccurate, time consuming and faulty. Therefore, implementing smart and autonomous monitoring of health condition of the civil infrastructures is crucial to reduce costs and enhance efficiency. FBG-based OFSs have become the most feasible solution for SHM due to the exceptional advantages offered by them. Numerous attempts have been made in order to develop FBG based OFSs to monitor various parameters of interest in SHM (i.e. pressure, tilt, displacement, flow, vibration, torsion, acceleration, etc.) and other engineering and industrial applications. To develop FBG-based sensors for these additional parameters, a smart mechanism needs to be developed that can map the required parameter, generally onto the strain domain. Significant efforts have been dedicated to the development of such FBG-based sensors. Nowadays, nearly all practically significant parameters, including tilt [50], liquid-level [51], rotation [52], strain [53], temperature [54], displacement [55], acceleration [56], pressure [57], liquid level [58], torsion [59], relative humidity [60], pH [61], acoustic [62], and RI [63],

are being successfully and accurately monitored using fiber Bragg grating (FBG) based sensors in real-world environments.

Among all the parameters affecting the health of civil infrastructures, tilt angle monitoring is very important. Additionally, it is equally critical in fields such as mechanical engineering, instrumentation, robotics, and aeronautical engineering applications [64]. Tilt sensors help in monitoring the angular displacement, which provides critical information about the structural integrity of buildings, bridges, and other civil infrastructures. Detecting minor tilts (<4° from the point of view of civil engineering applications) can help predict larger deformations or collapses, which is especially important for tall buildings, towers, and bridges exposed to wind loads, seismic activity, or gradual ground movements. Therefore, the development of a highly accurate, sensitive, and compact tilt monitoring sensor system, capable of resolving minimal tilt angle variation over the desired dynamic range is of paramount importance. Conventional tilt sensors are predominantly electronic in nature, mapping inclination information into electrical signals [65]–[67]. For example, Benz *et al*. [65] proposed a micromechanical capacitive inclination sensor, that utilizes the relative movement of a dielectric fluid between two semi-circular electrodes for tilt measurement. Jung *et al.* [66] proposed a MEMS-based electrolytic tilt sensor, where the output voltage of sensor varies depending on the varying applied inclinations. Another capacitive tilt sensor using two electrodes and a metallic ball was proposed by Lee *et al.* [67]. However, inherent limitations of these sensors, such as, susceptibility to EMI, pose a great challenge when deployed in harsh environments. Further, the inability towards multiplexing, remote sensing and distributed sensing make them impractical for various engineering applications. As discussed earlier, some of these problems can be overcome by aligning towards optical sensing technology. However, only a few successful attempts have been made in order to develop all-optical tilt sensors using laser-based sensing technology. For instance, Zhong *et al*. [68] reported an optical tilt sensor

using wavefront sensing technique. [69], [70] proposed tilt angle-measurement method based on internal reflection of light beam in prism. Additionally, Hua *et al.* [71] explored a laser interference based tilt sensor, while Xiaoyong *et al.* [10] introduced a tilt sensor using laser and holographic techniques. Despite these efforts, the bulky and complex design configurations, coupled with extreme sensitivity to alignment, render these methods impractical from the point of view of real-field applications. To address these limitations OFSs are explored. However, only a few studies have focused on developing optical fiber sensors for tilt-angle monitoring. For example, Yuan *et al*. [72] proposed a Mach-Zehnder reflector-based push-pull fiber optic tilt sensor. Lee *et al*. [16] reported a tilt sensor using optical fibers as transceivers to capture reflected light upon tilting. Bajic *et al*. [73] described a tilt sensor utilizing lead-in and lead-out optical fibers separated by a specific distance in a liquid container; the reorientation of the liquid surface upon rotation causes variations in the captured optical power by the lead-out fiber. Although these sensors demonstrate good capability in detecting applied tilt, they suffer from limitations such as less sensitivity, less tilt-angle resolution, along with inherent measurement errors resulting due to their complicated design strategies. Recently, numerous innovative approaches and unique designs have been employed to develop FBG-based all-optical tilt sensors. Some of these sensors incorporate a pendulum suspension mechanism, with a mass either suspended from the top [64], [74]–[78] or hanged freely from the fiber[79]. In [64], [74], the fiber, with strategically placed grating structures onto it, captured the restricted movement of the suspended mass when the tilt perturbation was applied to the sensor. Other sensors, as reported in [75]–[77], utilized a cantilever-based pendulum suspension mechanism. Those sensors relied on the pendulum's rotation when tilt was applied. As an example, Dong *et al*. [78] proposed a complicated sensor design that employed pendulum structure. Here the pendulum structure was hung through three steel flakes. FBGs were glued onto those flakes. Ni *et al*. [79] reported tilt sensor using an inverted pyramidal structure with multiple FBGs

arranged in different configurations. However, ensuring sensor stability and addressing cross-sensitivity to unwanted perturbations (such as oscillations) were significant challenges in these designs. The direct suspension of the mass from the fiber loop is bound to induce undesired oscillations in these fiber-mass pyramidal structure-based sensors, leading to measurement inaccuracies and potential sensor instability. Additionally, there is a high likelihood of slackening in the fiber arms of the structure during tilt. Chen *et al*. [80] proposed an approach using a single FBG, while Li *et al*. [81] explored a tilt sensor employing a dual FBG configuration. Aneesh *et al.* [82] reported a tilt sensor using four FBGs and a spring-bob system, offering an enhanced tunable response. Pathi *et al*. [83] explored a sensor design utilizing a fiber with four FBGs glued strategically to the side of a bob, fixed with a vertical sturdy wire. All the sensors, discussed above, are characterized with reasonably moderate sensitivity, resolution, and accuracy. However, one of the major limitations with most of these sensors [74]-[78],[80],[81] was the lack of tuning mechanism that resulted in fixed response characteristics. Therefore, a critical need persists for a tilt sensor that combines optimal sensitivity with high measurement accuracy, minimal discrepancy, high angular resolution, and inherent sensitivity tuning capability, which are very crucial for real-field applications.

Liquid level sensing is also equally critical for the structural health of certain infrastructures, particularly those exposed to water or liquid-related stress, such as pillars (that support bridge), dams, and flood barriers. Changes in water or liquid levels can exert pressure on structures, accelerating degradation or even causing catastrophic failures if not detected early. Along with this, liquid level sensors are also extensively important in various industries including fuel reservoirs, chemical industries, water and waste water management industries, food and beverage industries, petrochemicals, pharmaceuticals as well as in agricultural and residential use that involves storage tanks of considerable size with substantial depths (2-6 m) [84]-[86]. Along with improving the operational efficiency of industries, they also serve an

extremely crucial role in guaranteeing safety by providing early prediction of flood by tracking the rising water levels, enabling early warnings and evacuation alerts in flood-prone areas. These applications require sensing systems that are capable of monitoring liquid level accurately. There are few conventional liquid level sensors that are proposed in the past few decades [87]–[89]. These sensors are characterised with good sensitivity. However, their operations are limited because of the size, susceptibility to electromagnetic interference, and inability to adapt to potentially explosive, corrosive and conductive environments. Later on, few attempts have been made in order to develop all-optical liquid level sensors that overcome some of the major shortcomings of conventional sensors [90], [91]. However, they have their own major limitations of being highly alignment sensitive and incapable for remote sensing and multiplexing, to name a few. These shortcomings, in-effect, make them impractical for real field applications. To address these limitations, OFSs have been explored. Numerous attempts have been made in realizing optical fiber liquid-level sensors employing various configurations, e.g., etched fiber [17], [92], [93], standard optical fiber [94], [95], optical fiber interferometers [96]–[99] etc. Several attempts have also been made in order to realize liquid level sensors based on FBG/ etched FBG (EFBG) [51], [100]–[104], tilted FBG [105]-[107] and long period grating (LPG) [108],[109]. For instance, Yun *et al*. [51] reported an EFBG based liquid level sensor that employed effective RI modulation mechanism. This sensor exhibited a nonlinear response over the dynamic range of ~1.5 cm. Guo *et al.* [100] reported another liquid level sensor based on the chirping of an embedded FBG onto a complex bending cantilever beam and column buoy structure. Lai *et al.* [101] proposed another scheme where liquid level sensor employed FBG embedded tapered cantilever beam and column buoy structure. A linear response with the experimentally obtained sensitivity of 14.91 pm/cm (much lower than the theoretically predicted sensitivity) and a resolution of ~3 cm was observed. FBG based liquid level sensor reported by Sohn *et al.* [102] employed a complex cantilever rod and

float structure. The sensor exhibited a linear response over a dynamic range of 0-36 cm with a sensitivity of 0.1 dB/cm. In another sensor reported by Sheng *et al.* [103], EFBG was encapsulated in a half-polymer-filled metal cylinder. In comparison to the theoretically anticipated sensitivity of 2.15×10^{-5} cm^{-1} pm/cm, experimentally observed sensitivity for the proposed sensor was 1.526×10^{-5} cm^{-1} pm/cm. Almeida *et al.* [104] developed a liquid level sensor by embedding FBG in a silicone rubber. The sensor showed a linear response with a maximum sensitivity of 1.56 pm/cm. In summary, reported sensors employed very complex structure, exhibited limited operational range and in many cases theoretically expected response could not be achieved experimentally.

1.1 Objective and summary of the thesis

The main objective of the thesis is to develop novel all-optical FBG-based tilt sensor and liquid level sensor, which are crucial for SHM and other real-field applications. It is essential to note that, in order to effectively capture applied perturbations, a sensor is required to have reasonably good sensitivity. Furthermore, achieving minimal discrepancy and uncertainty, along with high accuracy and resolution and possibly with tunable response characteristics, is crucial for a stable and effective sensing mechanism. In order to achieve these, first, a novel, all-optical, design strategy for the development of temperature insensitive non-pendulum type FBG based tilt sensor is proposed. The sensor has a provision to tune the response characteristics by simply varying the loaded mass onto it. Modulation of wavelength separation between two FBGs in accordance to the applied tilt makes the sensor inherently temperature insensitive. Response characteristics of the proposed sensor is theoretical analysed and experimentally established. An excellent agreement is observed between theoretically predicted and experimentally obtained responses. Sensor exhibits an excellent sensitivity with a high accuracy, minimal maximum discrepancy and angular resolution. To strategically

capture applied tilt perturbations with better sensitivity and to improve the sensor performance further, another novel design strategy for the development an FBG-based temperature-independent all-optical tilt sensor is proposed. The design strategy inherently enables the tuning of the response characteristics simply by varying the mass. This sensor exhibited substantial improvements not only in sensitivity, but also in accuracy, minimal maximum deviation, and angular resolution. In order to further enhance the sensor performance, such as, sensitivity, angular resolution, accuracy and angular uncertainty, another novel design strategy for the development of a temperature-insensitive FBG-based all-optical tilt sensor is proposed. This sensor also has a provision of tuning the response characteristics as per the requirement. Both theoretical analyses and extensive experimental investigations were carried out under varying tilt angles. The sensor demonstrates significantly improved overall performance, featuring an excellent sensitivity nearly eight times higher than that of the previous sensor. Additionally, experimental observations highlight the sensor's high degree of reversibility, repeatability, and reliability.

In the next part of the research, instead of traditional wavelength modulation mechanism, intensity modulation of the FBG spectrum that exploits the effective RI sensitivity of EFBG is used to develop novel all optical tilt sensor. This technique is utilized for the first time for the development of tilt sensor, to the best of author's knowledge. The design strategy of the proposed sensor employs four EFBGs in vertical configuration. All the four EFBGs are initially immersed upto the half-length into a strategically chosen liquid. The sensor characteristics of the design was investigated theoretically. The sensor exhibits high sensitivity. In order to capture applied tilt with better sensitivity and improve sensor performance, another sensor is proposed that exploits the same sensing mechanism (intensity modulation of EFBG). The design strategy of the proposed sensor is based on four EFBGs, each inclined in the vertical plane while making a cross. The sensor characteristics of the new sensor design was also

investigated theoretically. The maximum theoretical sensitivity for this sensor comes out to be double to the sensitivity observed for the previous sensor. Additionally, the peak reflectivity of FBG spectrum being independent of temperature variation, the response of the proposed sensor is free from the temperature cross-sensitivity.

Additionally, an FBG-based all-optical liquid level sensor exploiting Archimedes' law of buoyancy is developed. Objective of research in this part of work is to achieve high sensitivity towards liquid level variation along with significantly high resolution and high accuracy (<0.5% full scale reading (FSR); minimum requirement as per the industrial standards). Response characteristics of the proposed sensor is theoretically investigated and experimentally established. The sensor exhibits outstanding maximum sensitivity. Experimental results confirm that the proposed sensor is capable of achieving liquid level measurement with excellent resolution and exceptional accuracy.

1.2 Organization of the thesis

Chapter-1

This chapter establishes the foundation of the proposed research work. It begins with discussing about conventional sensors and their limitations, followed by the importance of optical fiber technology in the sensing industry. The next section discusses the theory of FBG and its sensing applications in various diverse fields, especially in SHM. In the next section, an extensive literature survey is carried out on the existing tilt and liquid level sensors and their limitations are reported. The last section establishes the objectives of the thesis work and the methodologies used in achieving those objectives.

Chapter-2

The objective of the research reported in this chapter is to develop FBG based novel all-optical temperature-insensitive tilt sensor. Initially, a novel sensor design comprised of a wheel and rod system was conceptualized. Then, comprehensive theoretical analysis was carried out to (a) establish feasibility of capturing the applied tilt, (b) understand the response characteristics and (c) examine the impact of various design parameters on the response characteristics. Based on these theoretical findings, sensor was designed and rigorous experimental investigations were carried out in order to establish various critical features of the proposed sensor (e.g., resolution, accuracy, maximum discrepancies, uncertainties, and reliability). It is important to mention that this sensor design was capable of tuning the response characteristics, as desired, for specific applications. During the experimental investigations, individual responses of both the FBGs were recorded. Applied tilt perturbation induced wavelength shifts were analyzed, confirming the sensor's effectiveness in detecting tilt angle variations with a consistent linear and reversible response within the dynamic range of ±10°. It is crucial to mention that, all the experimental results show a great agreement with the theoretical results. The sensor also demonstrated excellent resolution, accuracy, and repeatability, maintaining stable performance over multiple trials. Its design inherently compensates for temperature fluctuations by relying on the wavelength difference between two FBGs, significantly reducing temperature-induced shifts. Comparative analysis of the response characteristics establishes that the proposed sensor outperformed the other sensors reported in the literature in terms of observed sensitivity, accuracy, and tunability. These features make the proposed sensor highly suitable for the real-world applications.

Chapter-3

The previous chapter described the development of temperature-insensitive FBG-based tilt sensor that employed rod and wheel system. Even though, the sensor was characterised with a good sensitivity and accuracy, there is ample scope to improve the overall response characteristics of the tilt sensor. This chapter introduces another novel design strategy for the development of a temperature-insensitive FBG-based tilt sensor with further improved response characteristics. Initially, the sensor design was conceptualized, followed by an in-depth theoretical analysis aimed at determining the feasibility of capturing applied tilt and understanding the response characteristics. The design comprises of a giant wheel mounted in the vertical plane with its axle fixed rigidly onto two parallel vertical stands. Rigorous experimental investigations were conducted to establish critical features of the proposed sensor, such as resolution, accuracy, maximum discrepancies, uncertainties, and reliability. It is important to mention that this sensor design is also capable of tuning the response characteristics, as per requirement, simply by varying the mounted mass applied on the sensor. The experiments confirm that the sensor effectively measures tilt angle variations while maintaining a linear and reversible response across a ±10° range. The sensor exhibits excellent agreement with theoretical predictions, with minimal discrepancies and angular uncertainties, demonstrating high precision in both forward and reverse tilts. It also delivers impressive resolution and accuracy, improving consistently with increased mass loading. The sensor shows highly repeatable and reliable performance over time, as verified through repeatability tests. A key advantage of the design is its inherent temperature insensitivity, achieved by monitoring the wavelength difference between two FBGs. This approach significantly suppresses temperature-induced shifts, ensuring measurement stability under varying thermal conditions. Comparative evaluation further reveals that the proposed sensor surpasses existing counterparts

in terms of sensitivity, accuracy, and tunability, making it well-suited for practical, real-world applications.

Chapter-4

Building upon the findings and advancements detailed in the previous chapter, the pursuit of enhanced sensor performance continues in this chapter. This chapter emphasizes on the development of a novel FBG-based temperature-insensitive novel tilt sensor. The sensor consists of a double pendulum having a common axle. Rigorous experimental investigations were conducted to establish critical features of the proposed sensor, such as resolution, accuracy, maximum discrepancies, uncertainties, and reliability. It is important to mention that this sensor design is also capable of tuning the response characteristics, as per requirement, simply by varying the mounted mass applied on the sensor. Experimental investigations confirm that the sensor is capable of measuring tilt angles with excellent sensitivity, resolution, and accuracy. The observed results align closely with theoretical predictions, reflecting high precision and minimal measurement uncertainty. Repeatability and reliability tests further validate the sensor's consistent performance over time, with negligible variation in output. The design inherently compensates for temperature effects, as both FBGs experience identical thermal shifts, which cancel out in the differential measurement. This effectively neutralizes temperature-induced errors, ensuring thermally stable operation. When compared to other sensors, the proposed design exhibits superior performance across all key sensing parameters, including sensitivity, accuracy, and reliability, making it a strong candidate for high-precision tilt sensing applications.

Chapter-5

In this chapter, a novel all-optical tilt sensor is developed by utilizing intensity modulation of the FBG spectrum that exploits the effective RI sensitivity of EFBG, instead of the traditional

wavelength modulation mechanism. This technique is utilized for the first time for the development of tilt sensor, to the best of author's knowledge. The design strategy of the proposed sensor employs four EFBGs in vertical configuration. All the four EFBGs are initially immersed upto the half-length into a strategically chosen liquid. Response characteristics of the proposed sensor against tilt angle variations are theoretically investigated. The maximum theoretical sensitivity of the proposed sensor comes out to be 1.20 dB/°. In order to capture applied tilt with better sensitivity and improve sensor performance, another sensor is proposed that exploits the same sensing mechanism (intensity modulation of EFBG). The design strategy of the proposed sensor is based on four EFBGs, each inclined in the vertical plane while making a cross. The sensor characteristics of the new sensor design was also investigated theoretically. The maximum theoretical sensitivity for this sensor comes out to be double to the sensitivity observed for the previous sensor. Furthermore, both the sensors are observed to be capable of measuring the magnitude and the direction of inclination relative to the horizontal plane across the designated dynamic range of -10° to 10°, exhibiting excellent reversibility and reliability. Additionally, as peak reflectivity of FBG spectra does not depend on the temperature variations, change in temperature will cause the centre wavelength of the FBGs to get shifted. But, the reflected peak, which is used to monitor the applied tilt in our work, remains unaffected by temperature fluctuations. Thus, the problem of temperature cross-sensitivity gets eliminated inherently.

Chapter-6

The main objective of the research introduced in this chapter is to present a novel design for a liquid level sensor using Fiber Bragg Grating (FBG) technology. In the proposed sensor, Archimedes' law of buoyancy is exploited. The design involves two Fiber Bragg Gratings (FBGs) mounted on a single optical fiber, with a cylindrical metallic mass suspended in the liquid whose level is being measured. As the liquid level changes, the buoyant force on the

cylindrical mass alters the strain experienced by the FBGs, causing a shift in the reflected Bragg wavelengths. Experimental results confirm that the sensor exhibits high sensitivity, closely matching theoretical predictions, with minimal discrepancy across the designed dynamic range. The sensor demonstrates excellent resolution and accuracy in liquid level measurements, making it well-suited for precision applications. A key advantage of the design is its tunable sensitivity—achieved by adjusting the mass of the suspended cylinder—allowing the sensor to be customized for various application needs. Repeatability tests further validate the sensor's consistent and reliable performance over time. Temperature independence is ensured through differential wavelength shift measurement between two FBGs, effectively cancelling out thermal effects and maintaining stable operation across temperature variations. These features collectively make the proposed sensor highly precise, versatile, and robust for real-world environments.

Chapter-7

This chapter of the thesis presents a summary and highlights of the FBG-based tilt sensors and liquid level sensor employing wavelength modulation and intensity modulation techniques, exploiting the distinct characteristics of FBGs. Additionally, the chapter outlines the future scope of the presented research work.

1.3 List of Publications:

1.3.1 Journal Publications:

1. D. Paul, S. Mohan and S. K. Khijwania, "Development of Fiber Bragg Grating-Based Temperature Insensitive Novel All Optical Tilt Sensor," in *IEEE Photon. Technol. Lett.* vol. 36, no. 23, pp. 1377-1380, Dec, 2024, doi: 10.1109/LPT.2024.3480327.

2. D. Paul and S. K. Khijwania, "Etched Fiber Bragg Grating-Based Novel Tilt Sensor Employing Effective RI Induced Intensity Modulation Mechanism," in *IEEE Sens. Lett*, vol. 8, no. 11, pp. 1-4, Nov, 2024, doi: 10.1109/LSENS.2024.3482990.
3. D. Paul, S. Mohan and S. K. Khijwania, "Novel All-Optical Highly Sensitive Tilt Sensor Based on Etched Fiber Bragg Grating Utilizing Effective RI Induced Intensity Modulation," (Communicated)
4. D. Paul and S. K. Khijwania, "Highly sensitive and temperature insensitive Fiber Bragg grating based liquid-level sensor", (Communicated)
5. D. Paul and S. K. Khijwania, "Novel design strategy for the development of temperature insensitive fiber Bragg grating tilt sensor", (Communicated)
6. D. Paul and S. K. Khijwania, "Fiber Bragg Grating Based Temperature-Insensitive Tilt Sensor with Optimum Response Characteristics", (Communicated)

1.3.2 Conference Proceedings:

1. D. Paul and S. K. Khijwania, "Highly sensitive and temperature insensitive Fiber Bragg grating based liquid-level sensor", *OFS-2023*, W4.100, 2023, doi: 10.1364/OFS.2023.W4.100.
2. D. Paul, S. Mohan and S. K. Khijwania, "Development of Optical Fiber Tilt Sensor Using Etched Fiber Bragg Grating", *Optica Sensing Congress*, SW3D.5, 2023, doi: 10.1364/SENSORS.2023.SW3D.5

1.4 Paper presented in conferences (national & international)

1. D. Paul, S. Mohan and S. K. Khijwania, "Highly Sensitive Novel Fiber Bragg Grating Based Tilt Sensor For Structural Health Monitoring", XLIV OSI Symposium on Frontiers

in Optics & Photonics “FOP-21”, 24-27 September 2021, IIT Delhi, India. (Excellence in Oral Paper Presentation Awards)

2. D. Paul and S. K. Khijwania, “Novel Fiber Bragg Grating Based Tilt Sensor Employing Effective RI Modulation Mechanism”, Photonics-2023, 5-8 July 2023, IISc Bengaluru, India. (Poster)
3. D. Paul, S. Mohan and S. K. Khijwania, “Development of Optical Fiber Tilt Sensor Using Etched Fiber Bragg Grating”, Optica Sensing Congress 2023, 30 July-3 August, 2023, Munich, Germany. (Oral)
4. D. Paul and S. K. Khijwania, “Highly sensitive and temperature insensitive Fiber Bragg grating based liquid-level sensor”, 28th international conference on optical fiber sensor “OFS-28”, 20-24 November, 2023, Hamamatsu, Japan. (Poster)
5. D. Paul and S. K. Khijwania, “Fiber Bragg Grating Based Temperature Insensitive Tilt Sensor For Structural Health Monitoring”, Photonics-2024, 12-15 December 2024, IIT Kharagpur, India. (Poster)

Chapter 2 : Novel design strategy for the development of temperature insensitive fiber Bragg grating tilt sensor

2.1 Introduction

Inclination or tilt-angle monitoring plays a critical role in assessing the state of the health of civil infrastructures such as bridges, tunnels, dams etc. Furthermore, it is equally critical in applications across mechanical engineering, instrumentation, robotics, and aeronautical engineering applications [64]. Therefore, development of a highly accurate, extremely sensitive, and compact tilt monitoring system, capable of detecting the smallest tilt-angle variations across a wide dynamic range, is very important. Most of the conventional tilt sensors are predominantly electronic in nature, mapping inclination information into electrical signals through mechanisms such as magnetic or capacitive effects [65]–[67]. However, inherent limitations of such sensors, including susceptibility to EMI, challenges to deploy in harsh environments and the inability towards multiplexing, remote sensing and distributed sensing, impose serious problems for these sensors. Such drawbacks in-effect hinder their practicality for real-world applications. For example, Zhong *et al.* [68] reported an optical tilt sensor exploiting wavefront sensing technique. [69], [70] proposed tilt angle-measurement method based on internal reflection of light beam in prism. In another study, Hua *et al.* [71] explored a tilt sensor based on laser interference, while Xiaoyong *et al.* [10] introduced a tilt sensor that combines laser technology with holographic methods. Despite these efforts, the bulky and complex design configurations, coupled with extreme sensitivity to alignment, render these methods impractical for real-field applications. Optical fiber sensors, known for their very high sensitivity to external perturbations affecting the optical signal propagating down the fiber, have become a powerful alternative to traditional optical sensors. Since the first optical fiber sensor (OFS), introduced in 1974 [110], these sensors have evolved significantly and are

capable of overcoming many limitations of conventional sensors. With inherent advantages like remote and distributed sensing, multiplexing, compact size, light weight, and resistance to EMI, optical fiber sensors are used in wide range of real-world applications, including environmental monitoring, bio/chemical diagnostics, structural health monitoring etc. [111]. However, only a few studies have focused on developing optical fiber sensors for inclination or tilt-angle monitoring. One example is a push-pull fiber optic tilt sensor based on a Mach-Zehnder reflector, developed by Yuan *et al.* [72]. Another design by Lee *et al.* [16] used optical fibers as transceivers to capture reflected light in response to tilt. Similarly, Bajic *et al.* [73] introduced a tilt sensor using lead-in and lead-out optical fibers spaced within a liquid container. As the container rotates, the liquid surface shifts, causing changes in the optical power captured by the lead-out fiber. Although these sensors were characterised with good capability in detecting applied tilt, they suffer from various limitations such as low sensitivity, low tilt-angle resolution, and inherent measurement errors due to their complicated design strategies. With the invention of FBGs, they have received widespread recognition for their potential applications in the field of modern telecommunication systems and optical sensor networks [47]. Apart from inheriting all the advantages of optical fiber sensors, the inherent self-referencing nature and the capability of multiplexing large number of FBGs on a single fiber line make FBG based sensors integral to real-field industrial/engineering applications. FBG is inherently sensitive to strain and temperature both. Hence, FBG based sensors are strategically designed by mapping the desired parameter onto the induced strain in the FBG while negating the temperature effects. Recent advancements have introduced various FBG-based optical tilt sensors with innovative designs. Some of these sensors utilize pendulum suspension mechanisms, with a mass either suspended from the top [64], [74]–[78] or hanged freely from the fiber[79]. For instance, sensors in [64], [74] use grating structures to capture the restricted movement of the suspended mass upon tilt, while others employ utilize a

cantilever-based pendulum suspension mechanism [75]–[77]. Dong *et al.* [78] designed a sensor with a pendulum structure hung through three steel flakes, with FBGs attached to these flakes. Ni *et al.* [79] reported proposed sensors based on an inverted pyramid structure with FBGs arranged in different configurations along fiber arms. However, this design face challenges in maintaining stability and minimizing sensitivity to unwanted oscillations, which can lead to measurement inaccuracies. Additionally, slackening of fiber arms during tilt is another issue. Chen *et al.* [80] proposed an approach using a single FBG, while Li *et al.* [81] explored a tilt sensor employing a dual FBG configuration. Aneesh *et al.* [82] reported a tilt sensor using four FBGs and a spring-bob system, offering an enhanced tunable response. Pathi *et al.* [83] proposed a sensor design utilizing a fiber with four FBGs glued strategically to the side of a bob, fixed with a vertical sturdy wire. All the sensors discussed above exhibit moderate sensitivity ranging from 0.0011 to 0.0960 nm/°, accuracy from ±0.051° to ±0.360°, and angular resolution between 0.0067° to 0.019° [64], [74]–[83]. From the perspective of structural health monitoring and real-world applications, achieving a high sensitivity is essential. Additionally, it is equally important for the sensor to effectively detect tilt perturbations in a strategic manner while maintaining inherent stability. In designs prone to instability, any undesired oscillations can introduce noise in tilt measurements due to (a) random vibrations or oscillations of the suspended pendulum system and (b) slack in the fiber. Another major limitation with most of these sensors [74]-[78],[80],[81] is the lack of tuning mechanism that resulted in fixed response characteristics. It is important to note that a tilt sensor with optimum sensitivity, high measurement accuracy, minimal discrepancy, improved angular resolution, and inherently capable to tune response characteristics is of great importance for real-field applications.

This chapter introduces a novel, non-pendulum type design strategy for the development of a FBG based temperature-insensitive all-optical sensor. Initially, the sensor design is conceptualized. Comprehensive theoretical analysis is then carried out to (a) establish

feasibility of capturing the applied tilt, (b) understand the response characteristics and (c) examine the impact of various design parameters on the response characteristics. Based on these theoretical findings, sensor is designed and rigorous experimental investigations are carried out in order to establish various critical features of the proposed sensor (e.g., resolution, accuracy, maximum discrepancies, uncertainties, and reliability). It is important to mention that this sensor design is capable of tuning the response characteristics, as desired, for specific applications. During the experimental investigations, individual responses of both the FBGs are recorded. Applied tilt perturbation induced wavelength shifts are analysed. The experiments show that the sensor effectively detects tilt angle variations, maintaining consistent linear and reversible response characteristics within the dynamic range of ±10°. An excellent agreement is observed between theoretically predicted and experimentally obtained responses. The sensor displays minimal maximum discrepancy of ±0.001 nm and demonstrates a high degree of reversibility, repeatability and reliability. Comparative analysis of the response characteristics establishes that the proposed sensor outperformed the other sensors reported in the literature in terms of observed sensitivity and accuracy. Moreover, the sensing mechanism depends on mapping the varying tilt to shift in wavelength difference between the two FBGs. This approach makes the sensors inherently independent of ambient temperature fluctuations.

2.2 Concept and theory of sensor

2.2.1 Sensor conceptualization

Fig. 2.1 depicts the concept and the schematic diagram of the proposed sensor. The sensor primarily comprises a rod (CE), which is fixed to a small frictionless wheel (Fig. 2.2). The axle of the wheel is fixed to an 'L' shape frame comprising vertical plate P_1 and horizontal plate P_2

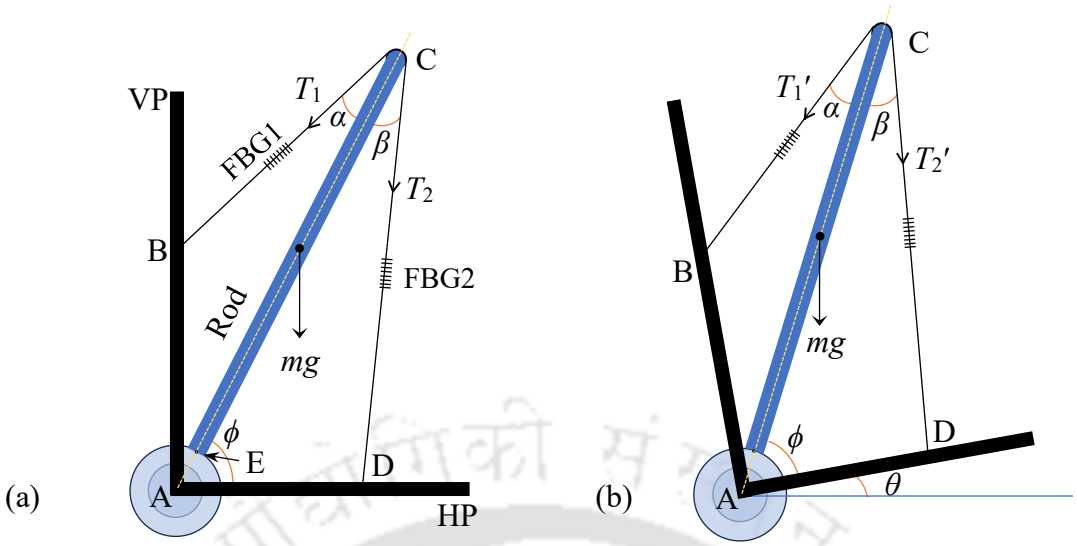

Figure 2.1: *Schematic diagram of the proposed FBG based tilt sensor (a) at zero inclination (b) at θ° inclination*

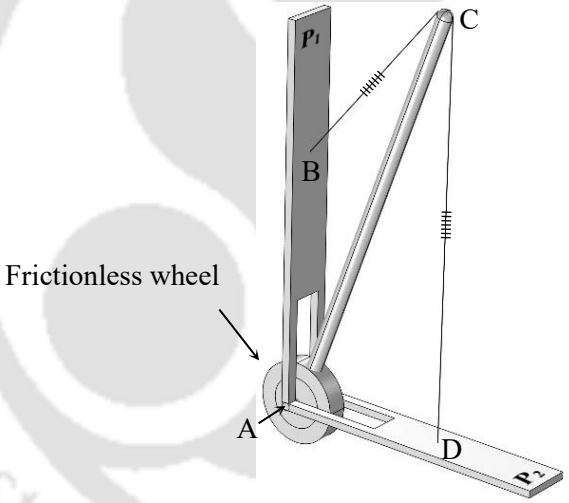

Figure 2.2: *3-D view of the proposed sensor*

(Fig. 2.1). This arrangement facilitates rod to rotate freely in a vertical plane about the center of the wheel (A). However, the frame restricts the rod to stay on P_2 in its natural state. In order to exploit the rotational tendency for realizing the proposed tilt sensor, the rod is constrained to remain oriented at a specific angle ϕ w.r.t. P_2. This is achieved with the help of FBG carrying optical fiber, which is fixed at a point B (on P_1), then at the point C (top end of the rod) and finally at a point D (on P_2), as depicted in Fig. 2.1. In this arrangement, fiber arm CB makes an angle α, whereas, fiber arm CD makes an angle β with the axis of the rod. FBGs (λ_1 and λ_2)

reside at the center of each fiber arms and the fiber is strained in a way to avoid slackening. Both the fiber arms and the axis of the rod remain in the same vertical plane. Thus, the tendency of the rod to rotate clockwise is constrained by the fiber. As the frame is tilted, strain in the fiber arms will get redistributed due to the rotational tendency of the rod. In order to design the sensor and to achive optimum response charactwrsitics with respect to the design parameters, rigorous theoretical investigation is carried out, which is presented in the following section.

2.2.2 Theoretical modelling

The force diagram of the reported sensor is also depicted in Fig. 2.1(a) and 2.1(b). The rod is of mass m and length l, while x (= AE) represents the outer radius of the frictionless wheel. At zero inclination of the sensor, T_1 and T_2 are the tensions acting in the fiber arms. Clockwise torque (τ_c) and anti-clockwise torque (τ_{ac}) about Point A are given as,

$$\tau_c = mg\left(\frac{l}{2} + x\right)cos\phi + T_2(l + x)sin\beta \tag{2.1}$$

$$\tau_{ac} = T_1(l + x)sin\alpha \tag{2.2}$$

Here, g is the acceleration due to gravity. In this constrained position of the rod, clockwise and anticlockwise torque balance each other, making the net torque about A to be zero. Hence,

$$\tau_c - \tau_{ac} = 0 \tag{2.3}$$

$$mg\left(\frac{l}{2} + x\right)cos\phi + (T_2 sin\beta - T_1 sin\alpha)(l + x) = 0 \tag{2.4}$$

Now, when the sensor is inclined by an angle θ, the tension in both the fiber arms gets redistributed from T_1, T_2 to T_1' (= $T_1 + \Delta T_1$) and T_2' (= $T_2 + \Delta T_2$), respectively. In this situation, clockwise and anti-clockwise torques (about the point A) are given by,

$$\tau_c = mg\left(\frac{l}{2} + x\right)\cos(\phi + \theta) + T_2'(l + x)sin\beta \tag{2.5}$$

$$\tau_{ac} = T_1'(l + x)sin\alpha \tag{2.6}$$

In this new constrained position of the rod, these modified clockwise and anticlockwise torque will again balance each other, making the net torque about A to be zero. Hence,

$$\tau_c - \tau_{ac} = 0 \tag{2.7}$$

$$mg\left(\frac{l}{2} + x\right)\cos(\phi + \theta) + (T_2'sin\beta - T_1'sin\alpha)(l + x) = 0 \tag{2.8}$$

In order to simplify the theoretical analysis, let us consider the angle subtended by the fiber arms BC and CD with the rod to be equal, i.e., $\alpha = \beta$. With this simplification, Eq. (2.4) and Eq. (2.8) can be merged and written as,

$$\Delta T_2 - \Delta T_1 = \frac{mg}{2sin\alpha}\left(\frac{l + 2x}{l + x}\right)[\cos\phi - \cos(\phi + \theta)] \tag{2.9}$$

In terms of the mechanical strains (ϵ) induced in both the FBG arms, Eq. (2.9) can be expressed as

$$\Delta\epsilon_2 - \Delta\epsilon_1 = \frac{1}{AE} \cdot \frac{mg}{2sin\alpha}\left(\frac{l + 2x}{l + x}\right)[\cos\phi - \cos(\phi + \theta)] \tag{2.10}$$

Here, E is the Young's modulus of the fiber material and A is the cross-sectional area of the optical fiber. For the FBG, strain induced wavelength shift is expressed as [39],

$$\frac{\Delta\lambda}{\lambda} = (1 - p_e)\Delta\epsilon \tag{2.11}$$

Here, p_e is the photo-elastic coefficient of the fiber. Assuming $\Delta\lambda_i \ll \lambda_i$; i = 1, 2; $\lambda_1 \approx \lambda_2$ and employing Eq. (2.11), Eq. (2.10) reduces to

$$\Delta(\lambda_2 - \lambda_1) = \frac{mg}{2AE}(1 - p_e)\lambda_1\left(\frac{l + 2x}{l + x}\right)\left[\frac{\sin(\phi + \theta/2)}{\sin\alpha}\right]\left(2\sin\frac{\theta}{2}\right) \tag{2.12}$$

Referring to Eq. 2.12, the following features of the proposed sensor are worth mentioning: (a) Ambient temperature fluctuation, acting on both the FBGs identically, leads to an identical shift of the Bragg wavelengths. As the sensor monitors tilt by measuring $\Delta(\lambda_2 - \lambda_1)$, influence of

the temperature gets automatically eliminated, making the sensor inherently temperature insensitive; (b) Sensitivity is proportional to $m/2$. Hence, sensitivity can be tuned to the desired value simply by choosing a rod of different mass (m); (c) For small tilt angles (up to 20°), the shift in wavelength difference is proportional to the applied tilt angle (θ); (d) Importantly, apart from the applied tilt angle θ, sensor response critically depends on the crucial design parameters l, x, ϕ and α. In order to design the sensor, one needs to incorporate appropriate values of these additional design parameters that can lead to the optimum response characteristics. Hence, effect of these additional design parameters needs to be investigated.

2.2.3 Sensor optimization

Theoretical modeling of the proposed design strategy for the development of tilt sensor reveals that the response characteristics depends on critical design parameters l, x, ϕ and α. This dependency is reflected in Eq. (2.12) through the two additional factors, namely, $(l+2x)/(l+x)$ and $\sin(\phi+\theta/2)/\sin\alpha$. Let us consider the factor $(l+2x)/(l+x)$ first. The value of this factor approaches to 1 when $l >> x$, and to 2 when $x >> l$. As the proposed sensor exploits the rotational tendency of the rod and the mass of the rod critically defines the sensitivity, length of the rod l has to be much larger than the radius of the wheel x. Consequently, this factor essentially serves as a multiplier with the value slightly greater than 1. On the other hand, $\sin(\phi+\theta/2)/\sin\alpha$ acts as the dominating factor in defining the sensitivity and the linearity characteristics of the proposed sensor.

In order to develop deeper understanding, sensor response is simulated while varying the values of ϕ, θ, and α. During the simulation, mass of the rod is taken to be 30g. These simulated response characteristics are plotted in Fig. 2.3, where the x-axes carry the applied tilt angle θ and the y-axes carry theoretically observed values of $\Delta(\lambda_2-\lambda_1)$. In these simulations, (a) tilt angle θ is varied in a step of 2° from -10° to +10°; (b) for a fixed value of ϕ, α is varied as 50°, 30°, 20°, 15°, 10° and 5°; and (c) ϕ itself is varied as 10°, 30°, 50°, and 70°. Following

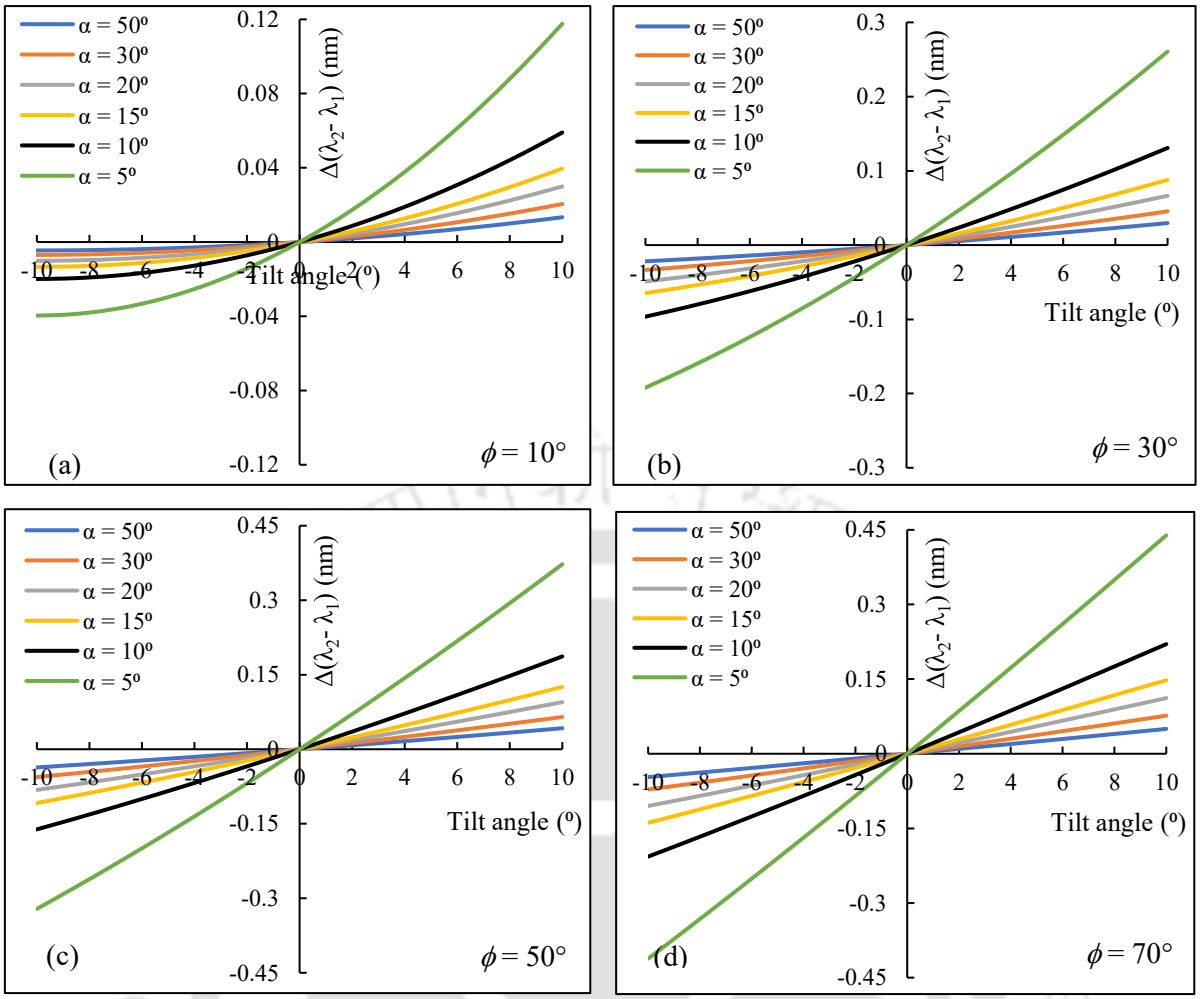

Figure 2.3: *Theoretical sensor response, $\Delta(\lambda_2 - \lambda_1)$ vs θ, at (a) ϕ = 10°, (b) ϕ = 30°, (c) ϕ = 50°, (d) ϕ = 70°*

observations can be made from Fig. 2.3: At lower value of ϕ, as an example when ϕ is fixed at 10° in Fig. 2.3(a), response of the sensor is nonlinear throughout the tilt angle variation range of ±10°. The nonlinear response is observed for all the values of α. As the value of ϕ is increased to 30° in Fig. 2.3(b), response of the sensor still remains nonlinear for all the values of α. Importantly, not only the nonlinear nature decreases within the θ range of ±10°, but the sensitivity also increases while moving from ϕ = 10° to ϕ = 30° at each value of α. Similar trend is observed when the value of ϕ is increased to 50° in Fig. 2.3(c). Increasing ϕ to 70° in Fig. 2.3(d), results in almost perfect linear response within the θ range of ±10°. Summarizing the observations, (i) at a fixed value of ϕ, decreasing the value of α results in a higher sensitivity.

The increment in sensitivity is observed to be nonlinear, which means that a lower value of α will result in significantly enhanced sensitivity of the proposed sensor. This is because of the fact that the response of the sensor depends on α through the term $\sin\alpha$ and this term appears in the denominator of the factor $\sin(\phi+\theta/2)/\sin\alpha$. Thus, the value of α should be opted as small as possible if one intends to achieve maximum sensitivity; (ii) at a fixed value of α, increasing the value of ϕ tends to make the nature of the response linear while increasing the sensitivity. To understand the reason behind the nature of the response characteristics being transformed from nonlinear to linear as ϕ increases, effect of $\sin(\phi+\theta/2)$ term in the numerator of the factor $\sin(\phi+\theta/2)/\sin\alpha$ needs to be analyzed. For the values of ϕ within the range of variations of θ (i.e., within ±10°), $\sin(\phi + \theta/2)$ is not constant. Rather, it acts as an increasingly multiplying factor within ±10°, thus contributing to the nonlinearity. However, if ϕ is chosen to be much larger than the range of θ variations (±10°) as in the case of Fig. 2.3(c) and (d), we can write,

$$\sin(\phi + \theta/2) \approx \sin\phi \tag{2.13}$$

Under this approximation, factor $\sin(\phi+\theta/2)/\sin\alpha$ ($\approx \sin\phi/\sin\alpha$) becomes effectively independent of θ. Thus, for a given value of α and larger values of ϕ, this factor acts merely as a constant multiplying factor with the ±10° range of θ; hence, leading to a linear response. In conclusion, for achieving optimum sensitivity and linear response within the designed dynamic range of ±10°, α should be as low as possible and ϕ should be as high as possible. Theoretical results in Fig. 2.3 depicts that the design parameters ϕ fixed at 70° and α fixed at 5° give rise to a linear response and highest sensitivity. Increasing the value of ϕ and decreasing the value of α will further increase the sensitivity. However, while realizing the sensor, it is the design constraints that limit the highest value of ϕ and the lowest value of α. Keeping the above findings and the design constraints into considerations, sensor was machined with the value of ϕ equal to 70° and the value of α equal to 14°.

2.3 Experimental

In order to design the sensor, a frictionless wheel was realized first. For this, a frictionless stainless-steel ball bearing (make: SKF, model: 608-Z, reference speed 1250 revolutions/sec, outer radius (o.r.) 11 mm, inner radius (i.r.) 4 mm, width 7 mm) was precisely and firmly fixed within an annular brass ring (housing) of i.r. 11 mm, o.r. 15 mm and thickness 10 mm. Thus the radius of the wheel x is fixed at 15mm. A brass rod of radius 4 mm was then rigidly fixed inside the ball bearing, which acted as an axle of the wheel. Another brass rod of length l (= 10 cm), diameter d (= 6.96mm) and mass m (= 31.94 g; mass-1) was used for realizing the sensor. One end of this rod was given semi-spherical shape whereas M3 threading was machined at the other end. This rod was fixed to the wheel; and this rod-wheel structure was then appropriately and rigidily fixed through the axle of the wheel to a L-shaped frame as depicted in Fig. 2.1 and Fig. 2.4. L-shaped frame was comprised of a vertical plate P_1 (14 cm×2cm×2cm) and a horizontal plate P_2 (8 cm×2cm×3cm). Specially designed strain tuning units (STUs) were fixed to both the plates. These STUs were not only crucial for pre-straining the fiber, but also played critical role in dictating/constraining the value of α. Two FBGs, FBG1 (λ_1 = 1552.112 nm) and FBG2 (λ_2 = 1546.206 nm) were inscribed at a pre-calculated separation on a hydrogen-loaded single-mode fiber using the phase-mask method. The fiber parameters were as follows: Young's modulus of material, $E = 7.2\times10^{10}$ N/m^2; cross-sectional area, $A = 1.23\times10^{-8}$ m^2; and photo-elastic coefficient, $p_e = 0.22$. FBG carrying optical fiber was fixed at the STU1, then at the top semi-spherical end of the rod and finally at the STU2, as depicted in Fig. 2.5. The fiber was pre-strained by an amount ~1500 $\mu\epsilon$. Following this, the sensor was mounted on the tilt platform (goniometer), which was capable of varying tilt within the range of ±10°. Photograph of the proposed FBG based tilt sensor is shown in Fig. 2.4. In order to carry out the experimental investigations, proposed sensor was connected to an FBG interrogator (Micron Optics, resolution 0.5 pm). The interrogator was interfaced to a computer in order to facilitate

real-time data acquisition through Micron Optics ENLIGHT software. Starting from −10° inclination, the sensor was tilted in a suitable and smallest step of 2° (dictated by the goniometer) to +10° (forward) and then reverted back to −10°(reverse). The wavelength shifts for both the FBGs corresponding to various applied tilt angles were recorded using the FBG interrogator.

2.4 Results and discussion

In order to characterize the response characteristics, proposed sensor was tilted with the help of goniometer. While doing so, wavelength shifts of both the FBGs were recorded in real-time

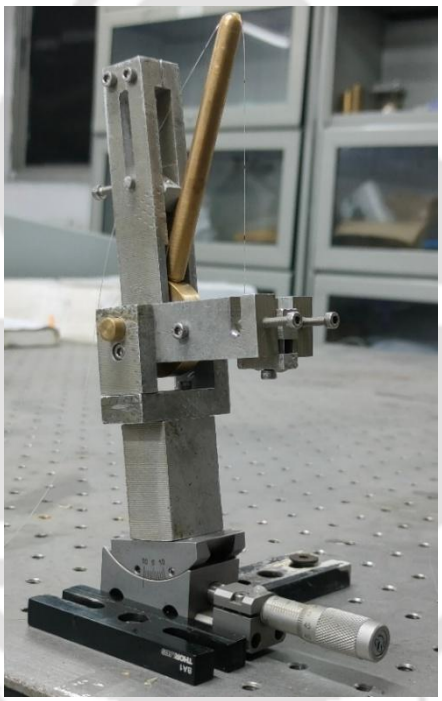

Figure 2.5: *Proposed FBG based tilt sensor*

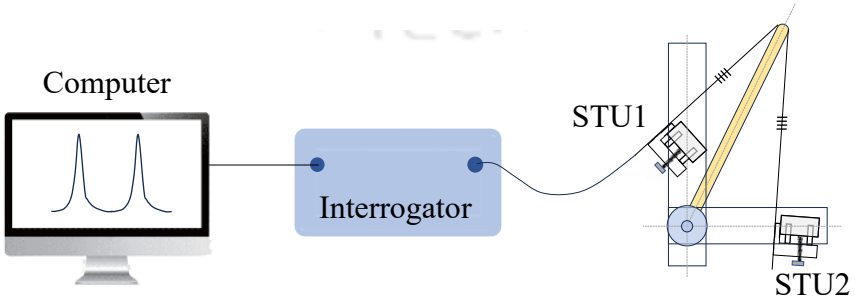

Figure 2.4: *Experimental setup for sensor characterization*

using the FBG interrogator. Observed time response of the two FBGs for the rod of mass-1 are depicted in the inset of Fig. 2.6. Left vertical axis represents responses of FBG1, whereas and right vertical axis represents responses of FBG2. In order to develop deeper understanding of the response characteristics, experimentally observed $\Delta(\lambda_2-\lambda_1)$, determined from the stabilized portion of the experimental response of individual FBGs, are plotted against the varying tilt angles in Fig. 2.6 for the forward (circles) as well as reverse (crosses) tilts. Theoretically predicted $\Delta(\lambda_2-\lambda_1)$ are also plotted (continuous line) in Fig. 2.6. It is worth mentioning that the experimental results match excellently with the theoretically predicted results. Theoretical as well the experimental sensitivities, both are observed to be 0.0162 nm/°. Further, the sensitivity remains identical for the forward and the reverse tilts. This establishes highly reversible nature of the sensor. Maximum discrepancy between the theoretical and the experimental responses is observed to be ±0.001 nm, which corresponds to an angular uncertainty of ±0.0617° for forward as well as reverse tilt variations. Accordingly, the accuracy of tilt angle measurement is observed to be ±0.062°. Importantly, angular resolution entirely depends on the wavelength resolution of the interrogation system. In the present research, the wavelength resolution of the interrogator was 0.5 pm. Consequently, tilt angle resolution is observed to be 0.0308°.

In order to investigate the tuning capability of the response characteristics, experiments were carried out by replacing the brass rod of mass-1 with another brass rod of mass-2 (59.07 g) (length l = 10 cm, diameter d = 9.50mm). Theoretically calculated and experimentally observed $\Delta(\lambda_2-\lambda_1)$ for this rod of higher mass are also depicted in Fig. 2.6 for forward (tilted squares) and reverse (triangles) tilt angle variations. In this case also, the experimental results match excellently with the theoretically predicted results. Theoretical as well the experimental

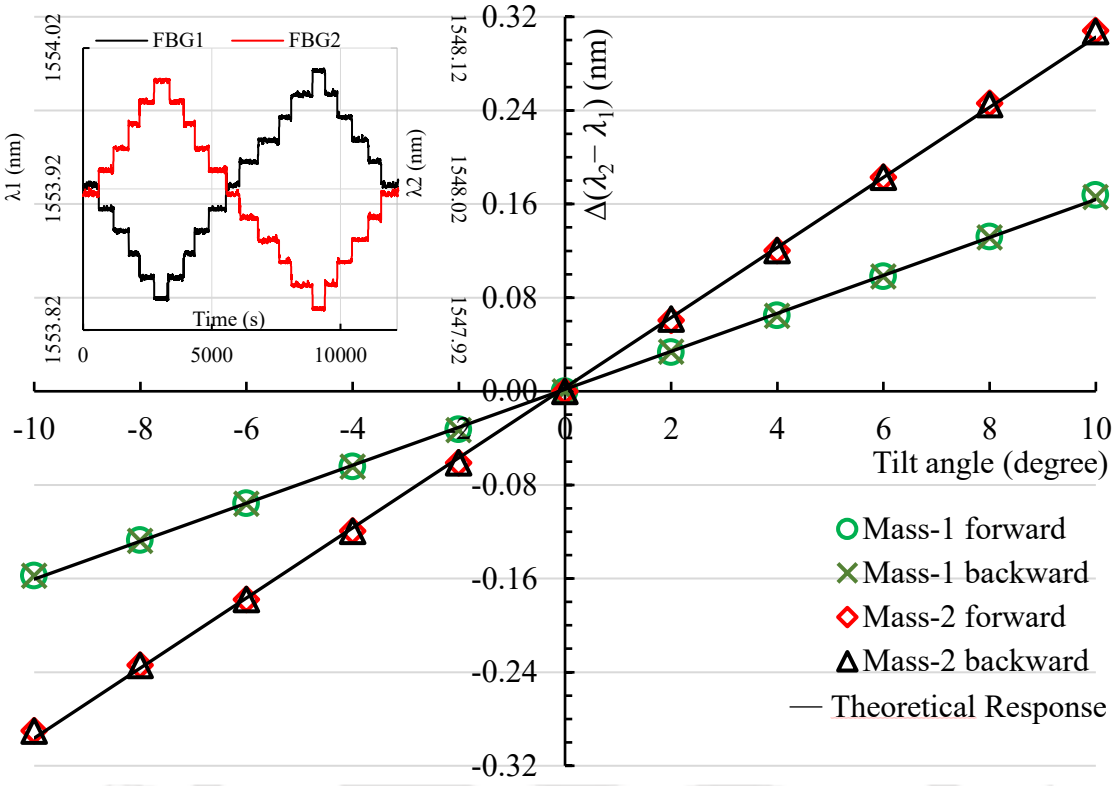

Figure 2.6: *Experimental response for two different masses (rods).*

sensitivities, both are observed to be 0.0300 nm/°. Further, the sensitivity remains identical for the forward and the reverse tilts. This, once again, establishes highly reversible nature of the sensor. Importantly, the observed sensitivity in this case is approximately 1.85 times higher than the sensitivity observed in the case when the proposed sensor employed rod of smaller mass (mass-1). This shows that the enhancement in the sensitivity aligns precisely with the ratio of the masses of the two rods, as predicted by the theoretical model presented in Eq. (2.12). This feature underlines the excellent capability of tuning the response characteristics of the proposed sensor simply by varying the mass of the rod. Further, the maximum discrepancy between the theoretical and the experimental responses is observed to be ±0.001 nm, which corresponds to an angular uncertainty of ±0.0333° for forward as well as reverse tilt variations. In addition, the accuracy of tilt angle measurement is observed to be ±0.033°; whereas the tilt angle resolution is observed to be 0.0167°.

Table 2.1: Comparison of performance characteristics of the proposed sensor

Author	Sensor dependency on mass of bob	Mass of bob (g)	Sensitivity (nm/º)	Accuracy	Maximum discrepancy (nm)	Angular resolution	Dynamic range
Guan *et al.* [74]	*m*	344	0.0752	±0.100º	±0.008	0.0070º	−09° to 03°
Au *et al.* [64]	*m*	170	0.0395	±0.051º	±0.002	0.0130º	−07° to 07°
Bao *et al.* [75]	*m*	528	0.0540	±0.270º	–	0.0190º	−20° to 20°
Bao *et al.* [76]	8*m*	500	0.0960	±0.200º	–	0.0130º	−20° to 20°
Yang *et al.* [77]	*m*	500	0.0740	±0.180º	–	0.0135º	0° to 40°
Ni *et al.* [79]	*m*	100	0.0537	–	±0.015	0.0090º	−10° to 10°
Chen *et al.* [80]	*m*	357	0.0600	±0.167º	±0.010	0.0067º	−15° to 15°
Li *et al.* [81]	*m*	5.3	0.0011	–	–	–	*−50° to 50°*
Aneesh *et al.* [82]	*m*	110	0.0626	±0.360º	–	0.0080º	−10° to 10°
Reported work	*m*/2	59.07	0.0300	±0.033º	±0.001	0.0167º	−10° to 10°

Next, the performance characteristics of the proposed sensor is compared with other FBG based tilt sensors reported in the literature. Table-I lists critically important parameters that are required for analyzing effective sensing abilities of a given sensor, such as, sensitivity, angular resolution, measurement accuracy, maximum discrepancy. Table-I also mentions the values of the mass (*m*) used in the reported sensors, and the dependency of sensitivity on the employed mass (*m*). At first glance, the sensitivity of the proposed sensor appears to be less than the sensitivities observed for all the reported sensors, except [82]. It is important to mention that the sensitivity varies in the linear proportion of *m*/2 for the proposed sensor (Eq. (2.12)). This means, the effective mass that played role in the sensing mechanism is half of the

employed mass. In comparison, not only the sensing mass used in other sensors (except [81]) were higher than the mass used in the present study, but the sensitivities varied in linear proportion to either *m* or 8*m*. This means that the effective mass that played role in the sensing mechanism in these sensors were either the employed mass itself (hence, double in comparison to the effective mass of the proposed sensor), or, eight times of the employed mass (hence, sixteen (16) times in comparison to the effective mass of the proposed sensor). Scaling the mass (mass-2) employed in the present study to the values employed in the other sensors, sensitivity of the proposed sensor will surpass all except [76], which reported highest tilt angle measurement sensitivity of 0.0960 nm/°. Importantly, in the case of [76] employed mass was 500g, which is ~ 8.47 times higher than 59.07g (mass-2 of the proposed sensor). Alongside, the sensitivity dependency on this mass was in a proportion to 8*m*. Combining equivalency of both of these factors, namely, the eight times dependency of sensitivity on the mass and the mass itself being nearly 8.47 times higher, the expected sensitivity of the reported sensor would be ~ 4.0608 nm/°. This is significantly (~ 42.3 times) higher than the sensitivity reported in [76]. At the same time, it is also important to mention that scaling the mass, used in the present research, to a higher value will substantially improve the observed accuracy and the resolution of the proposed sensor.

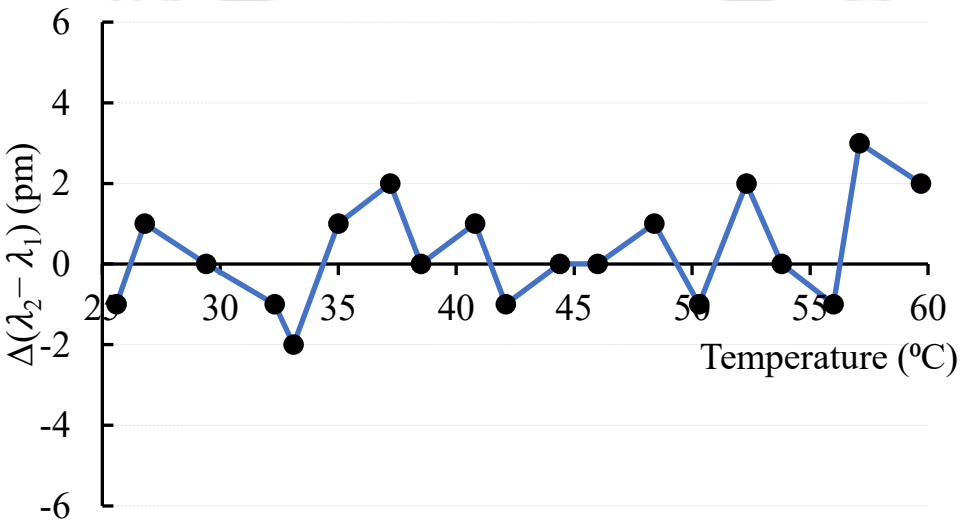

Figure 2.7: *Thermal response of the tilt sensor with rod-2 while inclined at a fixed angle*

It is very crucial to mitigate the ambient temperature induced cross-sensitivity for the proposed sensor that is crucial in real-field applications. While the sensor is inherently designed to fulfill this requirement, it is important to experimentally examine the effect of ambient temperature fluctuations on the sensor performance. For this, water bath test was conducted. Proposed sensor employing rod of mass-2 was placed in a water tank at a fixed inclination. Water was poured in the tank to the level that ensured that the sensor remained completely immersed in it. Temperature of the water inside the tank was first raised to 60°C, and then allowed to cool down naturally to the room temperature (~25°C). During this cooling process, wavelength difference $\Delta(\lambda_1-\lambda_2)$ was measured at regular intervals. Fig. 2.7 illustrates the thermal response of the proposed sensor. As can be observed, maximum discrepancy in the wavelength difference is within ±3pm. This discrepancy is about 121 times less than the absolute wavelength shift, an uncompensated FBG will experience when exposed to an identical temperature variation condition. The extremely low thermally-induced discrepancy, reflecting the ability to substantially eliminate the temperature cross-sensitivity, establishes the temperature independent nature of the proposed tilt sensor – an inherent requirement for real-field applications where continuous ambient temperature variation is inevitable.

Further, Stability, reliability, and repeatability are other crucial parameters to evaluate the sensor performance. For this, long term performance of the sensor was examined. Experiments were repeated over three separate days keeping an interval of two days. Fig. 2.8 depicts the sensor outputs corresponding to four different tilt angles (2°, 4°, 6°, 8°). The sensor output was observed to be consistent over all those repetitive experiments. The inset shows the corresponding date for 2°. The maximum variation in the sensor output, compared to day one at all the tilt angles, was found to be of the order of 10^{-3} nm. This establishes an excellent reliability and repeatability of the proposed sensor. This feature, along with an effective sensing

capability depicted by good sensitivity, maximum discrepancy, accuracy, reversible and tunable response characteristics make the proposed sensor of great practical importance.

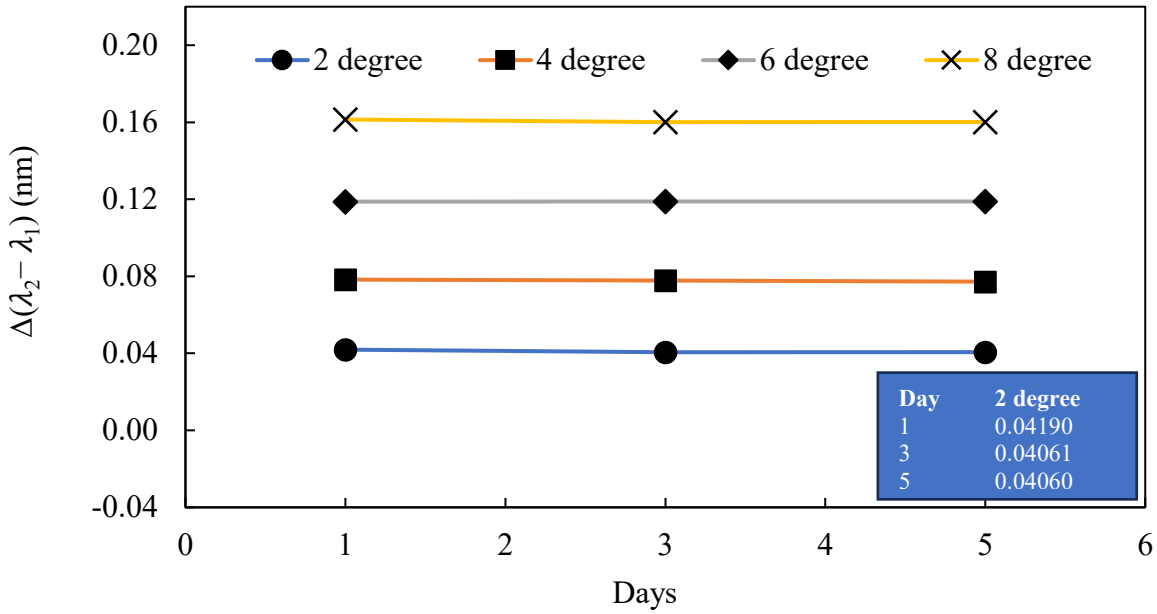

Figure 2.8: *Repeatability and reliability test*

2.5 Conclusion

In this chapter, a novel design strategy to develop a non-pendulum type temperature insensitive, FBG-based all optical tilt sensor is proposed. Rigorous theoretical investigations are carried out in order to establish various design parameters of the proposed sensor for achieving an optimum response characteristic. On the basis of the findings of the theoretical investigations, FBG-based tilt sensor is machined and experimentally investigated to establish the response characteristics across the dynamic range of ±10°. Proposed sensor exhibits excellent capability of tuning the response characteristics, which is reflected by the observed response as the rod of mass-1 (lower mass) is replaced with the rod of mass-2 (higher mass). Importantly, even employing mass-2 which is much smaller in comparison to the mass employed in the other reported tilt sensors, an excellent sensitivity of 0.0300 nm/° is observed for the proposed sensor. It is observed that by suitably employing an equivalent mass in the proposed design strategy, a

far better sensitivity can be achieved in comparison to the highest sensitivity reported in the literature. Further, the experimentally observed response matches excellently well with the theoretical response. This is reflected in the minimal maximum discrepancy of ±0.001 nm. Experimental observations establish high degree of reversible response characteristics with an excellent accuracy of ±0.033° and an angular resolution of 0.0167°, even when the employed mass is much smaller. Furthermore, the sensing principle depends on mapping tilt angle into the shift in wavelength difference between the FBGs. This makes the sensor inherently immune to ambient temperature fluctuations, as established by water bath test. The sensor is also characterized with high degree of repeatability and reliability. Hence, the proposed sensor is well suitable for various industrial/engineering applications. Although the sensor design was characterized with good sensitivity and high accuracy, the angular resolution could not be achieved as good as in comparison to the sensors developed and reported in literature. Hence, there remains a need to investigate alternative design approaches to further enhance the overall performance characteristics. This laid the foundation of the research work discussed in the next chapter.

Chapter 3 : Development of Fiber Bragg Grating Based Temperature Insensitive Novel All Optical Tilt Sensor

3.1 Introduction

The previous chapter described the development of temperature-insensitive FBG-based tilt sensor that employed rod and wheel system. Notably, apart from the length of the rod and the diameter of the wheel, the sensor response was inherently dependent on three design parameters, namely, mass of the employed rod (m), angle of the rod made from the horizontal (ϕ) and the angle FBG made with respect to the rod itself (α). These features facilitated the ability of tuning the response characteristics as per the desired applications. Even though, the sensor was characterised with a good sensitivity and accuracy, there is ample scope to improve the overall response characteristics of the tilt sensor.

This chapter introduces another non-pendulum type novel design strategy for the development of a temperature-insensitive FBG-based tilt sensor. By varying the loaded mass used in the sensor, the response characteristics can be fine-tuned without requiring complex adjustments. Response characteristics of the proposed sensor is theoretical analyzed and experimentally established. Apart from that, as the sensor design maps the applied tilt angle variations in terms of the Bragg wavelength separation between two FBGs, this makes the sensor inherently temperature independent. These features of the proposed tilt sensor facilitate it to meet critical operational standards of real-field monitoring applications.

3.2 Experimental

3.2.1 Sensor Design and Construction

Fig. 3.1 illustrates the design strategy of the proposed sensor, where a giant wheel is mounted in the vertical plane with its axle rigidly fixed onto two parallel vertical stands (refer to Fig. 3.2 for 3-D view). To design the sensor, frictionless stainless-steel ball-bearing (make: SKF, model: 608-z, reference speed 1250 revolutions/sec, inner diameter (i.d.) 8 mm, outer diameter (o.d.) 22 mm, width 10 mm) was rigidly and perfectly fixed within an annular brass (housing) ring (i.d. 22 mm, o.d. 35 mm, thickness 10 mm). This structure was then fixed rigidly at the center of a brass rod (axle) of length 10 cm and diameter 8 mm. The giant wheel comprised of a big circular brass ring (i.d. 77 mm, o.d. 87 mm, thickness 10 mm), rigidly fixed to the ball-bearing (through the housing ring) using three equally spaced (120° angular separation) sturdy stainless-steel spokes (Fig. 3.1). A small rod was symmetrically and rigidly fixed at the center of the width of the wheel. This rod was used for mounting equal masses ($m/2$ and $m/2$) on both the sides of the wheel so that the perfect vertical orientation of the wheel didn't get

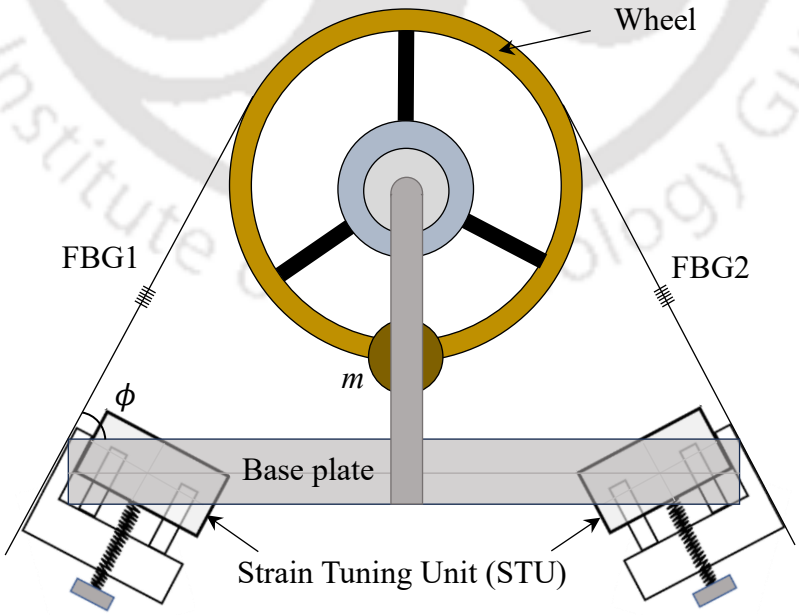

Figure 3.1: *Schematic diagram of the proposed FBG tilt sensor*

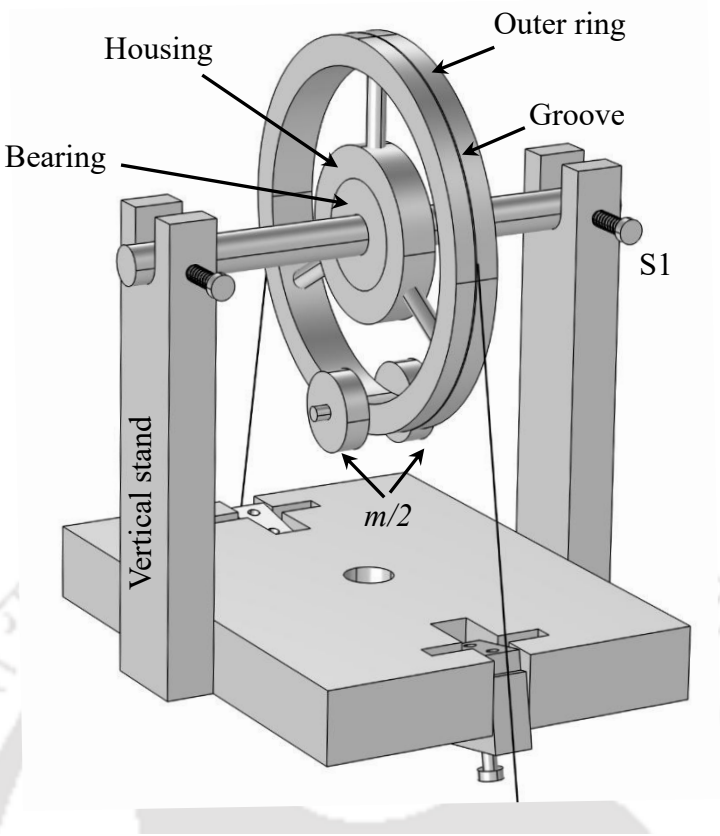

Figure 3.2: *Frictionless wheel system*

compromised (Fig. 3.2). A groove was machined onto the center of the outer surface of the wheel for attaching an optical fiber carrying FBG. This frictionless wheel system was fixed to the rectangular metallic (aluminum) base plate of dimension 11cm × 6cm × 1.5cm using two identical metallic (aluminum) vertical plates. Identical 'U' shaped cut was made at the top end, and at the middle of the width of these vertical plates to host the axle of the wheel (Fig. 3.2). Two M3 screws (S1) were used to fastened the axle on the vertical plates, guaranteeing no undesired shift in the position of the wheel system. These side plates were fixed at the centre of the lateral surface of the longer side of the base plate. In this arrangement, vertical plane carrying the giant wheel bisects the base plate along the 6 cm long sides. Further, in order to fix the FBG carrying fiber and to pre-strain it precisely, two specially designed strain tuning units (STUs) were fixed with in the slot created at the center of both the short edges of the base plate (Fig. 3.1).

Two FBGs (λ_1 and λ_2) were written onto a single optical fiber with pre-calculated inter-FBG separation. This fiber was glued at the center of the first STU. Then, going through the groove made on the wheel, it was glued at the top of the wheel. Finally, it was glued to the second STU. Thus, the fiber made two inclined fiber arms, each having curved vertex at the top of the wheel. While fixing the fiber, FBGs were maintained at the center of each fiber arm. All the FBGs were pre-strained by an equal amount through STUs. Photograph of the developed sensor is shown in Fig. 3.3. In this design, if the wheel is not constrained by the fiber, the topmost point of the wheel is free. If the mass m gains a tendency to be displaced clockwise (anticlockwise), the topmost point of the wheel will also gain a tendency to get displaced in the clockwise direction (anticlockwise). Thus, if an optical fiber is attached at the top of the wheel, strain will get redistributed in the two arms of the fiber in the opposite direction. Total dimension of the sensor is 11 cm × 10 cm × 13.5 cm.

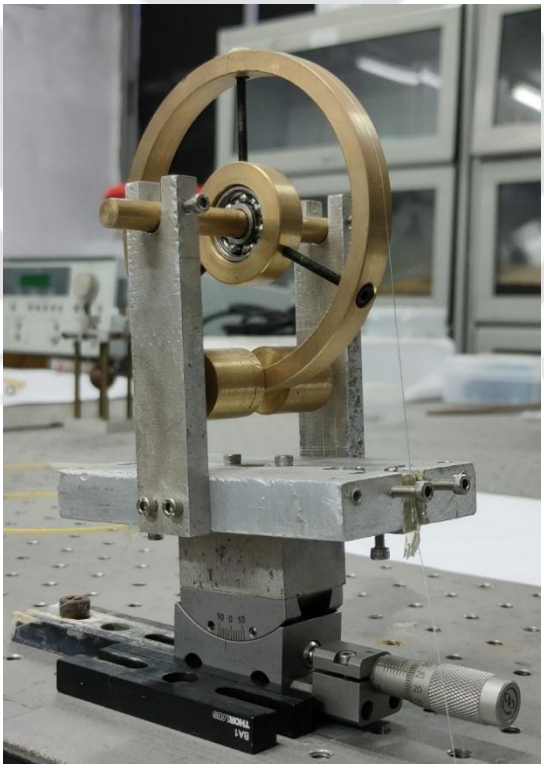

Figure 3.3: *Proposed FBG tilt sensor*

3.2.2 Sensing Principle

Fig 3.4 represents the force diagram of the sensor. At zero inclination, the tensions in both the fiber arms are defined as T_1 and T_2. At equilibrium, the net torque acting around the center of the axle (O) is zero. Hence,

$$\tau_c - \tau_{cc} = 0 \quad \Rightarrow rT_1 - rT_2 = 0 \quad \Rightarrow T_1 = T_2 \tag{3.1}$$

Here, τ_c and τ_{cc} are clockwise and counter-clockwise torque w.r.t. the center of the axle. When the sensor is inclined at an angle θ in the vertical plane, the tension in both the gratings gets redistributed to T_1' (= T_1 + ΔT_1) and T_2' (= T_2 + ΔT_2), respectively. This is because, if not constrained, the wheel has a tendency to rotate through the mounted mass. At equilibrium, the net torque acting around the center of axle (O) is zero. Hence,

$$\tau_c - \tau_{cc} = 0 \quad \Rightarrow rT_1' - rT_2' - mgrsin\theta = 0 \tag{3.2}$$

$$\Rightarrow \Delta T_1 - \Delta T_2 = mgrsin\theta \tag{3.3}$$

Here, m is the mass of the mounted weight, g is acceleration due to gravity. Mechanical strain induced in both of the FBG arms due to the tensions T_1 and T_2 can be written as,

$$\Delta\epsilon_1 - \Delta\epsilon_2 = (\Delta T_1 - \Delta T_2)/AE \tag{3.4}$$

The strain-induced wavelength shifts for an FBG, centred a wavelength (λ) is given by [39],

$$\frac{\Delta\lambda}{\lambda} = (1 - P_e)\Delta\epsilon \tag{3.5}$$

Here, P_e is photo-elastic coefficient of the fiber. Hence, Bragg wavelength shift for both the FBGs (λ_1 and λ_2), can be written as,

$$\frac{\Delta\lambda_1}{\lambda_1} - \frac{\Delta\lambda_1}{\lambda_1} = (1 - P_e)(\Delta\epsilon_1 - \Delta\epsilon_2) \tag{3.6}$$

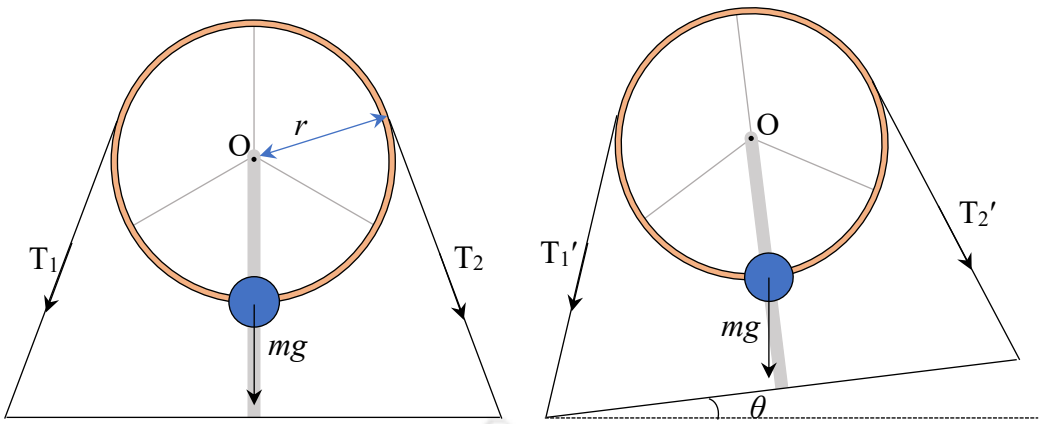

Figure 3.4: *Force diagram of the proposed FBG tilt sensor at zero inclination (left) and at θ° inclination (right)*

Using Eq. (3.3), Eq. (3.4) and Eq. (3.6), the wavelength shift difference for both the FBGs is expressed as (assuming $\Delta\lambda_i << \lambda_i$; $i = 1, 2$; $\lambda_1 \approx \lambda_2$),

$$\Delta(\lambda_1 - \lambda_2) = (1 - P_e)\frac{mg\lambda_1}{AE} \cdot sin\theta \tag{3.7}$$

As evident from Eq. (3.7), sensitivity is directly proportional to the mounted mass (m). With the provision of varying this mass without disturbing the mechanical stability of the proposed sensor, one can tune the sensitivity to the desired value by simply varying m. Eq. (3.7) also depicts that for small tilt angles (up to 20°), the difference in the wavelength separation is directly proportional to θ. Further, any temperature variation during the experiment will shift FBG's wavelengths in the same direction by the same amount. Hence, the wavelength separation between the two FBGs will always be insensitive towards the ambient temperature variations. This makes the sensor response inherently temperature independent.

3.2.3 Sensor Characterisation

Two FBGs, written onto a hydrogen-loaded single-mode fiber employing phase-mask method, were used in the proposed sensor. The parameters of the fiber are: cross-sectional area, A = 1.2266×10^{-8} m^2, Young's modulus of material, $E = 7.2\times10^{10}$ N/m^2, photo-elastic coefficient, P_e = 0.22. In absence of any external strain, the peak reflection wavelength of FBG1 (λ_1) are 1552.228 nm and that of FBG2 (λ_2) are 1546.168 nm. Fiber carrying both the FBGs (λ_1 and λ_2) was first glued at the centre of the first STU. Then, going through the groove made on the wheel, it was glued at the top of the wheel. Finally, it was glued to the second STU. Following this, both the FBG arms were pre-strained using the STUs. Finally, one end of the fiber was connected to FBG interrogator (Micron Optics, 0.5 pm resolution). The interrogator was interfaced with a computer for real-time data acquisition using Micron Optics ENLIGHT software. Two equal masses, of joint mass m (53.48 g, 73.12 g and 179.91 g), were mounted on the wheel. Fig. 3.5 shows the experimental setup. Following this, the sensor was mounted on the available tilt platform that was capable of applying tilt within ±10°. This was a laboratory constraint. For the experiment, the sensor was tilted in suitable steps (dictated by the goniometer) starting from −10° inclination in the plane of the wheel to +10° (forward) and then reverted back to −10° (reverse). The wavelength shifts for the FBGs, $\Delta(\lambda_1-\lambda_2)$, at different tilt angle variations were recorded using the FBG interrogator.

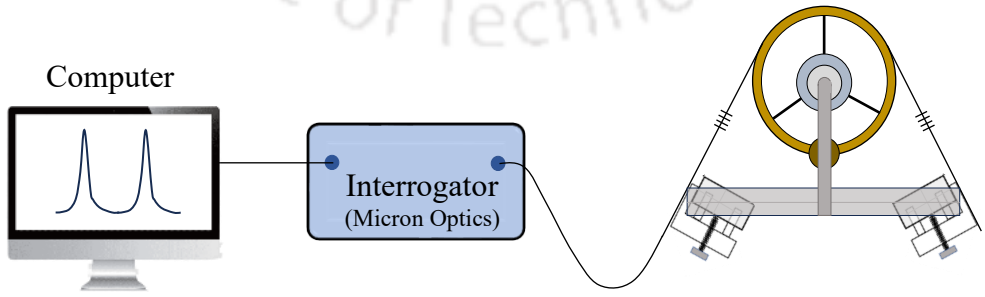

Figure 3.5: *Experimental Setup for sensor characterization*

3.3 Results and Discussions

In order to analyse the response characteristics of the proposed tilt sensor thoroughly, two equal masses of joint mass 53.48 g ($m = m_1$) were mounted on the wheel and the sensor was mounted on goniometer. Starting from −10º inclination in the plane of the wheel (containing FBG1 and FBG2), sensor was tilted in the vertical plane in suitable steps (dictated by the tilt platform) to +10º (forward) and then the sensor was reverted back from +10º to −10º (reverse). The Bragg wavelength of both the FBGs (FBG1 and FBG2) were recorded throughout the experiment using the interrogator. The measured response for $m = m_1$ is depicted in the inset of Fig. 3.6. Left vertical axis and right vertical axis represents the responses of FBG1 and FBG2, respectively, against time. For a deeper understanding of the sensor's response, experimentally observed $\Delta(\lambda_1-\lambda_2)$, from the stabilized portion of the response are plotted against the varying tilt angles in Fig. 3.6, for the forward (-10º to 10º) and reverse tilt (10º to -10º). It also depicts the theoretically calculated sensor response as well. As evident from Fig. 3.6, the sensor's response, $\Delta(\lambda_1-\lambda_2)$, is linear for both forward and reverse tilt variations, as anticipated by Eq.

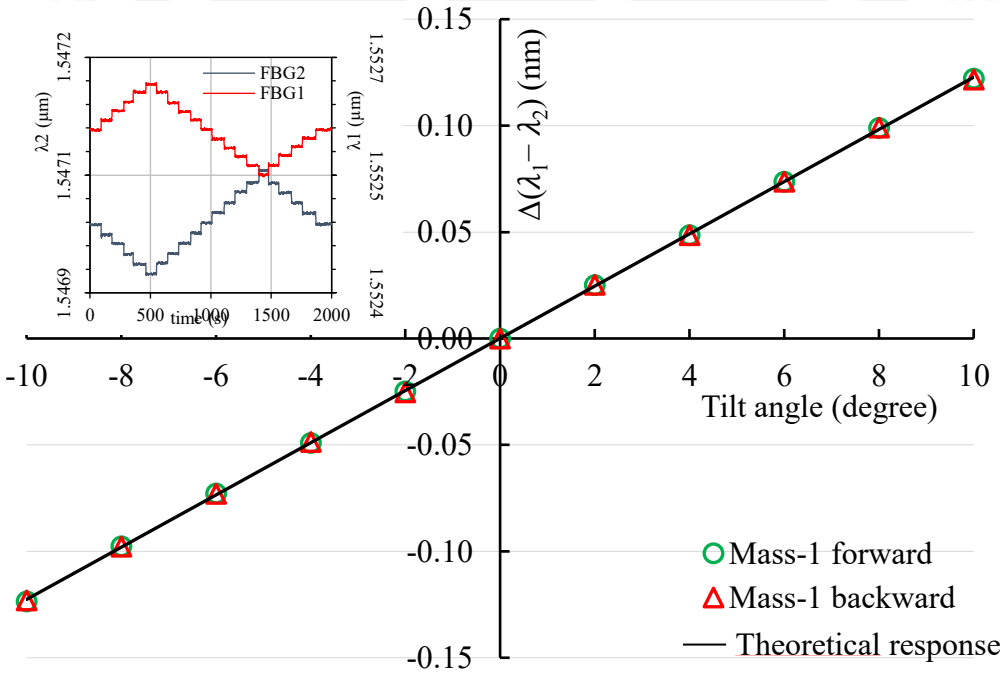

Figure 3.6: *Variation of $\Delta(\lambda_1-\lambda_2)$ for forward & backward tilt angle variations employing m_1*

(3.7). The measured sensitivities for both forward (-10º to 10º) and reverse (10º to -10º) tilt angle variations are 0.0123 nm/º. This exactly same sensitivity for both the forward and reverse tilt variations demonstrate the perfectly reversible nature of the sensor. It is also crucial to note that, the experimental results matched excellently with the theory. Maximum discrepancy between experimental and theoretical response is observed to be ±0.001 nm. This corresponds to a maximum angular uncertainty of ±0.0813º for both forward and reverse tilt angle variations. With a wavelength resolution of 0.5 pm provided by the interrogator, the sensor achieved an angular resolution of 0.0404°. The accuracy of tilt angle measurement was determined to be ±0.0808°.

In order to investigate capability of tuning the response characteristics, as described by the sensor design principal [Eq. 3.7], experiments were repeated by replacing the total mass ($2\times m/2$) loaded onto the wheel by 73.12 g (m_2) and 179.91 g (m_3). Same experimental procedures, that were conducted with the lighter mounted mass (m_1), were repeated for the sensor equipped with the heavier mounted masses (m_2 and m_3). Fig. 3.7 illustrates the wavelength response of each FBG in the proposed sensor during forward tilt cycles (-10º to +10º) and reverse tilt cycles (+10º to -10º) in the vertical plane. To evaluate the actual sensor response characteristics with the mounted masses m_2 and m_3, the experimentally observed $\Delta(\lambda_1-\lambda_2)$ for the forward tilt (-10º to 10º) and reverse tilt (10º to -10º) is presented in Fig. 3.7, along with the theoretically calculated responses. Figure 3.7 also consists the sensor response characteristics with the mounted masses m_1, for comparison. As evident in Fig. 3.7, the sensor's response, $\Delta(\lambda_1-\lambda_2)$, is linear for both forward and reverse tilt variations with both the higher masses, as dictated by Eq. (3.7). The measured sensitivities for both the forward (-10º to 10º) and reverse (10º to -10º) tilt angle variations are observed to be 0.0169 nm/º and 0.0415 nm/º, for the mounted masses m_2 and m_3 respectively. This exactly same sensitivity for both the forward and reverse tilt variations demonstrate the perfectly reversible nature of the sensor. It

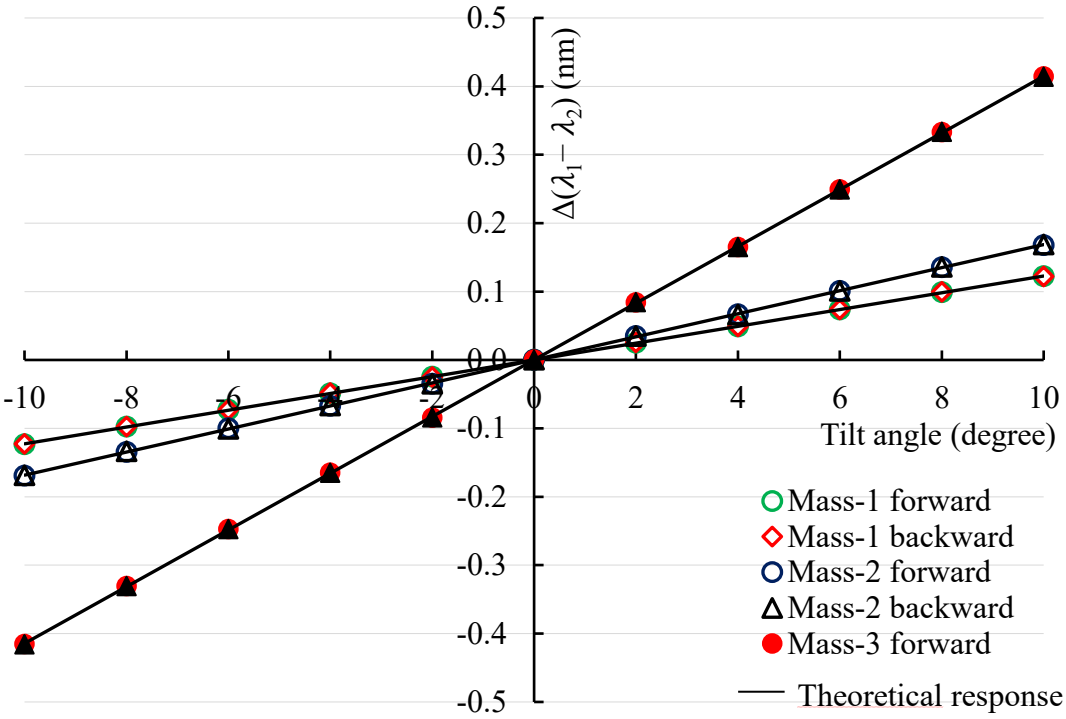

Figure 3.7: *Variation of $\Delta(\lambda_1 - \lambda_2)$ for forward and backward tilt angle variations employing m_1, m_2 and m_3*

is also crucial to note in these observations that, the experimental results matched excellently with the theoretical response. Maximum discrepancy between experimental and theoretical response is observed to be ±0.001 nm. This corresponds to a maximum angular uncertainty of ±0.0592º for m_2 and ±0.0241º for m_3, during both forward and reverse tilt angle variations. Considering the wavelength resolution of 0.5 pm provided by the interrogator, the sensor achieved an angular resolution of 0.0295° and accuracy of tilt angle measurement ±0.0591° for m_2. In case with the mounted mass m_3, the sensor achieved an angular resolution of 0.0120° and accuracy of tilt angle measurement ±0.0240°.

To analyze the effect of varying mass on the sensor performance, the sensor response characteristics for all the three masses is listed in Table 3.1. A notable characteristic of the proposed sensor, evident from Table 3.1, is that when the mounted mass is increased from m_1 to m_2 by a factor of 1.37, the sensitivity also increases by the exactly same ratio. Similarly, when the mounted mass is increased from m_2 to m_3 by a factor of 2.46, the sensitivity also

increases by the exactly same ratio. Additionally, as the mounted mass increases, the observed resolution and measurement accuracy seems to improve significantly.

Table 3.1: Summary of performance characteristics of the proposed sensor

Mass (*m*)	Sensitivity	Resolution	Max. Discrepancy (nm)	Max. Angular Uncertainty	Accuracy
53.48 g	0.0123 nm/º	0.0404°	±0.001	±0.0813º	±0.0808°
73.12 g	0.0169 nm/º	0.0295°	±0.001	±0.0592º	±0.0591°
179.91 g	0.0415 nm/º	0.0120°	±0.001	±0.0241º	±0.0240°

Table 3.2: Comparison of performance characteristics of the proposed sensor

Author	Sensor dependency on mass of bob	Mass of bob (g)	Sensitivity (nm/º)	Accuracy	Maximum discrepancy (nm)	Angular resolution
Guan *et al.* [74]	*m*	344	0.0752	± 0.100°	±0.008	0.0070°
Au *et al.* [64]	*m*	170	0.0395	± 0.051°	±0.002	0.0130°
Chen *et al.* [80]	*m*	357	0.0600	± 0.167°	±0.010	0.0067°
Bao *et al.* [75]	*m*	528	0.0540	± 0.270°	–	0.0190°
Bao *et al.* [76]	8*m*	500	0.0960	± 0.200°	–	0.0130°
Yang *et al.* [77]	*m*	500	0.0740	± 0.180°	–	0.0135°
Ni *et al.* [79]	*m*	100	0.0537	–	±0.015	0.0090°
Li *et al.* [81]	*m*	5.3	0.0011	–	–	–
Aneesh *et al.* [82]	*m*	110	0.0626	± 0.360°	–	0.0080°
This work	*m*	179.91	0.0415	± 0.024°	±0.001	0.0120°

Next, important parameters that are critical for an efficient measurement of tilt angle, are listed in Table 3.2 for the proposed as well as other tilt sensors for comparative analysis. This table also highlights value of the employed mass and sensitivity dependency on it. As can be observed, the best tilt angle measurement accuracy and the lowest maximum discrepancy are observed for the proposed sensor. By scaling the mass used in present study to the values used for other sensors, sensitivity of the proposed sensor will surpass all except [76], which reports highest sensitivity of 0.0960 nm/°. Incorporating equivalency of sensitivity dependency on 8*m* and *m* being 2.78 times larger as in [76], the expected sensitivity of the proposed sensor would be 0.9230 nm/°. This is almost 10 times higher than the sensitivity reported in [76]. Importantly, accuracy and resolution both will substantially improve upon scaling the mass used in this research to a higher value. It is important to note that the measured tilt range of the proposed sensor was constrained by the maximum tilt span (±10°) of the available laboratory goniometer.

It is very important to eliminate the effect of ambient temperature on the proposed sensor. Although, the sensor is designed to meet this requirement, still, effect of temperature on the performance of the sensor was examined by conducting water bath test. For this, sensor

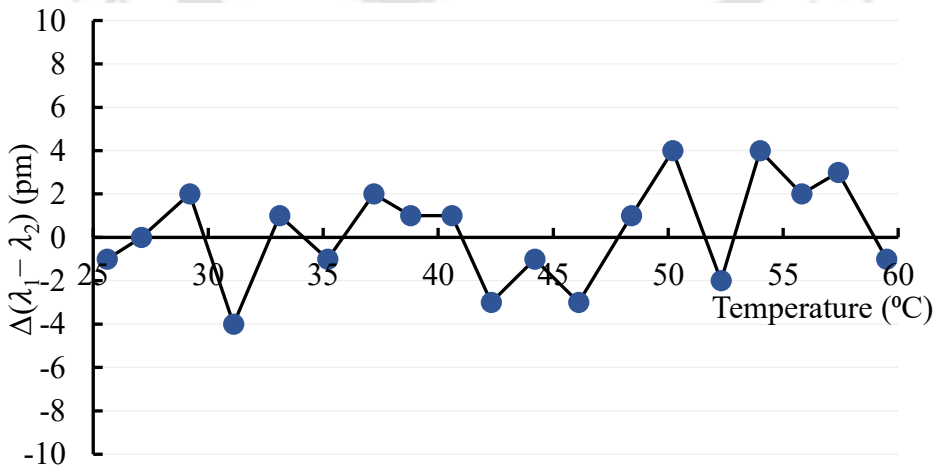

Figure 3.8: *Thermal response of the tilt sensor with mounted mass - m_3 while inclined at a fixed angle of* 4°

carrying mass m_3 and inclined at a fixed angle 4° was placed in a chamber. Water in the chamber was maintained initially at ~60°C and then allowed to cool down naturally to the room temperature (~25°C). Measured wavelength separation $\Delta(\lambda_1-\lambda_2)$ during the cooling down period is depicted in Fig. 3.8. The maximum discrepancy is observed within ±4pm, which is about 92 times less in comparison to the shift observed by an uncompensated FBG for the same temperature variation. This ensures temperature independent tilt measurement.

Finally, Stability, repeatability and reliability are other critical parameters to evaluate the performance of the sensor. Hence, long-term performance of the sensor was examined. For this, experiments were repeated over three separate days with an interval of two days. Observed results are shown in Fig. 3.9 for four different tilt angles (2°, 4°, 6°, 8°) for the sensor comprising m_3. The results show that the sensor output remained almost constant over the time period. The inset shows the corresponding date for 2°. Maximum variation in the sensor output, compared to day one at all the inclinations, is observed to be of the order of 10^{-4} nm. This shows an excellent reliability and repeatability of the developed sensor. Further, an effective sensing capability with very high accuracy, better angular resolution, better sensitivity combined with highly reversible and reliable response make the reported sensor of great practical importance..

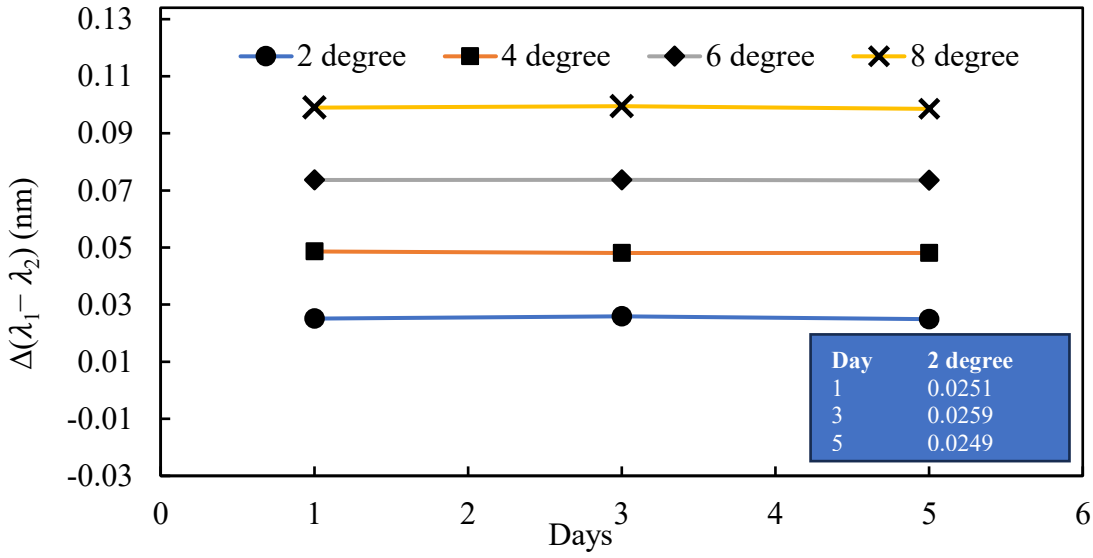

Figure 3.9: *Repeatability and reliability test*

3.4 Conclusion

In this chapter, the development of a temperature-insensitive all-optical tilt sensor based on FBG is described. The sensor employs a novel design with a non-pendulum approach and two FBGs mounted on a mechanically stable structure to capture tilt angles. The key feature of the sensor is its ability to tune its response characteristics by simply varying the mounted mass onto it. Response characteristics of the proposed sensor is theoretical analysed and experimentally established for three different mounted masses over a tilt range of -10° to +10°, dictated by the available goniometer. Linear and highly reversible responses were observed for all the three masses. An excellent agreement is observed between theoretically predicted and experimentally obtained responses. An excellent sensitivity of 0.0415 nm/°, that can be further tuned to the desired value, along with remarkable accuracy of ±0.024°, extremely low maximum discrepancy of ±0.001 nm, an angular resolution of 0.012° and an angular uncertainty of approximately ±0.0241° are observed for the sensor. The sensor is also characterized with high degree of reversibility, reliability and repeatability. While temperature cross-sensitivity is a common challenge for FBG sensors, this design overcomes it by mapping the wavelength separation modulation between two FBGs to decode tilt information. Thus, it effectively renders the sensor inherently temperature insensitive, making it suitable for practical industrial and engineering applications. The sensor design reported in this chapter exhibited much better sensor response in comparison to the sensor developed and reported in chapter 2. However, there still remains a need to investigate alternative design approaches. The next chapter of the thesis focuses on further improvement of the performance characteristics for an FBG-based all optical tilt sensor.

Chapter 4 : Fiber Bragg Grating Based Temperature-Insensitive Tilt Sensor with Optimum Response Characteristics

4.1 Introduction

Building upon the findings and advancements detailed in the previous chapter, the pursuit of enhanced sensor performance continues in this chapter. As observed, the tilt sensor reported in the previous chapter demonstrated exceptional sensitivity of 0.0415 nm/º, angular resolution of 0.012º and accuracy of ±0.024º. These parameters of the performance characteristics are far better than the parameters of various tilt sensors reported in the literature. However, for many engineering applications, a much higher tilt angle measurement sensitivity is required.

This chapter presents another novel pendulum type design strategy for the development of a temperature-insensitive, FBG-based all-optical tilt sensor, in order to achieve significant improvements in the response characteristics. The research includes both theoretical analysis and extensive experimental investigations to establish the sensor response characteristics under varying tilt angles. The experimental response characteristics align excellently with the theoretical predictions. A remarkable agreement is observed between theoretical predictions and experimental results, with a minimal maximum discrepancy of ±0.001 nm. The sensor is tested under various conditions, including different tilt angles and masses. The tunability of the sensor is demonstrated by varying the mass attached to the pendulum, which allows the sensitivity to be adjusted as required. A repeatability test is also conducted, where the sensor is subjected to the same tilt angles over multiple days. The results show minimal variation in the sensor's output, confirming its reliability and repeatable performance. Furthermore, temperature effects are effectively mitigated by leveraging the differential response of the FBGs, neutralizing temperature-induced wavelength shifts. Comparative analysis with other

sensors in the literature highlights the proposed design's superior performance, establishing it as a reliable and finely tunable solution for tilt sensing in real-world applications

4.2 Experimental

4.2.1 Sensor Design and Construction

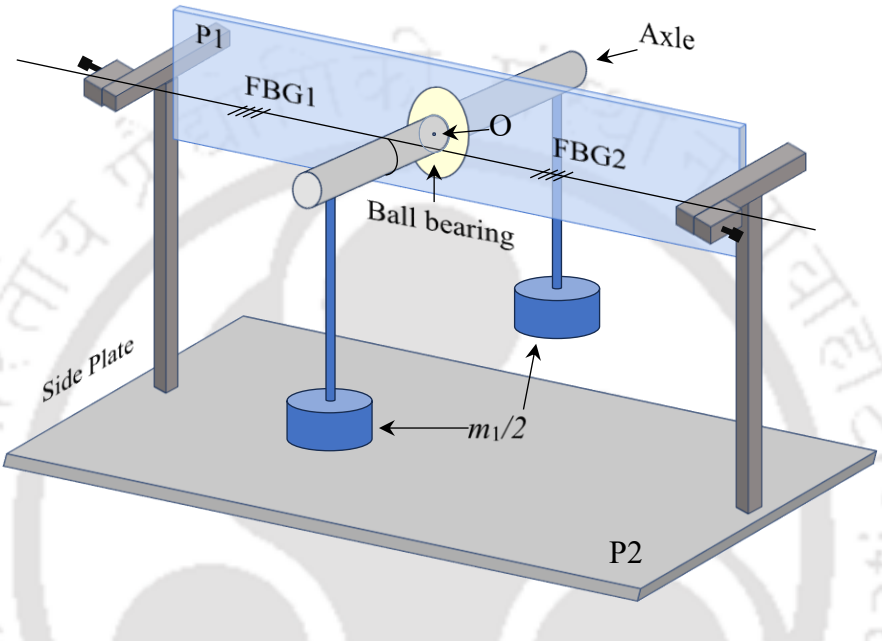

Figure 4.1: *Schematic diagram of the proposed FBG based tilt sensor*

The schematic diagram of the proposed sensor is depicted in Fig. 4.1, which consists of double pendulum having a common axle. To design the sensor, a frictionless stainless-steel ball-bearing (make: SKF, model: 608-Z, reference speed 1250 revolutions/sec, inner diameter 8 mm, outer diameter 22 mm, width 7 mm) is rigidly and perfectly fixed inside a hole that was made at the centre of a rectangular aluminium plate (P1) of dimensions 10cm × 3cm × 1cm. The hole has the diameter equal to the outer diameter of the ball-bearing. Following this, a

brass rod (axle) of radius '*r'* is rigidly fixed inside the ball-bearing. It is done in such a way that, the center of mass (COM) of P1 falls perfectly on the COM of the axle. Then, two thin sturdy rods of length (*d*) 60 mm are fixed vertically and symmetrically close to both the ends of the axle. These rods are used to mount two equal masses ($m_1/2$ and $m_1/2$) so as to maintain perfect weight balance on both side of the ball-bearing. The plate, P1, is then attached to two 'T' shaped side plates using screws and mounted on another rectangular aluminium base plate (P2) (Fig. 4.1). Further, two small rectangular prisms capable of moving in the horizontal plane are positioned on the outer side of the top rod of side plates. These prisms are used as a strain tuning unit (STU) (refer Fig. 4.1). At the center of base plate (P2), a hole of diameter 8 mm is machined to fix the sensor onto the tilt platform (goniometer). The photograph of the developed sensor is depicted in Fig. 4.2.

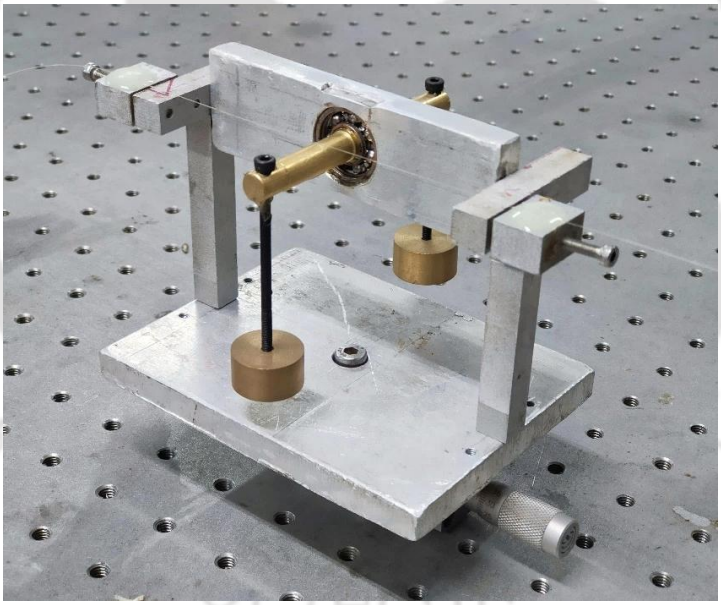

Figure 4.2: *Proposed FBG based tilt sensor*

Two FBGs, FBG1 and FBG2, written on a single optical fiber with a pre-calculated separation, are used in this sensor. Fiber is first glued on one STU. It is then wrapped in one loop over the axle and glued on the lowest part of the loop. Fiber is finally glued on the next STU, thus making two perfectly horizontal fiber arms with the FBGs at the center of each of the arms. Following this, both the FBGs were pre-strained by an equal amount using the STUs to avoid

fiber slackening. It is very crucial to mention that, during the fiber adhesion and pre-straining processes, extreme care was taken so that both the thin sturdy rod and mass system remain perfectly vertical.

Fig. 4.3 depicts the force diagram of the proposed sensor. At zero inclination of the sensor, the tensions acting in both the fiber arms are defined as, T_1 and T_2. At equilibrium, the net torque acting around center of the axle (O) will be zero. Hence,

$$\tau_c - \tau_{ac} = 0 \quad \Rightarrow rT_1 - rT_2 = 0 \tag{4.1}$$

$$\Rightarrow T_1 = T_2 \tag{4.2}$$

Here, τ_c and τ_{ac} represents the clockwise and anti-clockwise torque w.r.t. the center of axle. Upon inclination of the sensor by an angle θ in the vertical plane, the tension in both the gratings will get modified from T_1, T_2 to T_1' (= T_1 + ΔT_1) and T_2' (= T_2 + ΔT_2), respectively. At equilibrium, net torque acting around center of the axle (O) will be zero. Hence,

$$\tau_c - \tau_{ac} = 0 \tag{4.3}$$

$$\Rightarrow rT_1' - rT_2' - m_1 g d \sin\theta - m_2 g \left(\frac{d}{2}\right) \sin\theta = 0 \tag{4.4}$$

$$\Rightarrow \Delta T_1 - \Delta T_2 = mg \left(\frac{d}{r}\right) \sin\theta \tag{4.5}$$

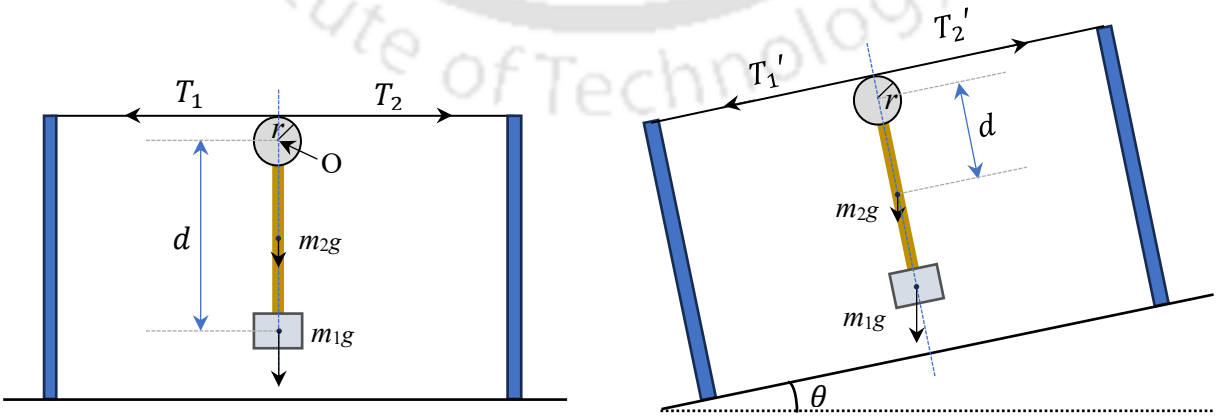

Figure 4.3: *Force diagram of the proposed sensor (a) at zero inclination (b) at θ° inclination*

Here, g is acceleration due to gravity, m_1 is the total mass attached to the vertical rods of the pendulum, m_2 is the total mass of the thin vertical rods of length d. Thus, the total mass m of the pendulum is expressed as $m = m_1 + m_2/2$. d is the length of those rods. In terms of the mechanical strains induced in both the FBG carrying arms due to tension T_1 and T_2, Eq. 4.5 can be expressed as,

$$\Rightarrow \Delta\epsilon_1 - \Delta\epsilon_2 = (\Delta T_1 - \Delta T_2)/AE \tag{4.6}$$

This changes in strain results in the shift in the Bragg wavelength of both the FBGs. Additionally, FBG is also sensitive towards ambient temperature variations due to thermal expansion and the thermo-optic effect. The shift in the Bragg wavelength (λ) resulting from strain and temperature variations for FBG written on a single-mode fiber is expressed as [39],

$$\frac{\Delta\lambda}{\lambda} = (1 - P_e)\Delta\epsilon + (\alpha + \xi)\Delta T \tag{4.7}$$

Here, P_e represents the photo-elastic coefficient of the fiber. α and ξ denote the thermal-expansion coefficient and the thermos-optic coefficient, respectively. When the pendulum is shifted from its equilibrium position, it bears a tendency towards reverting to its equilibrium position. This tendency is specifically exploited in this proposed sensor design. In the proposed sensor design, the application of tilt causes a redistribution of strain in the two FBGs, but in opposite directions. Consequently, the Bragg wavelength of one FBG experiences a redshift, while the other undergoes a blueshift. However, the Bragg wavelength shift for both the FBGs (λ_1 and λ_2) due to ambient temperature variations occurs in the same direction. Hence,

$$\frac{\Delta\lambda_1}{\lambda_1} - \frac{\Delta\lambda_2}{\lambda_2} = (1 - P_e)(\Delta\epsilon_1 - \Delta\epsilon_2) \tag{4.8}$$

Assuming, $\lambda_1 \approx \lambda_2$, $\Delta\lambda_i \ll \lambda_i$ (i = 1, 2), Eq. 4.5, Eq. 4.6 and Eq. 4.8 can be merged and written as,

$$\Delta(\lambda_1 - \lambda_2) = (1 - P_e)\frac{mg\lambda_1}{AE}\left(\frac{d}{r}\right) \cdot \sin\theta \tag{4.9}$$

As can be observed from Eq. 4.9, shift in wavelength difference $\Delta(\lambda_1 - \lambda_2)$ is directly proportional to the mounted mass (m). With the provision of adjusting the mass without compromising with the mechanical stability of the proposed sensor, the sensitivity can be tuned to the desired value simply by varying m_1. Eq. 4.9 also shows that for small tilt angle variations (up to 20°), the shift in the wavelength difference is directly proportional to θ. Apart from θ and m, sensor response depends heavily on the ratio of two crucial parameters d and r. By careful selection of these parameter, sensor response can be maximized. Furthermore, the Bragg wavelength shift of both FBGs, due to temperature variations, occurs in the same direction and by same amount. Thus, instead of absolute Bragg wavelength peak shifts of the FBGs, mapping the tilt angle to the shift in wavelength difference between the two FBGs makes the sensor inherently insensitive toward ambient temperature fluctuations.

4.2.2 Sensor Characterisation

Two FBGs, fabricated into a hydrogen-loaded single-mode fiber utilizing the phase-mask method, were employed in the sensor design. The peak reflections for the two FBGs, at strain-free condition, were observed at λ_1 = 1546.867 nm (FBG1), λ_2 = 1552.055 nm (FBG2). The fiber parameters are provided in chapter 2. The fiber containing the FBGs is securely fixed in the sensor as previously described. Following this, the fiber was pre-strained using the specially designed STUs. Then, the sensor was mounted on the tilt platform (goniometer), that had a provision to vary tilt with in ±10°. As mentioned above, sensor

response depends heavily on the ratio of *d* and *r*. Higher is the ratio of *d* and *r*, higher will be the sensitivity of the proposed sensor. Hence, by careful selection of these parameter, sensor response can be maximized. Considering the sensor design, the minimum value of *r* (radius of axle), is chosen to be 4 mm. Additionally, in order to achieve a higher ratio of *d* and *r*, the chosen value of *d* is 60 mm. This makes (*d*/*r*) to act as a multiplying factor of 15, which can enhance the sensor performance by a huge margin. Fig. 4.4 illustrates the experimental setup. The proposed FBG-based tilt sensor, mounted on a goniometer was connected to an FBG interrogator (Micron Optics, with a resolution of 0.5 pm). The interrogator was then interfaced to a computer to facilitate real-time data acquisition through Micron Optics ENLIGHT software.

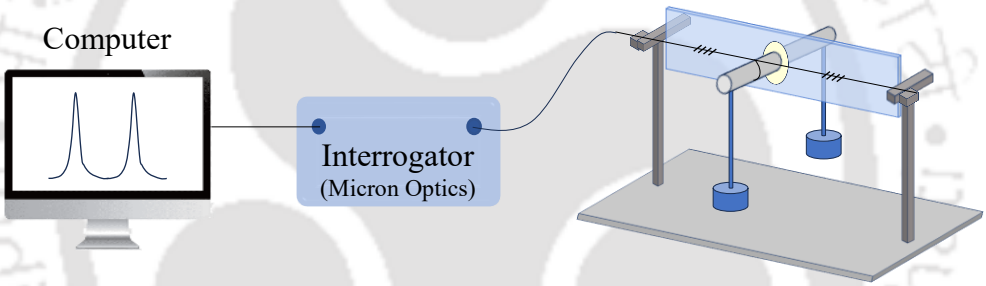

Figure 4.4: *Experimental setup for sensor characterization*

4.3 Results and Discussions

To start the experiment, first, total mass ($m_1 = 2\times m_1/2$) of 57.72 g was screwed securely into the two thin vertical rods of total mass ($m_2 = 2\times m_2/2$) 6.56 g. Hence, mass m ($= m_1 + m_2/2$) reaches a value of 61g (mass-1). Next, starting from -10° inclination in the vertical plane, the sensor was incrementally tilted to +10° (forward) and then returned back to -10° (reverse) in the smallest steps allowed by the goniometer. The wavelength shifts for both FBGs corresponding to various applied tilt angles were recorded using an interrogator (Micron Optics, Resolution: 0.5 pm). The measured response for m = mass-1 is shown in the inset of Fig. 4.5. The left vertical axis corresponds to the response of FBG2, while the right vertical

axis corresponds to that of FBG1, both plotted over time. To better understand the sensor behavior, the experimentally observed $\Delta(\lambda_1-\lambda_2)$ from the stabilized portion of the response, along with the theoretically calculated $\Delta(\lambda_1-\lambda_2)$, are plotted against different tilt angles in Fig. 4.5 for both forward and reverse tilts. The continuous line in the figure represents the theoretical response as calculated by using Eq. 4.9, whereas the different symbols represent different experimental observations. It is worth notifying that, the sensor response is identical for both the forward and reverse tilt angle variations and matches exceptionally well with the theoretical results. This is reflected by the observed theoretical and experimental sensitivities of the sensor, which is 0.2120 nm/° for both forward and reverse tilts. This identical sensitivity for both forward and reverse tilts establish the highly reversible nature of the sensor. Furthermore, the maximum discrepancy between the theoretical and the experimental responses is observed to be ±0.001 nm with the corresponding extremely low angular uncertainty of ±0.0047° for both forward and reverse tilt variations.

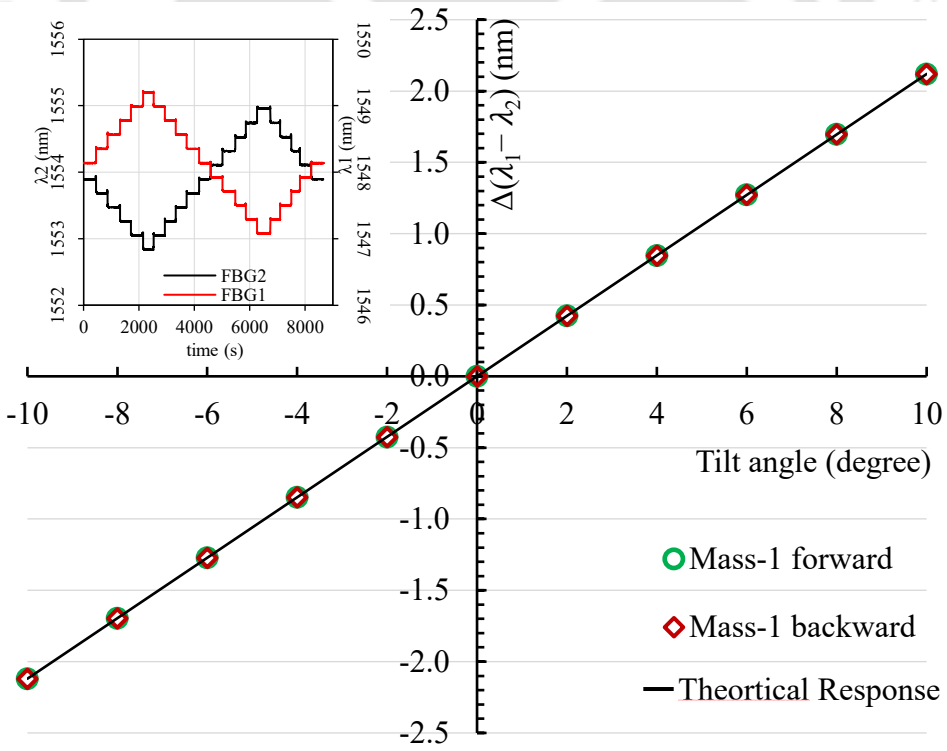

Figure 4.5: *Variation of $\Delta(\lambda_1-\lambda_2)$ for forward and backward tilt angle variations employing mass*-1

Further, to investigate the tuning capability of the sensor response characteristics, experiments were conducted with a different mounted mass (m_1) 88.76 g. Hence, the value of m in this case reaches to 92.04 g (mass-2). Then, the experiment was carried out in the similar way as described earlier. The experimental observations of $\Delta(\lambda_1\text{-}\lambda_2)$ versus tilt angle using mass-2, for both forward and reverse tilt angle variations are depicted in Fig. 4.6. The figure also illustrates the sensor response characteristics with $m = m_1$ for comparison. Again, it can be observed that, the sensor response is identical (for both the forward and reverse tilt angle variations) and matches excellently with the theoretical results. This is reflected by the observed theoretical and experimental sensitivities of the sensor, which is 0.3198 nm/° for both forward and reverse tilts. This revalidates the highly reversible nature of the sensor. In this case also, the maximum discrepancy in experimental observation compared to the theoretical results is observed to be ±0.001 nm, corresponding to a further reduced angular uncertainty of ±0.0031° (for both forward and reverse tilts). To determine the angular resolution of sensor, it is crucial to note that it is entirely dependent on the wavelength resolution interrogation system. In this experiment, wavelength resolution of the interrogator was 0.5 pm, that resulted in a tilt angle resolution of 0.0024° for the mass-1 and 0.0016° for the mass-2. Further, the accuracy of the sensor in measuring applied tilt is calculated to be ±0.0047° for the mass-1 and 0.0031° for the mass-2, for both forward and reverse tilt variations. It is also very crucial to mention that, by modifying the ratio of d and r to a higher value, the overall sensor performance can be further improved.

It is also worth noting that, the sensor response in both the cases are in excellent agreement with the theoretical response. To validate this observation further, analytical treatment using Eq. 4.9 can be employed. According to the theoretical response, the sensitivity is proportional to m. Hence, the ratio of the theoretical sensitivities for the two sets of mass is,

$$\left.\frac{S_{mass-2}}{S_{mass-1}}\right|_{theo} = \frac{92.08}{61} = 1.51 \tag{4.10}$$

The ratio of the experimentally obtained sensitivities for the two sets of mass is,

$$\left.\frac{S_{mass-2}}{S_{mass-1}}\right|_{exp} = \frac{0.3198}{0.2120} = 1.51 \tag{4.11}$$

Eq. (4.10) and (4.11) establishes the fact that the response of the proposed sensor is in excellent agreement with the anticipated theoretical responses. Moreover, this validates the potential to customize the sensitivity of the proposed sensor for specific applications by carefully varying the mounted mass.

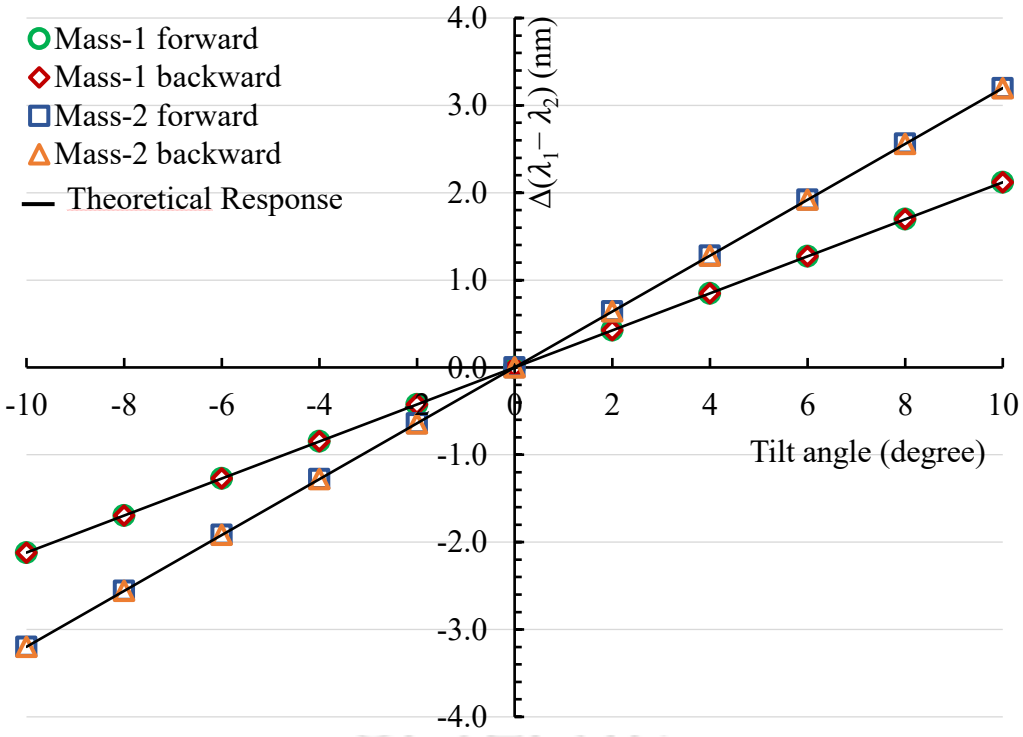

Figure 4.6: *Variation of* $\Delta(\lambda_1 - \lambda_2)$ *for forward and backward tilt angle variations employing mass-2 and mass-1*

Next, the performance characteristics of the proposed sensor is compared with other FBG based tilt sensors. In Table-4.1, all the important parameters (i.e. sensitivity, angular resolution, measurement accuracy, maximum discrepancy) required for the analysis of effective sensing capabilities, are listed. It is worth noticing from the table that the proposed

sensor is characterized with the lowest maximum discrepancy of ±0.001 nm with respect to the theoretical response. However, in case of most of the reported sensors tabulated above, the maximum discrepancy (compared to their experimentally fitted data) is much higher. The table also mentions the values of the mass (m) used in those sensors and the dependency of sensitivity on m. It is worth noticing from the table that, the proposed sensor is characterized with the highest tilt angle measurement accuracy and highest angular resolution. The sensor is also characterized with the highest sensitivity among all the reported tilt sensors. Furthermore, as depicted by Eq. 4.9, the sensitivity varies in a linear proportion to m, whereas all the other listed sensors' sensitivities vary in linear proportion to either $m/2$, m, $2m$ or $8m$.

Table 4.1: Comparison of performance characteristics of the proposed sensor

Author	Sensor dependency on mass of bob	Mass of bob (g)	Sensitivity (nm/°)	Accuracy	Maximum discrepancy (nm)	Angular resolution
Guan *et al.* [74]	m	344	0.0752	± 0.100°	±0.008	0.0070°
Au *et al.* [64]	m	528	0.0540	± 0.270°	±0.002	0.0190°
Bao *et al.* [75]	m	528	0.0540	± 0.270°	–	0.0190°
Bao *et al.* [76]	$8m$	500	0.0960	± 0.200°	–	0.0130°
Yang *et al.* [77]	m	500	0.0740	± 0.180°	–	0.0135°
Ni *et al.* [79]	m	100	0.0537	–	±0.015	0.0090°
Chen *et al.* [80]	m	357	0.0600	± 0.167°	±0.010	0.0067°
Li *et al.* [81]	m	5.3	0.0011	–	–	–
Aneesh *et al.* [82]	m	110	0.0626	± 0.360°	±0.023	0.0080°
Pathi *et al.* [83]	$m/2$	90	0.0120	± 0.050°	±0.001	0.0041°
This work	m	92.04	0.3198	± 0.0031°	±0.001	0.0016°

The sensors reported in [64], [74], [75], [77], [79], [80]-[82] have sensitivity dependency on the mass in a proportion to *m*. The maximum sensitivity among these sensors was proposed by Guan et al [74]. Combining equivalency of sensitivity dependency on being linearly proportional to *m* and the value of *m* being ~3.74 times larger, the expected sensitivity of the reported sensor would be ~1.1953 nm/° (15.89 times higher). The sensor reported in [83] has sensitivity dependency on the mass, in a proportion to *m*/2. Combining equivalency of sensitivity dependency on being linearly proportional to *m*/2 and the value of *m* being ~0.98 times larger, the expected sensitivity of the reported sensor would be ~0.1567 nm/° (13.06 times higher). Similarly, the sensor reported in [76] has sensitivity dependency on the mass, in a proportion to 8*m*. Combining equivalency of sensitivity dependency on being linearly proportional to 8*m* and the value of *m* being ~5.43 times larger, the expected sensitivity of the reported sensor would be ~13.8983 nm/° (~144.77 times higher). All these equivalent sensitivities are much higher than that of the reported works. It is also important to acknowledge that, when the mass of the mounted weight is increased, the accuracy and resolution of the sensor improves substantially.

Further, it is very crucial to eliminate the effect of ambient temperature variations on the proposed sensor for ensuring accurate performance in real-field applications. Although, the sensor is designed to meet this requirement by mapping the tilt angle variation into the shift in wavelength difference between the FBGs, it is important to verify the effect of temperature variations on the sensor performance, experimentally. For this, a water bath test was conducted. First the sensor, carrying mass-2 and inclined at a fixed angle, was fixed inside a water tank. Following this, water of ~60°C was poured inside the tank to the level ensuring that the sensor is completely immersed throughout the experiment. Then the water was left to cool down naturally to room temperature (~25°C) and the corresponding shift in wavelength difference

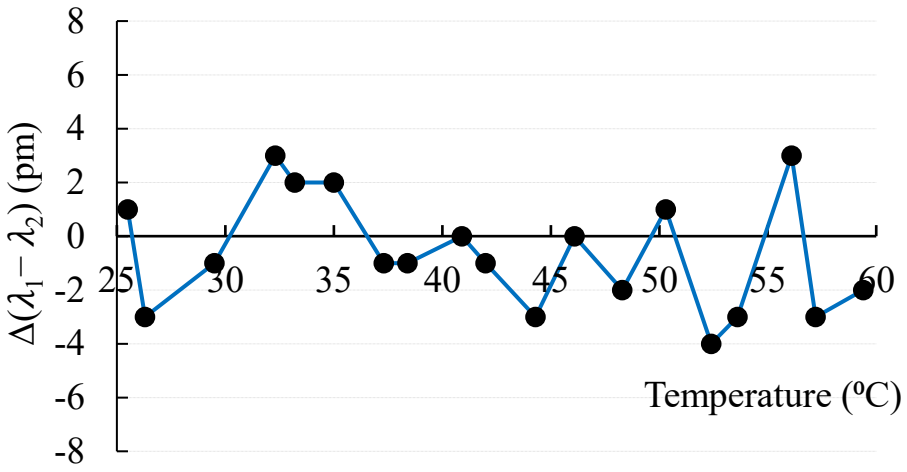

Figure 4.7: *Thermal response of the tilt sensor with mass-2 at a fixed inclination*

was measured. Fig. 4.7 depicts the thermal response of the sensor. The maximum discrepancy observed was within ±3 pm, which is about 123 times less than the shift observed by an uncompensated FBG under the same temperature variation. This result ensures temperature-independent tilt measurement.

Further, Repeatability and reliability are other critical parameters for further evaluation of the sensor performance. To examine this, experiments were conducted over three separate days with two-day intervals. The experimental results are depicted in Fig. 4.8, where

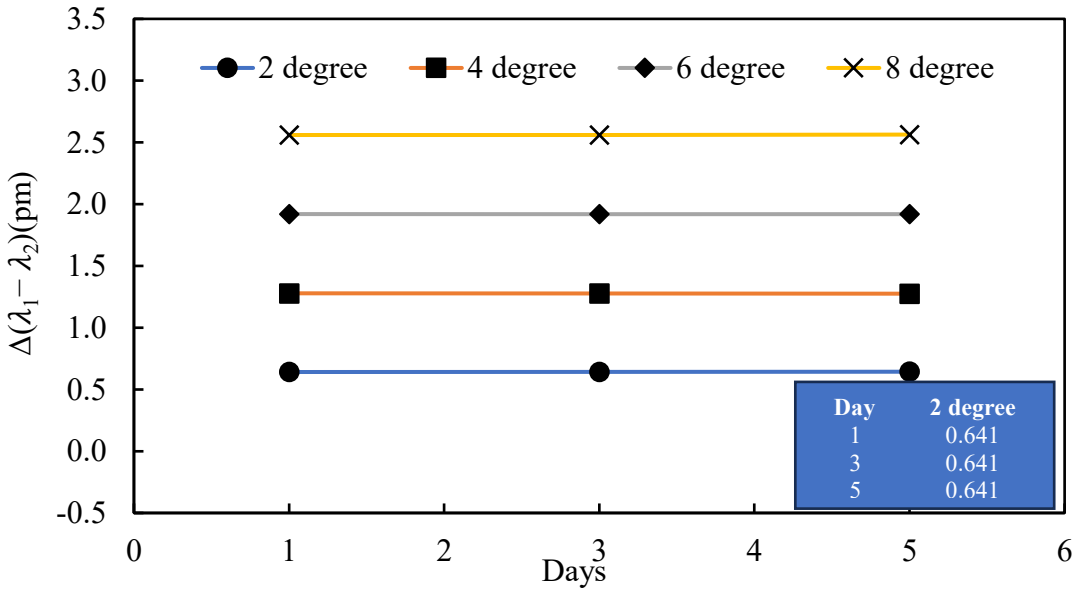

Figure 4.8: *Repeatability and reliability test*

$\Delta(\lambda_1 - \lambda_2)$ for four different tilt angles (2°, 4°, 6°, 8°) are plotted. The inset shows the corresponding date for 2°. The maximum variation in the sensor output, compared to first day across all inclinations, was observed to be on the order of 10^{-3} nm. This minimal variation and consistent performance over multiple days indicates that the sensor demonstrates excellent reliability and repeatability, making it highly dependable for precise measurements. This ability to maintain reliability over repeated trials and time periods is essential for practical applications, and the observed results confirm the sensor's suitability for such requirements. Moreover, the sensor demonstrates effective sensing capabilities with excellent accuracy, very high angular resolution, tremendously high sensitivity, and a highly reversible response. These attributes make the reported sensor of significant practical importance, offering reliable performance in environments with varying temperatures, thus broadening its applicability in real-field applications.

4.4 Conclusion

This chapter reports a novel design strategy for the development of an FBG-based all optical tilt sensor. The research includes both rigorous theoretical analysis and experimental investigation to establish the response characteristics of the sensor across the dynamic range of ±10°. Experimental observation demonstrates a tremendously high sensitivity of 0.3198 nm/°, that capable of being tuned further to any desired value. Further, the sensor is characterized with an excellent accuracy (±0.0031°), very low maximum deviation (±0.001 nm), and an outstanding angular resolution of 0.0016°. The sensing principle depends on mapping the tilt angle into wavelength shift difference between the two FBGs. This makes the sensor inherently immune to ambient temperature fluctuations, making it suitable for practical industrial and engineering applications. Furthermore, the experimental observations establish the sensor response to have a very high degree of reversibility, repeatability, and reliability. The sensor

design exhibited excellent response characteristics in comparison to both the sensors developed and reported in chapter 2 and chapter 3 along with all the sensors reported in literature. In the sensor designs reported in last three chapters, the strain induced Bragg wavelength shift mechanism of FBG is exploited. The next chapter focuses on proposing novel sensor designs for tilt monitoring utilizing the effective RI sensitivity of an EFBG in order to achieve intensity modulation of the FBG spectrum.

Chapter 5 : Etched Fiber Bragg Grating Based Novel Tilt Sensor Employing Effective RI Induced Intensity Modulation Mechanism

5.1 Introduction

As discussed earlier, n_{eff} can be modulated only by applying strain or temperature perturbations, exploiting the strain-optic and thermo-optic effects. It remains unaffected by variations in the surrounding RI. Consequently, FBGs are naturally sensitive towards strain and temperature changes due to modulations in both n_{eff} and Λ, while being insensitive towards ambient RI [84]. However, if the cladding diameter in the region carrying FBG is reduced enough, the effective RI of the propagating mode gets modulated in accordance with the RI of the surrounding medium. This happens due to the interaction of the evanescent tail of the fundamental guided mode to interact more strongly with the surrounding medium. This makes FBG with thinned cladding to be not only sensitive towards strain and temperature, but also sensitive towards the ambient RI.

In this chapter, instead of traditional wavelength modulation mechanism, intensity modulation of the FBG spectrum that exploits the effective RI sensitivity of EFBG is used to develop novel all optical tilt sensor. This technique is utilized for the first time for the development of tilt sensor, to the best of author's knowledge. The design strategy of the proposed sensor employs four EFBGs in vertical configuration. All the four EFBGs are initially immersed upto the half-length into a strategically chosen liquid. Response characteristics of the proposed sensor against tilt angle variations are theoretically investigated. EFBG splits into two distinct gratings when partially immersed in a liquid. Applied tilt modulates the length of EFBG immersed into a liquid; which in turn, modulates the characteristic reflection spectrum of both the sections (exposed to liquid and to the air). In order to capture applied tilt with better

sensitivity and improve sensor performance, another sensor is proposed that exploits the same sensing mechanism (intensity modulation of EFBG). The design strategy of the proposed sensor is based on four EFBGs, each inclined in the vertical plane while making a cross. The sensor characteristics of the new sensor design was also investigated theoretically. Furthermore, both the sensors are observed to be capable of measuring the magnitude and the direction of inclination relative to the horizontal plane across the designated dynamic range of -10° to 10°, exhibiting excellent reversibility and reliability. Additionally, as peak reflectivity of FBG spectra does not depend on the temperature variations, change in temperature will cause the centre wavelength of the FBGs to get shifted. But, the reflected peak, which is used to monitor the applied tilt in our work, remains unaffected by temperature fluctuations. Thus, the problem of temperature cross-sensitivity gets eliminated inherently.

5.2 Theoretical model

Bragg condition manifests the condition for achieving strong coupling between identical or nearly identical forward and counter-propagating modes in a fiber grating inscribed within a single-mode fiber (SMF). In terms of grating parameters n_{eff} (effective RI of fiber for the guided mode) and Λ (spatial period of the grating), Bragg wavelength is expressed as, $\lambda_B = 2\Lambda n_{eff}$ [39]. Bragg wavelength (λ_B) is inherently immune to changes in the RI of the surrounding medium. However, if the diameter of the fiber in the cladding region of the FBG is reduced to a certain extent, the evanescent tail of the fundamental guided mode of the fiber interacts strongly with the surrounding medium. Hence, n_{eff} gets modulated as a result of changes in the surrounding RI. Consequently, the Bragg wavelength (λ_B) also becomes dependent on surrounding RI

modulations. The peak reflectivity (R), which is determined by the coupling coefficient (κ) and the length of the FBG (L), is expressed [112],

$$R = \tanh^2[\kappa L] \tag{5.1}$$

If an EFBG is partially immersed in a liquid (remaining part exposed to air), the original single reflected peak splits into two distinct reflected peaks. Hence, it can be regarded as two different gratings with two distinct Bragg wavelengths as discussed below. This occurs because the reflected spectrum is influenced by the portion of the EFBG that is submerged into the liquid. Therefore, the reflected spectrum will contain two peaks; one centered at the coupling wavelength of the core mode influenced by the air interface, and the other centered at the coupling wavelength of the core mode influenced by the liquid. Consider an EFBG of length L. If a section of length l_L of this EFBG is immersed into a liquid and section of length l_A (L - l_L) is exposed to air, the peak reflectivities for the portion of EFBG exposed to air (R_A) and exposed to the liquid (R_L) can be expressed as,

$$R_L = \tanh^2[\kappa_L l_L] \tag{5.2}$$

$$R_A = \tanh^2[\kappa_A l_A] \tag{5.3}$$

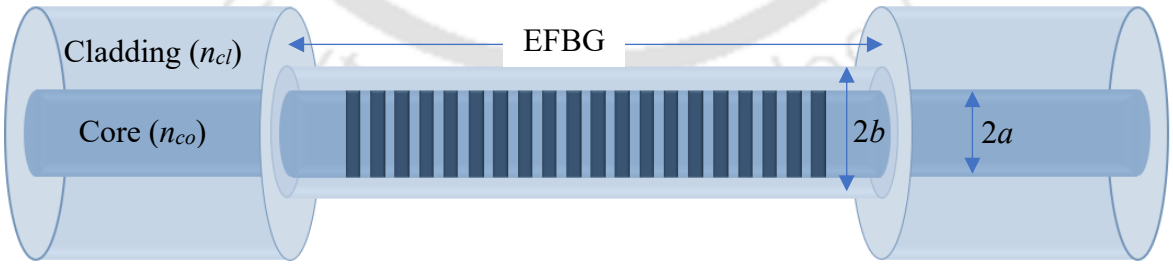

Figure 5.1: *Schematic diagram of EFBG*

In order to understand the behaviour of an EFBG, partially submerged into a liquid, and to design the sensor, it is important to study the effect of n_{out} and the cladding diameter (b) on the

FBG's characteristics. The well-known doubly-cladded model is deemed most appropriate in this scenario, for establishing a distinct correlation between the modal propagation constant (β) and the RI of the surrounding medium (n_{out}) [51]. After determining β for a given n_{out}, λ_B can be easily computed using the formula $\lambda_B = 2\Lambda n_{eff} = 2\Lambda(\beta/k_o)$, where k_o denotes the free space wavenumber. The fiber structure utilizing the doubly-clad fiber model for EFBG is shown in Fig. 5.1. The radii of the core and inner-cladding are represented by a and b, respectively.

The refractive indices of the core, inner-cladding, and surrounding medium (outer cladding) are denoted by n_{co}, n_{cl}, n_{out} respectively. For azimuthal order m, the radial dependence $\psi(r)$ of the axial field components are expressed as [113],

$$\begin{aligned} \psi &= A_0' J_m\left(u\frac{r}{a}\right) && \text{For } r \le a \\ \psi &= A_1' I_m\left(v'\frac{r}{b}\right) + A_2' K_m\left(v'\frac{r}{a}\right) && \text{For } a \le r \le b \text{ if } \beta > k_0 n_2 \\ \psi &= A_3' K_m\left(v\frac{r}{a}\right) && \text{For } r \ge b \end{aligned} \tag{5.4}$$

Here, $u = a(k_o^2 n_{co}^2 - \beta^2)^{1/2}$, $v = b(\beta^2 - k_o^2 n_{out}^2)^{1/2}$, and $v' = b(\beta^2 - k_o^2 n_{cl}^2)^{1/2}$. A's are the normalization coefficient. J_m is ordinary Bessel function, whereas, I_m and K_m are the modified Bessel functions. Under the weekly-guiding approximation, the continuity of the transverse field components across the two interfaces (between core and inner cladding, and between inner and outer cladding) results in a set of four equations,

$$\begin{aligned} &A_0' J_m(u) - A_1' I_m(v'c) - A_2' K_m'(v'c) = 0 \\ &uA_0' J_m(u) - v'cA_1' I_m'(v'c) - v'cA_2' K_m'(v'c) = 0 \\ &A_1' I_m(v') + A_2' K_m(v') - A_3' K_m'(v') = 0 \\ &v'A_1' I_m'(v') + v'A_2' K_m'(v') - vA_3' K_m'(v') = 0 \end{aligned} \tag{5.5}$$

Here $Z' = dZ/dr$ (Z is a Bessel function J_m, I_m and K_m) and $c = b/a$. In order to obtain a non-trivial solution, the determinant of the 4×4 coefficient matrix of these equations must be

equated to zero, thereby leading to the dispersion equation that defines the guided mode of the doubly-clad fiber. For the fundamental mode (LP_{01}) the dispersion equation becomes,

$$\frac{v'cK_1(v'c)J_0(u) - uJ_1(u)K_0(v'c)}{v'cI(v'c)J_0(u) + uJ_1(u)I_0(v'c)} = \frac{v'cK_1(v')K_0(v) - vK_1(v)K_0(v')}{v'I_1(v')K(u) + vK_1(v)I_0(v')} \tag{5.6}$$

For a fixed value of b, this equation is numerically solved using MATLAB software. In the theoretical investigations, cladding radius in the FBG region (b) is varied from $62.5\mu m$ (unetched fiber) to the reduced values of $9.5\mu m$, $7.5\mu m$ and $6\mu m$. Fiber parameters used for solving this equation are that of SMF-28e (a = 4.15μm, n_{co} = 1.460 and n_{cl} = 1.4564). Findings of the numerical simulations are illustrated in Fig. 5.2, which displays the simulated response of FBG (λ_B vs n_{out}) for a fixed value of b. It is evident from Fig. 5.2 that the normal (unetched) FBG (b = 62.5μm) is not at all sensitive towards the changes in the surrounding RI. Etching the fiber in FBG region makes FBG sensitive to the ambient refractive

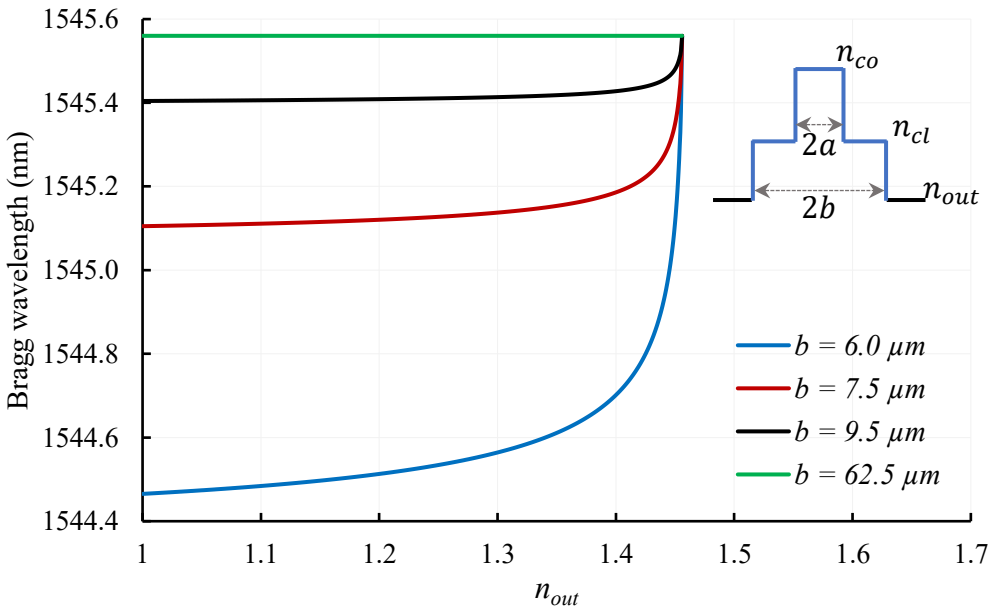

Figure 5.2: *Bragg wavelength of an EFBG vs* n_{out} *for different cladding radii (b). The inset shows the RI variation along the cross-section of doubly cladded and weakly guided fiber.*

indices. The lower the cladding diameter, the higher is the sensitivity of an EFBG towards the ambient RI variations. Specially, if the EFBG is exposed to an ambient medium with n_{out} > 1.4,

effective index modulation would be very prominent. Therefore, if an FBG is etched appreciably and then exposed partially (up to a length l_L) to n_{out} ~1.456 and (for the remaining length l_A) to n_{out} = 1 (air), one FBG will effectively split into two FBGs with two distinct resolvable peaks. Variation of l_L plays a major role in defining the optical characteristics of the two sections of a single FBG. Proposed sensors exploit the variation of optical characteristics of the two sections of a single FBG by modulating l_L.

5.3 First design strategy

For the design and development of the first sensor design strategy, a unique mechanism is devised in order to map applied tilt angle (θ) onto l_L. In the proposed sensor, varying tilt angle θ modulates the section-length l_L immersed in the liquid. This results in the characteristic changes in R_A and R_L both. Thus, by monitoring R_A and R_L while changing the inclination of the sensor from the horizontal, tilt angle variations can be measured.

5.3.1 Sensor design and principle

For the sensor, a cubical Perspex box (having four vertical walls and a base plate) is designed. The inner dimension of this box is taken as 10cm (length) ×10cm (breadth) ×6cm (height). Four identical etching chambers are the part of the sensor design. These are to be used for reducing the cladding diameter in the FBG region. Each etching chamber design carries a Perspex rectangular base plate and a Perspex rectangular top plate of width 1cm, rigidly attached to each other. Both the rectangular plates are of identical dimensions (3cm×4cm). An oval shaped section of length 15mm is hollowed out from the center of the top plate in the proposed design. Identical oval shaped section of width 5mm is removed from the central region of the base plate (Fig. 5.3(a)). Four FBGs (λ_{B1} = 1544.56 nm, λ_{B2} = 1536.75 nm, λ_{B3} = 1545.00 nm, λ_{B4} = 1550.7 nm), each of length 14 mm, are used in designing the sensor. Each FBG is fixed within these chambers in such a way that FBG remains at the center of the oval

section. Fiber carrying FBG is strained by a pre-calculated amount. Precisely controlled chemical etching process using 40% HF (Hydrofluoric) acid solution for 48 minutes followed by 15% HF acid for 15 minutes (in room temperature) reduces the diameter of the fiber uniformly in the FBG region to the desired value. In this study, the diameter of the fiber in the etched region was analysed using a Field emission scanning electron microscope (Sigma FESEM, Carl Zeiss NTS, USA, resolution 2.5nm), and a uniform fiber diameter with a reduced value of approximately 12.07µm was observed for the etched section of the fiber. Etching chambers carrying the EFBG are fixed at the center of the inner side of each vertical plate (Fig. 5.3(b)). In this arrangement, FBGs remain vertical and the middle points of the four FBGs remain in the horizontal plane that passes through the center of the cubical Perspex box. Cubical Perspex box carries a strategically chosen liquid (RI ~1.45) up to a vertical height of 3cm, thus ensuring half-length of the EFBGs is immersed into the liquid (Fig. 5.3(b)).

In order to understand the sensing mechanism, especially when the sensor is to be tilted in *y-z* plane, the side view of the proposed sensor is depicted in Fig. 5.4(a). Let us consider the case when anticlockwise tilt is applied in *y-z* plane. In this case, EFBG near the rightside wall (confined in *x-z* plane) will keep getting exposed to the air (shown by *h* in Fig. 5.4(b)), while the FBG near the left side wall (confined in *x-z* plane) will dip further into the liquid (by

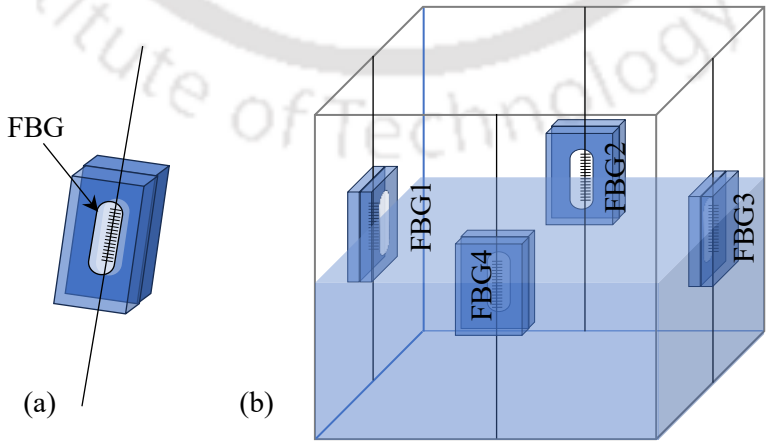

Figure 5.3: *(a) Etching chamber with FBG (b) Schematic diagram of the sensor.*

the same amount h in Fig. 5.4(b)). However, the EFBGs in the orthogonal plane (y-z plane), shown in the middle of the box in Fig. 5.4(b), will not face any change in the height of the liquid level, even when the sensor is tilted; hence, will have no effective role in this case. On the other hand, when the sensor is tilted in x-z plane, FBGs fixed near the side walls confined in y-z plane will play an effective role in the sensing process, and FBGs that are fixed to the other two side walls (confined in x-z plane) will be having no effective role. Thus, it is the section-length of FBG exposed to air, and to the liquid, that gets modulated by the applied tilt angle (θ) variations. Hence, it is crucial to establish a relation between the applied tilt (θ) and the corresponding variations in the length of FBG that gets immersed into the liquid or exposed to air (h). Multiple observations show that the variation in h, when the liquid filled cubical box is tilted by an angle θ, is given by,

$$h = 0.01742\, x\, \theta \tag{5.7}$$

Where x is the distance of the FBG carrying fibers from the center of the cubical box (Fig. 5.4(b)). Eq. (5.7) establishes that the length of the FBG exposed to air/immersed in the liquid, i.e., h is directly proportional to the applied tilt angle θ. Variation of h while changing the tilt angle modifies the peak reflectivity (R) of the FBG.

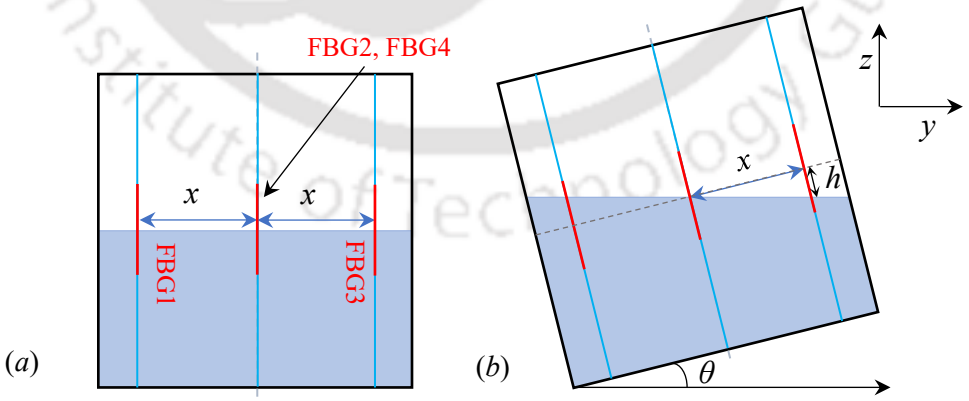

Figure 5.4: *(a) Schematic diagram of the sensor at zero inclination ($\theta = 0^o$), (b) Schematic diagram of the sensor at θ^o.*

5.3.2 Result and discussion

Proposed sensor utilizes four EFBGs, which are confined in the vertical plane, are equidistant from each other and fixed in a cubical box. Each EFBG of length L (= $2l$) is partially immersed into a strategically chosen liquid, which occupies half of the volume of the box. At zero inclination (θ = 0°), lower half of the EFBG (of length $l_L = l$) is immersed into the liquid, while the upper half (of length $l_A = l$) is exposed to air. When the sensor is tilted to an angle θ, peak reflectivity of the section of EFBG exposed to air (R_A) and peak reflectivity of the other section of EFBG exposed to the liquid (R_L) can be expressed as,

$$R_A = \tanh^2[\kappa_A(l + h)] = \tanh^2[\kappa_A(l + 0.01742\, x\theta)] \tag{5.8}$$

$$R_L = \tanh^2[\kappa_L(l - h)] = \tanh^2[\kappa_L(l - 0.01742\, x\theta)] \tag{5.9}$$

Where Eqs. (5.2), (5.3) and (5.7) are employed. As can be observed from Eq. 5.8 and Eq. 5.9, peak reflectivities R_A and R_L depend on the two additional parameters, x and θ. Theoretically simulated response of the EFBG (FBG1), partially dipped into the liquid, is depicted in Fig. 5.5 for inclination angle θ = 0°.

As can be observed, in absence of any inclination (θ = 0°), peak reflectivity for both the parts of FBG are equal. Afterwards, inclination angle is varied in y-z plane using a step size

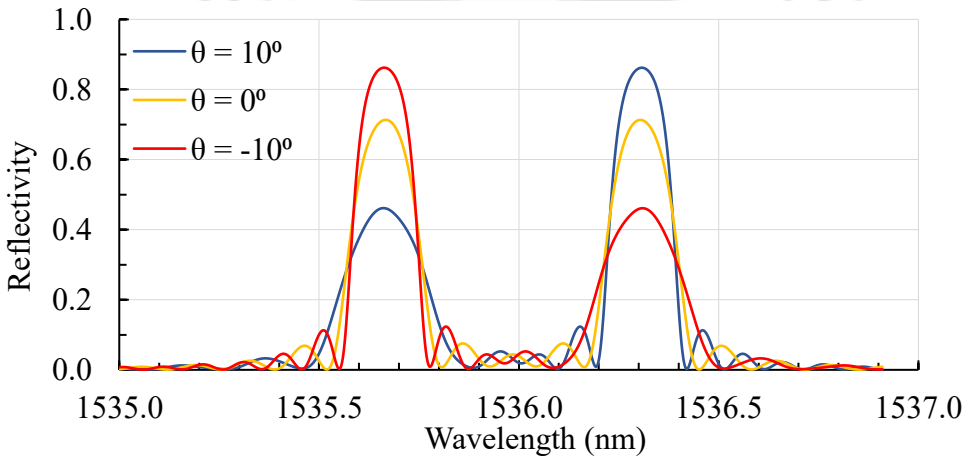

Figure 5.5: *Variation in peak reflectivity of FBG1 for θ = -10°, 0°, +10°.*

of 1°. As an example, Fig. 5.5 also illustrates the theoretical response of EFBG (FBG1) when the sensor is tilted by extreme amounts (θ = +10° and θ = -10°). As can be observed from the simulated results, peak reflectivity for both the parts of the FBG gets modified in accordance to the applied tilt. In order to get a deeper insight of the response of the proposed sensor, peak reflectivities for both the sections of the EFBG, i.e., R_L and R_A, are calculated from the spectrum depicted in Fig. 5.5. This is done for the applied tilt angles in the range of ±10°.

Afterwards, these reflectivities are plotted in logarithmic scale (log[1-R]) against the tilt angles. Fig. 5.6 depicts the plot of log[1-R_L] against the tilt angles for a fixed value of x (32mm). As can be observed, peak reflectivity of the section of EFBG that remains immersed in the liquid increases with the applied tilt, which is expected as l_L increases for FBG1. Response remains linear (on the logarithmic scale) over the dynamic range of ±10°. Fig. 5.7 depicts the plot of log[1-R_A] against the tilt angles for the same value of x (32mm). As expected, peak reflectivity of this section of EFBG that remains exposed to the air decreases with the applied tilt. Response remains linear (on the logarithmic scale) over the dynamic range of ±10°. An identical (absolute) sensitivity of 0.97 dB/° with a linearity of 0.999 is observed when x is kept 32mm. Fig. 5.6 and Fig. 5.7 also depict the sensor response when x is increased and kept fixed at 40 mm. As can be observed, changing the value of x by 8 mm, sensitivity increases by 23.7% and becomes 1.20 dB/°. Importantly, when the sensor is tilted in the clockwise direction, EFBG1 (in Fig. 5.3(b)) will get revealed to air, i.e., l_L will decrease and h will increase for this grating. Hence, the spectrum will be reversed. This characteristic feature of the proposed sensor enables it to monitor not only the magnitude but also the direction of the applied tilt. By critically choosing a liquid with low viscosity, high degree of reversibility and repeatability is expected to be observed. Furthermore, peak reflectivity (R) does not depend on the temperature variations. Change of temperature will cause the center wavelength of the FBGs to get shifted. The reflected peak, which is used to monitor the applied tilt in our work, remains unaffected

by temperature fluctuations. Thus, the problem of temperature cross-sensitivity gets eliminated inherently. This makes the sensor inherently temperature independent.

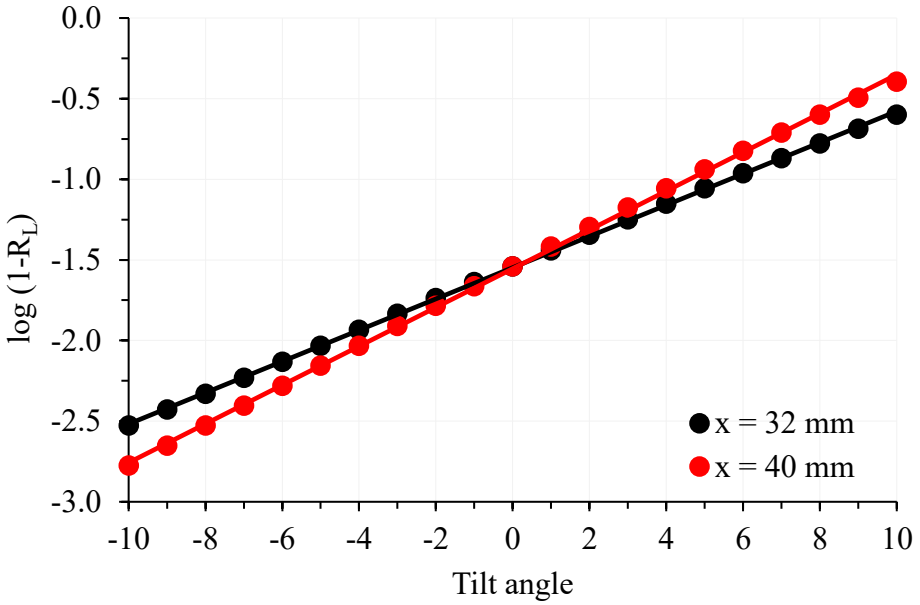

Figure 5.6: *Variation of reflectivities with tilt angle for EFBG partially dipped in liquid.*

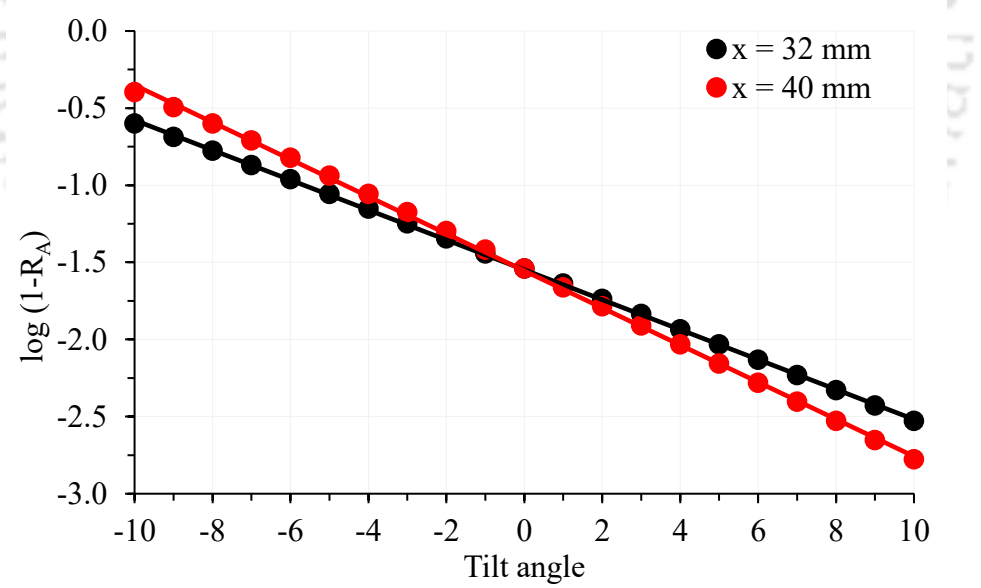

Figure 5.7: *Variation of reflectivities with tilt angle for EFBG partially exposed to air.*

The proposed sensor is capable of sensing tilt angle variations with reasonably good sensitivity. However, in order to further enhance the sensitivity, another novel sensor design strategy that exploits the same sensing mechanism, is proposed and the response characteristics is analysed theoretically.

5.4 Second design strategy

In this case, proposed sensor exploits the variation of optical characteristics of one of the two sections of single EFBG by modulating l_A. To achieve this, a novel mechanism is devised in order to map applied tilt angle (θ) onto l_A. In the proposed sensor, varying tilt angle θ modulates the section-length exposed to air. This results in the characteristic changes in R_A. Hence, by monitoring R_A while changing the inclination of the sensor from the horizontal, tilt angle variations can be monitored.

5.4.1 Sensor design and principle

For the sensor, a cubical Perspex box of outer dimension 6cm (length) × 6cm (breadth) × 6cm (height) was machined. Fiber carrying four FBGs (λ_{B1} = 1538.75 nm, λ_{B2} = 1545.56 nm, λ_{B3} = 1547.25 nm, λ_{B4} = 1551.12 nm, each of length 18 mm) was used in the sensor. Design strategy of the proposed sensor, illustrated in Fig. 5.8, employs four inclined fiber arms, each carrying single FBG. To realize the sensor, fiber carrying FBGs was first inserted into the box through the hole at A in the left wall (W1). It was then taken out from the box through the hole at B in the opposite (right) wall (W2), thus making the fiber arm AB inclined at -ϕ from the horizontal. Following this, fiber was again inserted into the box through the hole at C in the wall W2, and then taken out from the box through the hole at D in the wall W1; thus, making the other fiber arm CD inclined at +ϕ from the horizontal. In the similar way, other two fiber arms (EF and GH) were realized using the holes machined in the remaining two side walls (W3 & W4) (Fig. 5.8(b)). Holes in the opposite walls were strategically planned to ensure that each fiber arm, inclined at ±ϕ, remained (a) confined in the vertical plan, (b) closed to the central section of the box (Fig. 5.8). FBGs were positioned at the upper end of each fiber arm. One end (upper) of each fiber arm was glued onto the strategically designed strain tuning units (STUs), fixed just outside the walls (Fig. 5.8(a)); whereas the other end (lower) was glued into the hole at B,

D, F and H. STUs were used to pre-strain the fiber arms to avoid fiber slackening. All the four FBGs were simultaneously etched within the Perspex box. For this, Perspex box was inverted, and HF (Hydrofluoric) acid was filled up to the height that ensured only the FBG carrying length of the fiber got exposed to the acid. Precisely controlled chemical etching process reduces the diameter of the fiber uniformly in the FBG region to a desired value. In this study, fiber diameter uniformly reduced to 12.07μm in the FBG region is used. Afterwards, HF acid was removed. Perspex box was cleaned; and then filled with a strategically chosen liquid (RI ~1.456) up to the horizontal level AEGC, ensuring the upper edge of each fiber arm (and hence, each EFBG) got just immersed into the liquid (Fig. 5.8(a)).

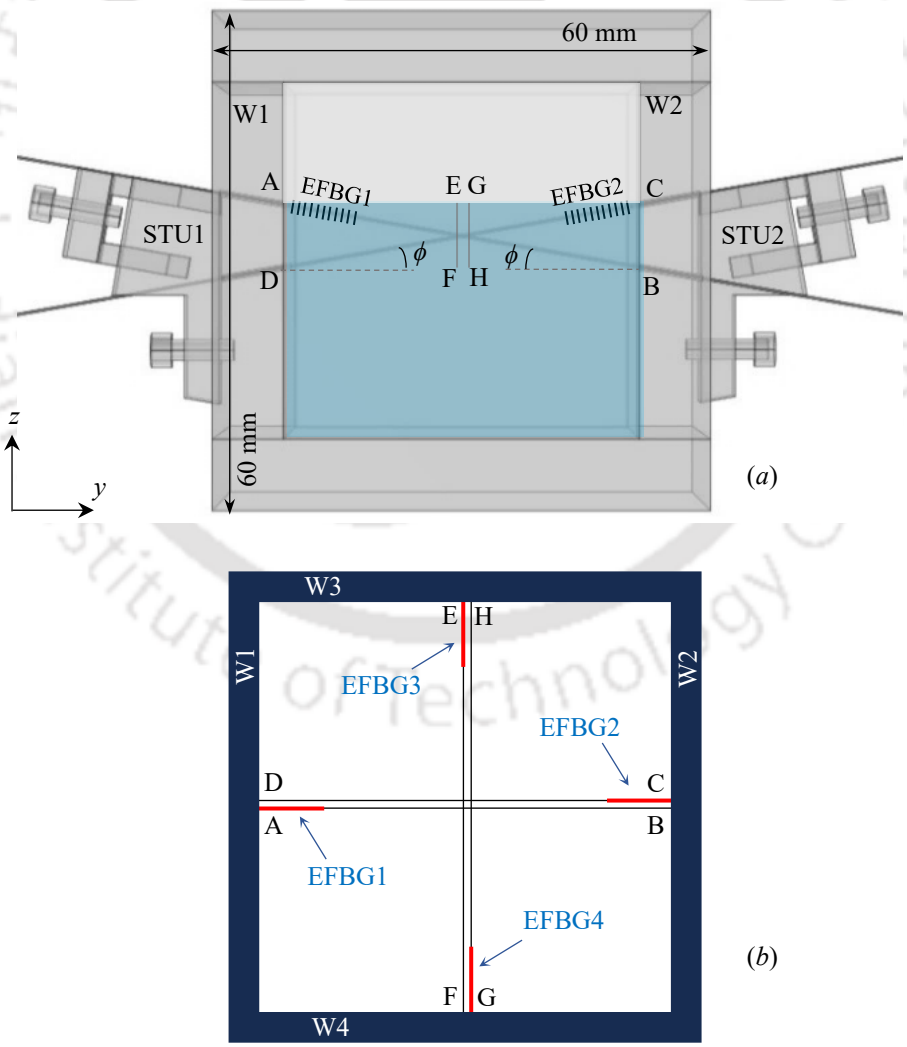

Figure 5.8: *Schematic diagram of the proposed sensor: (a) Side view (b) Top view of the sensor.*

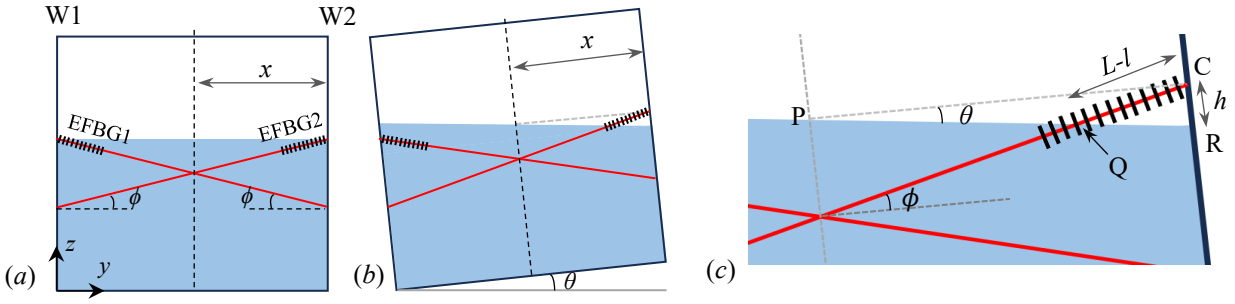

Figure 5.9: *(a) Schematic diagram of the sensor at 0°, (b) Schematic diagram of the sensor at θ°, (c) Enlarged picture of sensor at θ° inclination.*

In order to understand the sensing mechanism, as an example, when the sensor is tilted in the *y-z* plane, schematic diagram depicted in Fig. 5.9 is useful. In the absence of any given tilt, EFBGs are completely immersed into the liquid (Fig. 5.9(a)). Considering the case when anticlockwise tilt is applied in this plane, EFBG2 near the wall W2 will keep getting exposed to air (shown by l_A = QC, in Fig. 5.9(c)), whereas EFBG1 near the wall W1 will remain completely immersed into the liquid. Hence, EFBG1 will have no effective role in this case. Similarly, when clockwise tilt is applied in this plane, EFBG1 will keep getting exposed to air, while EFBG2 will remain completely immersed into the liquid. Hence, EFBG2 will have no effective role in that case. Needless to mention that, while tilting the sensor in *y-z* plane, EFBG3 and EFBG4 in orthogonal fiber arms (EF and GH) will not face any exposure to air; hence, will have no effective role in this scenario. However, in the case when inclinations are applied in the orthogonal *x-z* plane, EFBG3 and EFBG4 will play effective role depending on the direction of the applied tilt, whereas, EFBG1 and EFBG2 will remain ineffective. In all the cases, it is the section-length of EFBG exposed to air that gets modulated by varying the applied tilt (θ). Therefore, it is essential to establish a relationship between the applied tilt and the corresponding variations in the length of the EFBG exposed to air (l_A). Considering, as an example, the case when the sensor is tilted by an angle θ in the anticlockwise direction in *y-z* plane, length of EFBG that gets exposed to air is given by (Fig. 5.9(c)),

$$l_A = [\cos\theta / \sin(\theta + \phi)]h \tag{5.10}$$

where h (= CR) is the variation of liquid level at the wall W2 (Fig. 5.9(c)). Multiple observations establish that h is related to θ as,

$$h = 0.01742\, x\theta \tag{5.11}$$

where x (= PC) is the half-width of the cube. Consequently, Eq. (4) can be rewritten as,

$$l_A = [\cos\theta \,/\, \sin(\theta + \phi)] \times 0.01742\, x\theta \tag{5.12}$$

Eq. 5.12 establishes that the length of EFBG getting exposed to air (l_A) not only depends on the applied tilt angle θ, but also depends on ϕ (angle made by fiber with the horizontal at θ = 0°) and x (half-width of the cube). Thus, for the fixed dimension "x" of the sensor, the additional parameter ϕ plays a crucial role in dictating the length (l_A) that gets revealed to air; which in turn, modulates the peak reflectivity (R_A) of the EFBG section that is exposed to air.

5.4.2 Result and discussion

Proposed sensor utilizes four EFBGs that are fixed at an angle $\pm\phi$ from the horizontal. Vertical planes carrying two EFBGs (λ_{B3} and λ_{B4}) are orthogonal to the vertical planes carrying remaining two EFBGs (λ_{B1} and λ_{B2}). At zero inclination (θ = 0°), all the EFBGs are just immersed into a strategically chosen liquid of RI 1.456. When the sensor is tilted anti-clockwise in yz-plane (xz-plane), EFBG2 (EFBG3) starts getting exposed to air, while the EFBG1 (EFBG4) stays immersed throughout. In the case of clockwise inclinations in yz-plane (xz-plane), EFBG1 (EFBG4) gets exposed to air and EFBG2 (EFBG3) stays immersed. In all these cases, peak reflectivity of the section of EFBG exposed to air (R_A) keeps on increasing. This peak reflectivity can be expressed as (using Eq. 5.3 and Eq. 5.12),

$$R_A = \tanh^2[\kappa_A l_A] = \tanh^2\left[\kappa_A\left(\frac{\cos\theta}{\sin(\theta+\phi)} \times 0.01742\, x\theta\right)\right] \tag{5.13}$$

As can be observed from Eq. 5.13, peak reflectivity R_A not only depends on the parameters x and θ, but also on the critically important design parameter ϕ. Further, for fixed x and θ, lower

the value of ϕ, higher is R_A. Therefore, it is crucial to optimize ϕ in order to achieve best response characteristics for the proposed sensor. In the present investigation, ϕ is varied as 30º, 25º, 20º, and 15º. Owing to the experimental constraints, ϕ could not be made lower than 15º. Theoretically simulated response of EFBG (as an example, of EFBG2 fixed at ϕ = 15º) while varying the inclination angle (θ) in *y*-*z* plane from 0º to +10º in the step of 1º is depicted in Fig. 5.10. As can be observed, in the case of zero inclination (θ = 0º) there exists single reflection peak, which corresponds to EFBG entirely submerged into the liquid. As the tilt angle is increased, single reflection peak splits into two. The additional peak, appearing at left in Fig.5.10., corresponds to the section of EFBG getting revealed to air. Further, peak reflectivity for both the sections of EFBG2 (R_A and R_L) gets modulated in accordance to the applied tilt.

In order to gain a deeper understanding of the response characteristics of the proposed sensor, peak reflectivity for the section of the EFBG exposed to air, i.e., R_A, is calculated from the spectrum depicted in Fig. 5.10. It is important to mention that, being independent of the length of the EFBG, R_A is used to define sensor's characteristics. Afterwards, these peak reflectivities are plotted on a logarithmic scale (log[1-*R*]) against the tilt angles. Fig. 5.11 illustrates plot of log[1-R_A] against the tilt angles at various values of ϕ and fixed *x* (32 mm). As can be observed, peak reflectivity (R_A) increases with the applied tilt (which is expected as

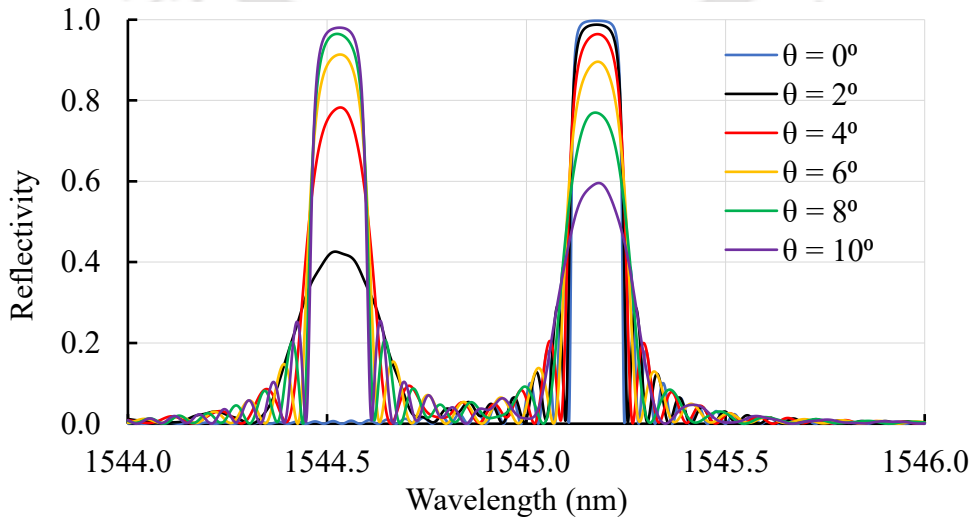

Figure 5.10: *Peak reflectivity of EFBG2 (fixed at ϕ = 15º) for θ* = 0º, 2º, 4º, 6º, 8º, 10º.

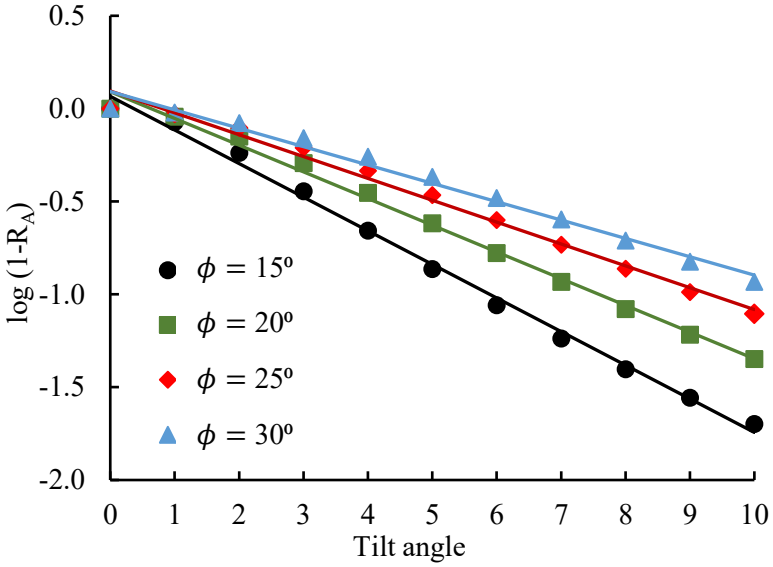

Figure 5.11: *Variation of reflectivity for the section of EFBG exposed to air with the applied tilt at different values of ϕ. x is fixed at 32mm.*

l_A increases). Response remains linear (on the logarithmic scale) as θ is varied from 0º to 10º. Sensitivity increases while decreasing the value of ϕ. Highest sensitivity of 1.81 dB/º with a linearity of $R^2 = 0.995$ is observed for the sensor employing $\phi = 15º$. Next, effect of x on the sensor's response is investigated. Fig. 5.12 illustrates the sensor response (log[1-R] vs θ) for two values of x (32 mm and 40 mm) while fixing EFBGs at $\phi = 15º$. As can be observed, changing the value of x by just 8 mm, sensitivity of the sensor increases by 33.2% and becomes 2.41 dB/º. Importantly, when the sensor is tilted in clockwise direction (from 0º to -10º), EFBG1 will respond exactly in the way, similar to EFBG2 in anticlockwise inclinations. In this scenario, EFBG2 remains ineffective. Thus, in totality, the sensor responds linearly over the dynamic range of -10º to +10º. In addition, response remains identical if the tilt is applied in xz-plane. These characteristic features of the proposed sensor enable it to monitor magnitude as well as the direction of the applied tilt. By critically selecting a liquid with low viscosity, a high degree of reversibility and repeatability is expected to be observed.

Moreover, peak reflectivity (R) remains unaffected by temperature variations. Temperature change shifts the center wavelength of the FBG. However, peak reflectivity,

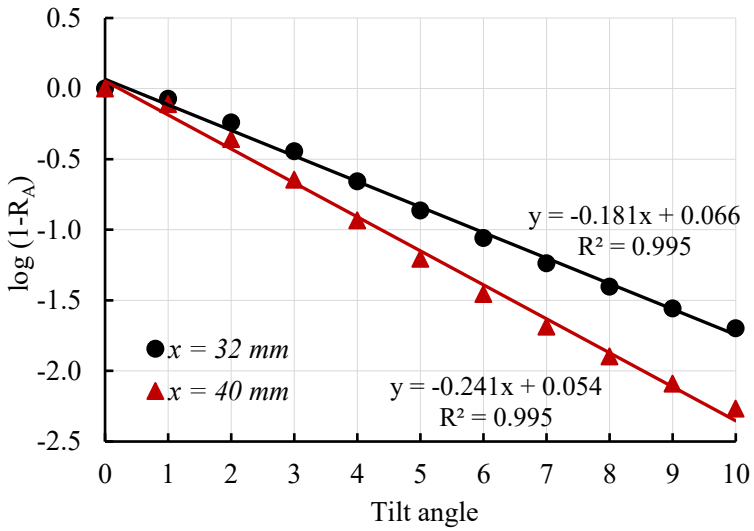

Figure 5.12: *Variation of reflectivity for the section of EFBG exposed to air with the applied tilt at two values of x. ϕ is fixed at* 15º.

which is utilized to monitor the applied tilt in this study, is not influenced by temperature fluctuations. Consequently, the problem of temperature cross-sensitivity gets inherently eliminated, rendering the sensor temperature-independent.

5.5 Conclusion

A novel all-optical tilt sensor that employes four EFBGs is theoretically demonstrated. Proposed sensor exploits effective RI sensitivity of an EFBG in order to achieve intensity modulation of the FBG spectrum. This modulation technique is utilized for the first time for the development of tilt sensor, to the best of author's knowledge. Response characteristics of the proposed sensor against tilt angle variations are theoretically investigated. Detailed theoretcial analysis shows that the reflectivity depends on tilt angle and the distance (x) of the EFBGs from the center of the sensor also. For x equal to 32 mm, expected sensitivity is 0.97 dB/°. Sensitivity increases to 1.20 dB/° as x increases to 40 mm. In order to capture applied tilt with better sensitivity and improve sensor performance, another novel design was proposed. The sensor characteristics of the new sensor design was also investigated theoretically. The maximum theoretical sensitivity for the new sensor design comes out to be 2.41 dB/°. Both the

proposed sensor designs eliminate the potential of noise/error due to any extraneous undesirable perturbations. Furthermore, both the sensors exhibit the ability to quantify the magnitude and the direction of inclination relative to the horizontal plane across the designated dynamic range of -10° to 10°. Additionally, as peak reflectivity of FBG spectra does not depend on the temperature variations, change in temperature will cause the centre wavelength of the FBGs to get shifted. But, the reflected peak, which is used to monitor the applied tilt in our work, remains unaffected by temperature fluctuations. Thus, the problem of temperature cross-sensitivity gets eliminated inherently.

Chapter 6 : Highly Sensitive and Temperature Insensitive Liquid Level Sensor Based on Fiber Bragg Grating

6.1 Introduction

Liquid level sensing is also equally critical for the structural health of certain infrastructures, particularly those exposed to water or liquid-related stress, such as bridges, dams, and flood barriers. Changes in water or liquid levels can exert pressure on structures, accelerating degradation or even causing catastrophic failures if not detected early. Along with this, liquid level sensors are also extensively important in various industries including fuel reservoirs, chemical industries, water and waste water management industries, food and beverage industries, petrochemicals, pharmaceuticals as well as in agricultural and residential use that involves storage tanks of considerable size with substantial depths (2-6 m) [84]-[86]. Along with improving the operational efficiency of industries, they also serve an extremely crucial role in guaranteeing safety while providing early prediction of flood by tracking the rising water levels, enabling early warnings and evacuation alerts in flood-prone areas. These applications require sensing systems that are capable of monitoring liquid level accurately (<0.5% FSR) and continuously across a measurement range. This measurement range is dictated by the targeted application and can be up to several meters [84]-[86], [114]. Few numbers of conventional liquid level sensors with good sensitivity have been proposed in the past few decades. However, their operations are limited because of their size, susceptibility to electromagnetic interference, or inability to adapt to potentially explosive, corrosive and conductive environments [87]–[89]. Later on, a few attempts have been made in order to develop all-optical liquid level sensors that overcome some of the major shortcomings of conventional sensors [90], [91]. However, they have their own major limitations of being highly alignment sensitive and incapable for remote sensing and multiplexing to name a few.

Technological advancements in the field of fiber optics and optoelectronics have greatly impacted sensing engineering with the development of optical fiber sensors that enable multi-parameter, remote and distributed sensing with extraordinarily high sensitivity. Consequently, numerous attempts have also been made in realizing optical fiber liquid-level sensors employing various configurations, e.g., etched fiber [17], [92], [93], standard optical fiber [94], [95], optical fiber interferometers [96]–[99] etc. Most importantly, the realization of in-fiber grating (FBG and LPG) has helped in making tremendous progress in all-optical sensing. In addition to carrying all the benefits offered by optical fiber sensors, the inherent self-referencing nature and the ability to multiplex multiple FBGs onto a single optical fiber channel make FBG-based sensors suitable for real-field applications [46]. FBG sensors, in general, employ wavelength modulation through strain-optic and thermo-optic effects when subjected to the applied strain and temperature perturbations. This makes FBG an inherent strain and temperature sensor. In order to design FBG sensor for parameters other than strain and temperature, a smart mechanism needs to be developed that maps the required parameter, generally, onto the strain domain and abandons the effect of temperature. Several attempts have been made in order to realize liquid level sensors based on FBG/EFBG [51], [100]–[104], LPG and tilted FBG [105]–[109]. For instance, Yun *et al.* [51] reported an EFBG based liquid level sensor that employed effective RI modulation mechanism. This sensor was characterised with a nonlinear response over the dynamic range of ~1.5 cm. Guo *et al.* [100] reported another FBG based liquid level sensor that employed a complex bending cantilever beam and column buoy structure. This sensor was unable to determine the direction of liquid level variation. Lai *et al.* [101] proposed liquid level sensor that employed dual sensor system incorporating FBG and fiber Fabry-Péro sensor. A linear response with the experimentally obtained sensitivity of 14.91 pm/cm (as against theoretically predicted sensitivity of 18.67 pm/cm) and a resolution of ~3 cm were observed. Sohn *et al.* [102] proposed another liquid level sensor where FBG

was embedded in a cantilever rod that was attached to a complex float structure. A linear response over a dynamic range of 0-36 cm with a sensitivity of 0.1 dB/cm was observed. In another sensor reported by Sheng *et al.* [103], EFBG was encapsulated in a half-polymer-filled metal cylinder. In comparison to the theoretically anticipated sensitivity of 2.15×10^{-5} cm^{-1} pm/cm, experimentally observed sensitivity for the proposed sensor was 1.526×10^{-5} cm^{-1} pm/cm. Almeida *et al.* [104], reported liquid level sensor where FBG was embedded in silicon rubber. A linear response with a maximum sensitivity of 1.56 pm/cm was observed. In summary, reported sensors employed very complex structure, exhibited limited operational range and in many cases theoretically expected response could not be achieved experimentally. Importantly, only few reported sensors, primarily involving complex design of optical fiber interferometer or the integration of FBGs with complex cantilever structures, exhibited the potential to meet the requirements as demanded in petrochemical or agricultural/residential applications [99], [100]–[102].

The main objective of the research reported in this chapter is to present a novel and very simple design strategy for the development of FBG based liquid level sensor. Proposed sensor exploits Archimedes' law of buoyancy [115]. The main objective of research carried out in this work is to realize a liquid level sensor with tunable response characteristics while achieving significantly high sensitivity, resolution and the measurement accuracy in order to match the requirements for applications in various industries such as petrochemical, agricultural fields, flood monitoring etc. In particular, proposed sensor offers advantages over the other interferometer/EFBG/FBG embedded cantilever-based liquid level sensors in terms of simplicity in design and customization of sensing performances for specific applications. Response characteristics of the proposed sensor is rigorously investigated theoretically and experimentally. Maximum discrepancy of the order of ±0.01nm is observed over the designed dynamic range of 30 cm. Experimental observations show that the proposed sensor

demonstrates the capability of achieving liquid level measurement with an excellent resolution of 0.006 cm (<0.02%FSR) and an exceptional accuracy of <0.03%FSR. Additionally, proposed sensor exhibits a very high level of reversibility and repeatability. Further, in the proposed sensing strategy, imprinting of the liquid level variations in the optical domain is achieved by decoding the liquid level information from the peak wavelength separation between two FBGs. This makes the sensor inherently temperature-insensitive. These attributes make the proposed sensor highly significant for practical/real-field applications.

6.2 Sensor design and operating principle

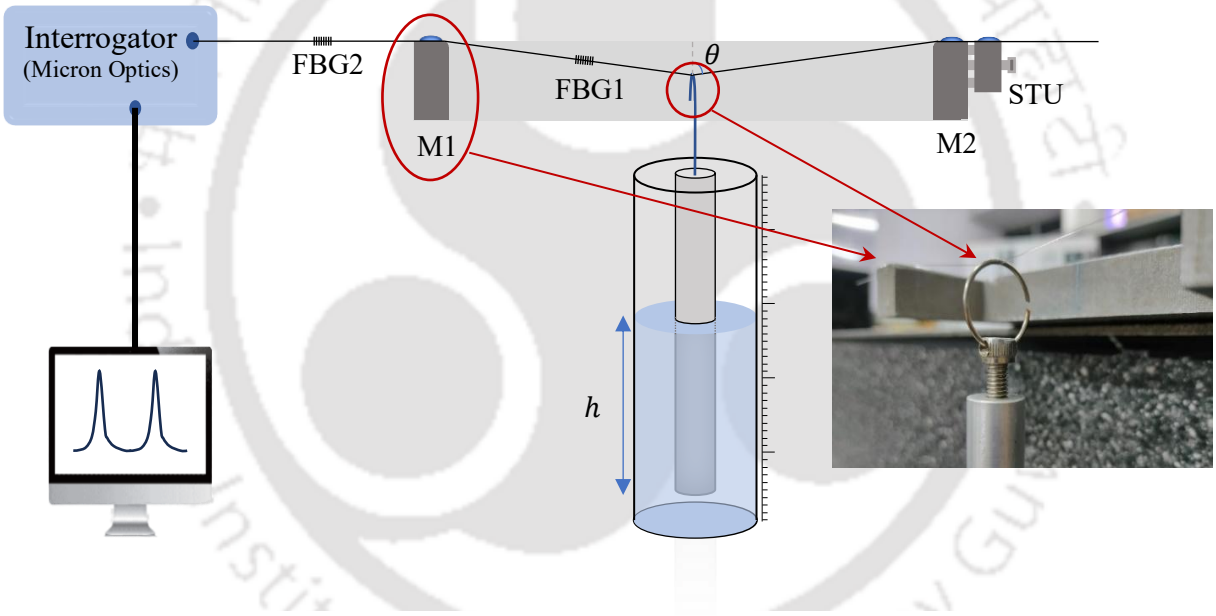

Figure 6.1: *Proposed FBG based liquid level sensor*

The schematic representation of the proposed FBG based liquid level sensor design is illustrated in Fig. 6.1. The design includes two metallic (aluminum) mounts M1 and M2 that are separated by a distance of $2l$ (= 12 cm). A specially designed metallic strain tuning unit (STU) is attached to M2. A single fiber carrying two FBGs is glued on M1 and STU in such a

way that FBG1 (λ_1) is placed nearly 3 cm on the right from M1, while FBG2 (λ_2) remained just outside (Fig. 6.1). After pre-straining the fiber using the STU, the fiber is glued on M2. A cylindrical mass of length *H* is then carefully and precisely mounted on the optical fiber exactly at the midpoint of the fiber length between the two mounts. The mounted cylindrical mass is then precisely positioned inside and along the axis of a graduated cylinder, which is used as the liquid tank (Fig. 6.1).

The operating principle of the proposed sensor is based on the Archimedes' law of buoyancy [115] and specially on the variation of effective weight of the cylindrical mass, when the liquid level in the tank varies from $h = 0$ (when liquid just touches the bottom of the mass) to $h = H$ (height of the cylinder). If F (= mg) is the weight of the cylinder and F_B is the buoyant force, the effective weight of the cylinder can be written as follow:

$$W = F - F_B = mg - m_l g = mg\left(1 - \frac{m_l}{m}\right) \tag{6.1}$$

Here, m_l is the mass of the displaced liquid by immersed cylinder. The mass of the cylinder of radius r, density ρ and height h is, $m = \pi r^2 \rho H$. For a liquid of density ρ_l, if the cylinder is immersed into the liquid by a length h, mass of the dispersed liquid can be expressed as $m_l = \pi r^2 \rho_l h$. Hence, the equation for the effective weight can be rewritten as,

$$W = mg\left(1 - \frac{\rho_l}{\rho} \cdot \frac{h}{H}\right) \tag{6.2}$$

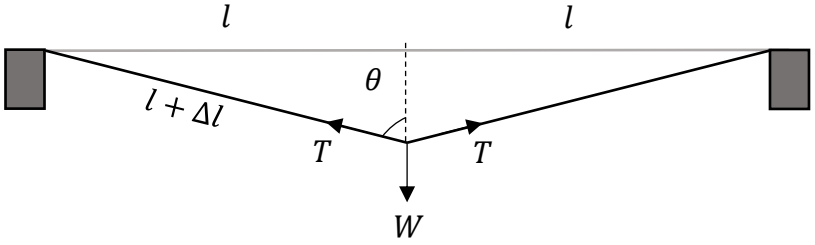

Figure 6.2: *Free body diagram of the proposed sensor.*

Using the free body diagram shown in Fig. 6.2, the tension(T) acting on the fiber due to suspension of cylinder can be expressed in terms of W as, $T = W/(2cos\theta)$. Here, θ is the angle made by the fiber with the vertical at its center (as shown in Fig. 6.2) when the cylindrical mass is hanged. Considering the full length of the fiber between the two mounts ($2l$) when the cylindrical mass is not hanged and the total elongation ($2\Delta l$) due to the suspension of the mass, one can write,

$$\cos\theta \cong \sqrt{(2\Delta l)/l} \tag{6.3}$$

As per the principles of mechanics, the Young's modulus (E) of the optical fiber can be mathematically represented as, $E = (T/A)/\Delta\epsilon$ [116]. Here, A is the cross-sectional area of the fiber and ϵ is the axial strain due to tension T. From the definition of E and using the expression for T and Eq. 6.3, we get,

$$\cos\theta = \left(\frac{W}{AE}\right)^{\frac{1}{3}} = \left(\frac{mg}{AE}\right)^{\frac{1}{3}}\left(1 - \frac{\rho_l}{\rho H}\cdot h\right)^{\frac{1}{3}} \tag{6.4}$$

Hence, using Eq. (3) and (4), the axial strain acting onto the fiber is expressed as [107],

$$\Delta\epsilon = \frac{\Delta l}{l} = \frac{\cos^2\theta}{2} = \frac{1}{2}\cdot\left(\frac{mg}{AE}\right)^{\frac{2}{3}}\left(1 - \frac{\rho_l}{\rho H}\cdot h\right)^{\frac{2}{3}} \tag{6.5}$$

Eq. 6.5 clearly indicates that as the cylinder gets immersed into the liquid, the strain keeps on decreasing accordingly and vice-versa. This changes in strain will induce shift in the Bragg wavelength of grating due to elastic and strain-optic effect. FBG is also sensitive towards ambient temperature variation due to thermal expansion and thermo-optic effect. The shift in Bragg wavelength due to strain and temperature variations for FBG written on single mode fiber is expressed as [39],

$$\frac{\Delta\lambda}{\lambda} = (1 - P_e)\Delta\epsilon + (\alpha + \xi)\Delta T \tag{6.6}$$

In the proposed sensor design configuration, the change in strain due to change in liquid level induces Bragg wavelength shift only in FBG1 (λ_1), whereas both the FBGs (λ_1 and λ_2) experience temperature induced change in Bragg wavelength. Hence,

$$\frac{\Delta\lambda_1}{\lambda_1} - \frac{\Delta\lambda_2}{\lambda_2} = (1 - P_e)\Delta\epsilon \tag{6.7}$$

Assuming, $\lambda_1 \approx \lambda_2$ and $\Delta\lambda_i \ll \lambda_i$ $(i = 1,2)$, using Eq. 6.5, Eq. 6.7 can be rewritten as,

$$\Delta(\lambda_1 - \lambda_2) = \lambda_1(1 - P_e)\frac{1}{2} \cdot \left(\frac{mg}{AE}\right)^{\frac{2}{3}} \left(1 - \frac{\rho_l}{\rho H} \cdot h\right)^{\frac{2}{3}} \tag{6.8}$$

As can be observed from Eq. 6.8, shift in wavelength difference $\Delta(\lambda_1 - \lambda_2)$ is dependent on the liquid level (h) along with a dependency on the mass of cylinder (m), and the density of the liquid (ρ_l). It is crucial to note that the temperature-induced wavelength shift of both FBGs occurs in the same direction. Therefore, the proposed design makes the sensor inherently temperature insensitive by mapping the liquid level to shift in wavelength difference instead of absolute Bragg wavelength peaks of FBGs. It is worth noting that, by choosing a cylinder with a different mass, the sensing capabilities of the proposed device can be adjusted to match the needs of a particular real-field application.

6.3 Experiment and result

To realize the proposed liquid level sensor, two cylindrical rods made of aluminium were machined with precision, each with an outer diameter of 16 mm and a length of 30 cm. One rod was hollow (m = 110g) with metallic caps securely sealing both ends, and the other one was solid (m = 160g). A graduated cylindrical beaker with dimensions bigger than those of the rods was used as the liquid tank, and distilled water was used for the liquid level variation. Two FBGs, inscribed onto a hydrogen-loaded single-mode fiber employing the phase-mask

technique were used for the sensor. The fiber parameters are provided in chapter 2. The Bragg wavelength of the two FBGs were $\lambda_1 = 1551.581$ nm and $\lambda_2 = 1554.670$ nm. The fiber with both the FBGs was glued using a bi-component epoxy resin and was left to cure for 24 hours to ensure strong adhesion. Strain tuning unit (STU) was employed to pre-strain the fiber, preventing any slackening. For the suspension of the cylinder on the fiber, a custom hook, featuring an M4 screw and a circular ring was devised and threaded at one end of the rod (inset, Fig. 6.1). Extreme attention was directed towards the accurate suspension of the cylindrical mass, precisely at the midpoint between the two mounts.

The experiment was conducted by inserting the cylinder into the graduated liquid tank. Initially, the liquid was filled until it barely touched the bottom of the cylinder, denoted by $h = 0$. Then the liquid level was increased by gradually filling up the tank with steps of 2 cm and spanning the entire length of the suspended cylinder (H = 30 cm). When the entire cylinder got immersed, the liquid level was then gradually reduced in a step of 2 cm by draining the liquid from the tank. It is very crucial to mention that, a very precisely controlled liquid pouring and draining system, comprising one submersible motor and pipes, was employed to precisely change the liquid level. This ensured the avoidance of any mechanical vibrations on the liquid surface during the insertion and extraction processes. During the experiment, the reflection spectra of both the FBGs were monitored using a robust and compact four channel FBG interrogator (Micron optics, resolution: 0.5pm).

Fig. 6.3 depicts the temporal variation of $\Delta(\lambda_1 - \lambda_2)$ in case of the hollow cylinder. Initially the rod was not immersed into the liquid. Then the liquid level was increased by 2 cm. After increasing the liquid level, we waited for sufficient time in order to mitigate any vibration that may get generated due to the liquid level variation, and to get a stabilized sensor response.

After the sensor response got settled, the liquid level was increased again by 2 cm. This process was repeated till the entire rod got submerged within the liquid. When the entire rod was immersed, the liquid level was then decreased in steps of 2 cm. The response of the sensor was recorded after stabilization at every descending liquid level. As the liquid level was increasing, the cylindrical mass was consistently submerging into the liquid. Consequently, an abrupt shift in $\Delta(\lambda_1 - \lambda_2)$ was observed owing to the reduced strain into the fiber. This reduction in strain can be attributed to the decreased effective weight of the cylinder (W) in the presence of the buoyant force. Conversely, a reduction in the liquid level by the same amount led to a decrease in the buoyant force, subsequently increasing the effective weight of the cylinder (W). This change resulted in an increased strain in the fiber, and hence, a red-shift in $\Delta(\lambda_1 - \lambda_2)$. In Fig. 6.3, each step represents a liquid level change of 2 cm. The first half depicts the sensor response while increasing the liquid level and the second half corresponds to the sensor response for the decreasing liquid level.

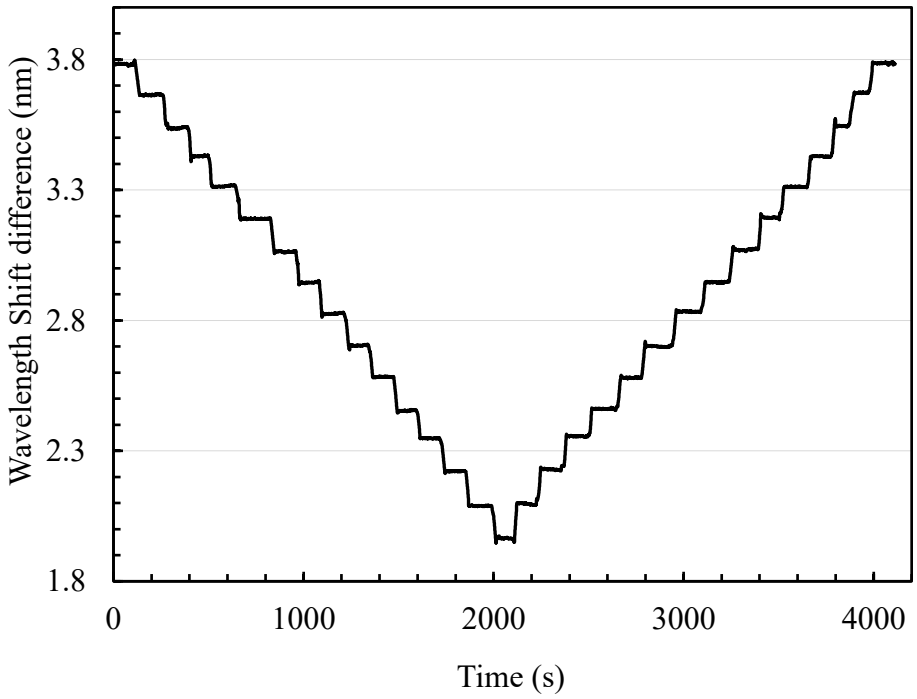

Figure 6.3: *Temporal variation of shift in wavelength difference between two FBGs while increasing and decreasing of liquid level, in case of hollow rod (m* = 110*g)*

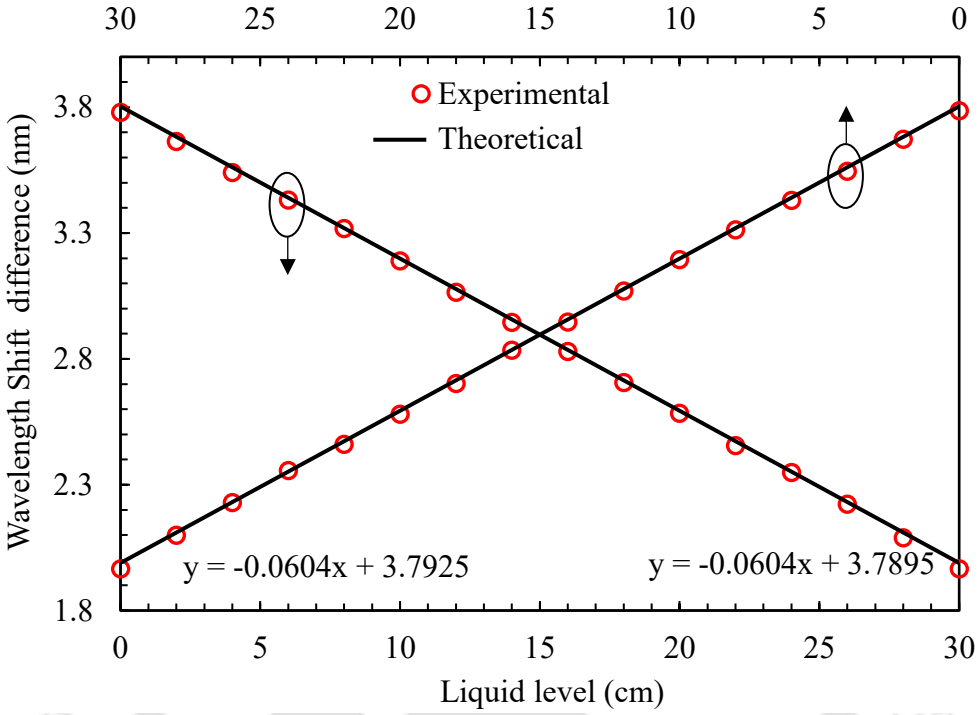

Figure 6.4: *Characteristic curve, $\Delta(\lambda_1-\lambda_2)$ vs. h, obtained from data reported in Fig. 6.3*

Specifically, the temporal variation of $\Delta(\lambda_1 - \lambda_2)$ for the liquid level variation of 2 cm is observed to be about 121pm. It is worth noting that, when the liquid level is brought back to zero ($h = 0$), the sensor's response fully recovers to its initial value. This demonstrates the high capability for recovery and reversibility of the proposed sensor. To get the exact sensor response, $\Delta(\lambda_1 - \lambda_2)$ from the stabilized portions of Fig. 6.3 is plotted against the liquid level in Fig. 6.4 for both increasing and decreasing liquid levels. The lower *x*-axis corresponds to the increasing liquid level, whereas, the upper *x*-axis depicts the decreasing liquid level. In accordance to that, the *y*-axis represents the sensor response corresponding to increasing and decreasing liquid levels. In the same graph, the theoretical response is also plotted as obtained from Eq. 6.8. The sensor response is observed to be linear over the entire dynamic range of 30 cm, as predicted by Eq. 6.8. Importantly, an excellent agreement is observed between the experimentally observed and theoretically predicted responses. Sensitivity of the sensor employing hollow cylinder is determined to be 60.4 pm/cm (R^2 = 0.9999) with a maximum

observed discrepancy of the order of ±0.01 nm for both, increasing and decreasing liquid levels. Considering the resolution of the FBG interrogator, the proposed sensor demonstrates the capability to achieve an exceptional resolution of 0.008 cm (<0.026%FSR). The standard deviation for five measurements at each value of h is observed to be ±0.7 pm. This reveals the high repeatability of the proposed sensor. Consequently, the accuracy of the sensor is observed to be <0.04%FSR.

It is important to highlight that the response of the sensor, as indicated by Eq. 6.8, is closely related to the mass of the cylindrical rod, which is utilized in constructing the sensor. To experimentally validate this conjecture, identical experiments were carried out by employing a solid cylinder of identical dimensions, but of mass 160g. In this case also, the liquid level was varied in the steps of 2 cm and the corresponding response was recorded after stabilization. The temporal variation of $\Delta(\lambda_1 - \lambda_2)$ in the case of solid cylinder is depicted in Fig. 6.5. It is worth noting that, the sensor's response recovers fully to its initial value, when the liquid level is brought back to zero (h = 0). In order to get a better insight, sensor response for each liquid level is extracted from stabilized region of the temporal response curve and plotted in Fig. 6.6. In this figure also, the lower x-axis corresponds to the increasing liquid level, whereas, the upper x-axis depicts the decreasing liquid level. In accordance to that, the y-axis represents the sensor response corresponding to increasing and decreasing liquid levels. In the same graph, theoretical response, obtained from Eq. 6.8, is also plotted. As can be seen, sensor response is observed to be linear over the entire dynamic range of 30 cm. Further, an excellent agreement is observed between the experimentally observed and theoretically predicted responses. The measured sensitivity of the sensor with the solid cylinder for both, increasing and decreasing liquid levels is determined to be 77.5 pm/cm (R^2 = 0.9999) with a maximum observed discrepancy of the order of ±0.01 nm. Considering the resolution of the FBG interrogator, the proposed sensor demonstrates the capability to achieve an exceptional

resolution of 0.006 cm (<0.020%FSR). The standard deviation for five measurements at each value of *h* establishes an excellent accuracy of <0.03%FSR in this case

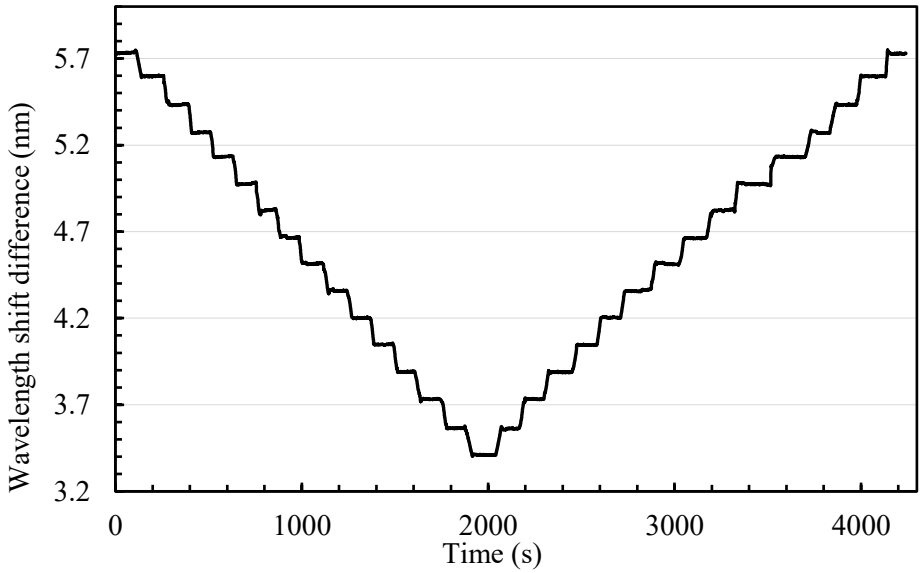

Figure 6.5: *Temporal variation of shift in wavelength difference between two FBGs while increasing and decreasing of liquid level, in case of solid rod (m =* 160*g)*

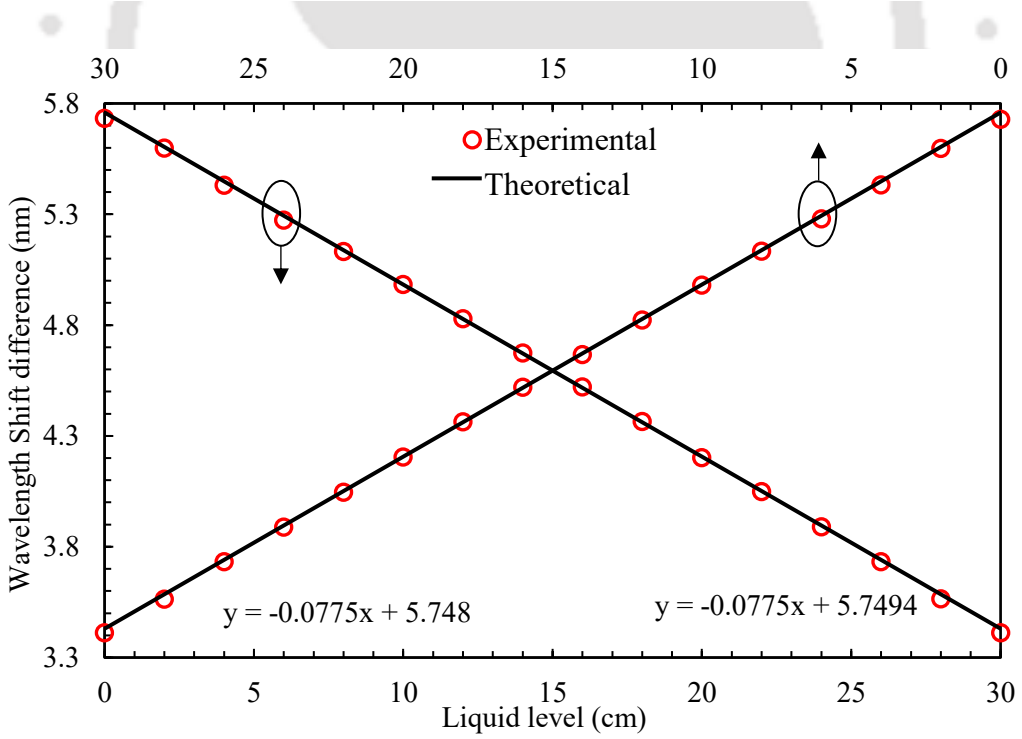

Figure 6.6: *Characteristic curve, $\Delta(\lambda_1-\lambda_2)$ vs. h, obtained from data reported in Fig. 6.5.*

It is also worth noting that, the sensor response in both the cases are in excellent agreement with the theoretical response. To validate this observation further, analytical treatment using Eq. 6.8 can be employed. For the considered liquid level variations, the theoretical sensitivity is proportional to $m^{2/3}$. Hence, the ratio of the theoretical sensitivities for the two cylinders is,

$$\left.\frac{S_{Solid}}{S_{Hollow}}\right|_{theo} = \left(\frac{m_{Solid}}{m_{Hollow}}\right)^{2/3} = \left(\frac{160}{110}\right)^{2/3} = 1.28 \tag{6.9}$$

The ratio of the experimentally obtained sensitivities for both the cylinders is,

$$\left.\frac{S_{Solid}}{S_{Hollow}}\right|_{exp} = \frac{77.5}{60.4} = 1.28 \tag{6.10}$$

Eq. 6.9 and 6.10 establishes the fact that the response of the proposed sensor is in excellent agreement with the anticipated theoretical responses. Moreover, this validates the potential to customize the sensitivity of the proposed sensor for specific applications by carefully varying the mass of the suspended cylindrical rod. However, there exists an upper limit in selecting the mass of the suspended rod. This limit is dictated by the maximum allowable weight that can be suspended on an optical fiber without breaking it. In the light of the fact that optical fiber utilized in this experiment (Corning SMF-28e+ Optical Fiber) has been already tested successfully to withstand a tensile stress $\sigma_T \geq 0.7$ GPa [117], the maximum permissible weight for the mass is determined to be, $m = \sigma_T.A.(2\cos\theta)/g \approx 0.213$ kg. Further, it is worth mentioning that the Buoyant force depends solely on the volume of the displaced liquid, which in turn, depends on the volume of the mass immersed in the liquid. These two facts give ample room to tailor the sensor's characteristics (e.g., sensitivity, dynamic range etc.) as per the need of desired application by simply redesigning the shape and geometry as well as the length of the suspended object while keeping the mass fixed under the maximum limit. Furthermore, the

material used for the rod can be chosen to ensure that the sensor can operate effectively in various types of liquids, including conductive and erosive ones.

Table 6.1: Response comparison of the proposed sensor with other optical liquid level sensor

Ref.	Sensing Method	Sensitivity	Resolution
[91]	Light guide plate	–	0.200 cm
[95]	Plastic optical fiber	–	0.167 cm
[94]	Plastic optical fiber polished	–	34 cm
[101]	FBG	14.91 pm/cm	3 cm
[102]	FBG	0.1 dB/cm	–
[103]	FBG	23.50 pm/cm	–
[104]	FBG	1.56 pm/cm	–
This work	FBG (Hollow cylinder)	60.40 pm/cm	0.008 cm
	FBG (Solid cylinder)	77.50 pm/cm	0.006 cm

Next, the research investigation delves into a comparative analysis of the performance characteristics of the proposed liquid level sensor with the other FBG-based liquid level sensors reported in the literature. Table I provides a comprehensive overview of key parameters, e.g., sensitivity and resolution that are key to underline the effective sensing capabilities of a given sensor. As can be observed from the table, among all the previously reported works, the maximum sensitivity was achieved by Sheng *et al.* [103] whereas, the best resolution was achieved by Jing *et al.* [95]. All the other reported sensors exhibit either moderate sensitivity or comparatively lower resolution. On the other hand, proposed sensor outperforms all the previously reported FBG based liquid level sensors. Highest sensitivity is observed for the proposed sensor, which is over three times greater than the sensitivity reported in [103]. An outstanding resolution is also observed for the proposed sensor, which is ~28 times better than the sensor with best resolution reported in [95]. The remarkable sensitivity and the extremely

high resolution (indicative of the sensor's capacity to precisely measure variations in liquid levels) underscore sensor's ability to discern even minute changes in liquid levels, rendering it very significant for applications demanding high precision, such as, in chemical processing; industrial storage, oil, gas and petrochemical industries; pharmaceutical manufacturing; or in environmental surveillance, e.g., flood monitoring, groundwater monitoring etc.

Next, it is very crucial to eliminate the temperature cross-sensitivity of the reported sensor for real-field applications. Although, the sensor is designed aiming at mitigating temperature effects inherently, it is important to examine the impact of ambient temperature fluctuations on its performance, experimentally. For this, experiments were carried out employing the solid cylinder. Liquid level was set at a fixed height of h = 14 cm. Both the FBGs were exposed to a specially designed water bath at a temperature of ~60°C. As the water naturally cooled to the room temperature (~25°C), corresponding shift in wavelength difference, $\Delta(\lambda_1-\lambda_2)$, was measured. The thermal response of the sensor is depicted in Fig. 6.7. The maximum observed temperature cross-sensitivity is ~3 pm/°C, which is about 121 times less in comparison to the shift experienced by an uncompensated FBG under identical temperature variation conditions. This remarkably low temperature cross-sensitivity s

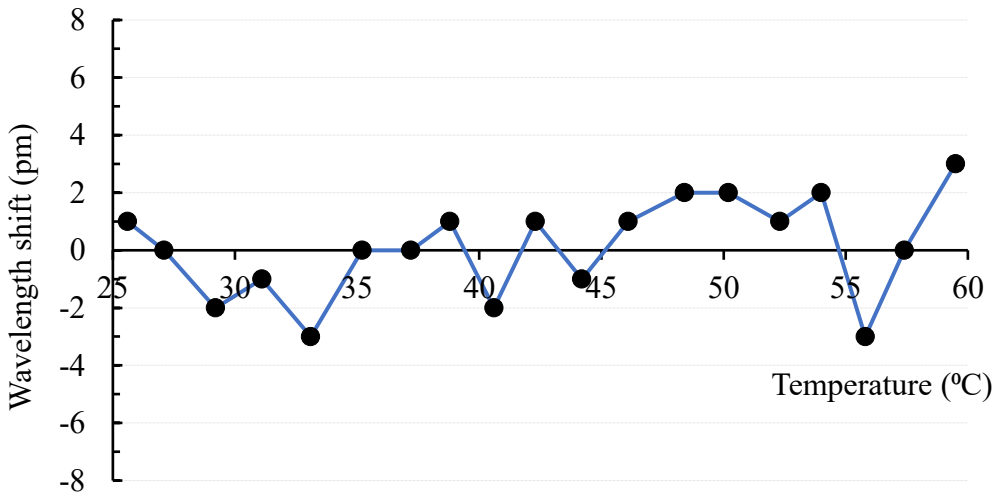

Figure 6.7: *Thermal response of the sensor with solid rod at a liquid level h* = 14 *cm*

establishes the high degree of temperature independent nature of the proposed sensor, making it suitable for real-world applications where continuous fluctuations in ambient temperature are unavoidable.

Finally, the proposed sensor provides significant flexibility in customizing the characteristic curve for specific applications, as the buoyant force is solely dependent on the volume of the immersed mass. This offers a wide range of possibilities to achieve different tailored response. For example, we can use cones, hollow cylinders, or combinations of different objects with different sizes. This also enable the creation of customized non-linear characteristic curves, which can be useful for specific needs. By taking advantage of different shapes and combinations, we can customize the sensor to work well in a wide range of applications.

6.4 Conclusion

In this work, a simple and novel design strategy is proposed for the realization of an FBG based all-optical liquid level sensor based on Archimedes' law of buoyancy. The main objective of this work is to enhance the sensitivity towards liquid level variation while achieving significantly high resolution to match the requirements for applications in various industries such as petrochemical, agricultural fields, flood monitoring etc. Response characteristics of the proposed sensor is theoretically investigated and experimentally established. The sensor exhibits an outstanding maximum sensitivity of 77.5 pm/cm, coupled with an exceptionally high resolution of 0.006 cm (<0.020% FSR) and an accuracy of <0.03% FSR across the designed dynamic range of 30 cm. Furthermore, this sensor displays excellent reversibility and repeatability following an excellent agreement with the theoretical response. Moreover, the sensor validates the potential to customize the sensitivity for specific applications (such as petrochemical, agricultural fields, flood monitoring etc.) by carefully varying the mass of the

suspended rod within the maximum allowable mass limit, constrained by the predetermined maximum tensile stress endurance of SMF. The fundamental principle underlying this sensing approach involves mapping the variation in liquid level to the shift in wavelength difference between the two FBGs. This makes the sensor inherently insensitive towards any temperature fluctuation. These characteristics render the proposed sensor highly promising for practical applications in real-world scenarios. Additionally, the measuring range of proposed sensor can be adjusted to fit the needs of different applications by altering the length of the cylindrical rod suspended from the fiber. It is important to note that the suspended mass can be made from a wide range of materials, allowing our FBG liquid level sensor to be used with all types of liquids, including conductive and erosive ones.

Chapter 7 : Conclusion and Future work

7.1 Conclusion

This thesis successfully presents the design and development of novel all-optical Fiber Bragg Grating (FBG)-based tilt and liquid level sensors for structural health monitoring (SHM) and other real-field applications. The primary goal is to design sensors with high sensitivity, exceptional angular resolution, and minimal discrepancy, while ensuring stability and temperature insensitivity for real-world applications. The research's novelty lies in its unique sensor designs that integrate tunable response characteristics with inherent temperature compensation. Initially, a novel, temperature-insensitive, all-optical FBG-based tilt sensor is introduced. This sensor allows tuning of its response characteristics through variable loaded rod mass. This sensor exhibits high sensitivity (0.0300 nm/°), high accuracy (±0.033°), minimal discrepancy (±0.001 nm), and angular resolution (0.0167°), with experimental results closely matching theoretical predictions. To further improve sensor performance, another novel temperature-insensitive FBG-based all-optical tilt sensor design is proposed, offering improved sensitivity (0.0415 nm/°) across a dynamic range of ±10°. This design features tunable response characteristics via a loaded mass, delivering high accuracy (±0.024°), minimal deviation (±0.001 nm), and an angular resolution of 0.012°. Advancing the design further, another novel, temperature-insensitive FBG-based tilt sensor is developed, achieving remarkable sensitivity (0.3198 nm/°), exceptional accuracy (±0.0031°), minimal discrepancy (±0.001 nm), and outstanding angular resolution (0.0016°). This design also offers superior performance with tunable response characteristics. In all the three sensor designs proposed above, the experimental results closely matching theoretical predictions. Furthermore, all the sensors demonstrate high repeatability and reliability throughout its operational range. Additionally, the sensors work by modulating the wavelength separation between two FBGs in response to

tilt, making them inherently temperature insensitive. In the next part of the research, instead of traditional wavelength modulation mechanism, intensity modulation of the FBG spectrum that exploits the effective RI sensitivity of EFBG is used to develop novel all optical tilt sensor. A theoretical sensitivity of 1.20 dB/° was achieved with the first proposed design strategy. The sensitivity further enhanced to 2.41 dB/° in an improved sensor design. Both the designs are capable of measuring magnitude and direction of inclination within a ±10° range. The innovative application of EFBG introduces a new approach in tilt sensing technology. In the final phase, an all-optical, temperature-insensitive FBG-based liquid level sensor is developed, employing Archimedes' principle for precise measurements. This sensor delivers high sensitivity (77.5 pm/cm) and high resolution (0.006 cm), with minimal discrepancy (±0.01 nm) over a 30 cm dynamic range and outstanding accuracy (<0.03% FSR). Its tunable response characteristics are validated by experimental results. The novelty of this design lies in leveraging buoyancy principles for accurate liquid level sensing. Overall, this research successfully presents advanced, high-performance all-optical FBG-based sensors for tilt and liquid level measurements, offering significant contributions to the field of structural health monitoring through innovative design strategies and novel sensing techniques.

7.2 Future scope

Building upon the successful development of novel all-optical FBG-based tilt and liquid level sensors, numerous opportunities exist for further exploration, particularly in enhancing their applicability and integration within structural health monitoring (SHM) systems. Among the five tilt sensors proposed in this thesis, the last two designs have been analyzed theoretically. An immediate research direction is to fabricate these sensor designs and conduct comprehensive experimental investigations to validate their response characteristics. Another crucial area for advancement involves the robust packaging and miniaturization of these sensors. Employing lightweight, durable, and corrosion-resistant materials for advanced

encapsulation will enhance their resilience in harsh environments, ensuring long-term stability and consistent performance. Miniaturization will enable seamless integration into complex and confined structural spaces, improving practicality and adaptability without compromising sensor functionality. Furthermore, collaboration with industry partners for large-scale production and commercialization will help transition these sensors from laboratory prototypes to practical SHM solutions, effectively addressing market demands and regulatory standards. By addressing these future research directions, the performance, scalability, and applicability of FBG-based sensors can be further refined and effectively integrated into next-generation SHM systems, ultimately contributing to safer, more resilient, and intelligently managed infrastructure.

References

[1] B. P. Pal, "Fundamentals of fiber optics in telecommunication and sensor systems," *New Age Inc*, 2003.

[2] P. J. Schubert and J. H. Nevin, "A polyimide-based capacitive humidity sensor," *IEEE Trans. Electron Devices,* vol. ED-32, no. 7, pp. 1220–1223, 1985.

[3] M. Suster, J. Guo, N. Chaimanonart, W. H. Ko, and D. J. Young, "A high-performance MEMS capacitive strain sensing system," *J. Microelectromechanical Syst.,* vol. 15, no. 5, pp. 1069–1077, 2006.

[4] H. Seidel, H. Riedel, R. Kolbeck, G. Mück, W. Kupke, and M. Königer, "Capacitive silicon accelerometer with highly symmetrical design," *Sens. Actuators A Phys.,* vol. 21, no. 1–3, pp. 312–315, 1990.

[5] H. Kautsky and A. Hirsch, "Optical sensor for low level oxygen detection," *Chem. Ber.,* vol. 64, p. 2677, 1931.

[6] X. Ge, Y. Kostov, and G. Rao, "High-stability non-invasive autoclavable naked optical CO2 sensor," *Biosens. Bioelectron.,* vol. 18, no. 7, pp. 857–865, 2003.

[7] S. K. Lee and I. Okura, "Porphyrin-doped sol-gel glass as a probe for oxygen sensing," *Anal. Chim. Acta,* vol. 342, no. 2–3, pp. 181–188, 1997.

[8] J. J. Lee and M. Shinozuka, "A vision-based system for remote sensing of bridge displacement," *NDT E Int.,* vol. 39, no. 5, pp. 425–431, 2006.

[9] R. Sawada, E. Higurashi, and T. Ito, "Monolithically integrated optical displacement sensor based on triangulation and optical beam deflection," *Appl. Opt.* Vol. 38, Issue 9, pp. 1746-1751, vol. 38, no. 9, pp. 1746–1751, 1999.

[10] F. Xiaoyong and C. Maosheng, "Theoretical analysis of 2D laser angle sensor and several design parameters," *Opt. Laser Technol.,* vol. 34, no. 3, pp. 225–229, 2002.

[11] R. J. Hoss and E. A. Lacy, "Fiber Optics", *Pearson Education*, 1993.

[12] K. T. V. Grattan and T. Sun, “Fiber optic sensor technology: an overview,” *Sens. Actuators A Phys.,* vol. 82, no. 1–3, pp. 40–61, 2000.

[13] E. Udd and E. Udda, “An overview of fiber-optic sensors,” *Rev. Sci. Instrum.,* vol. 66, no. 8, pp. 4015–4030, 1995.

[14] A. Kersey and B. Culshaw, “Fiber-Optic Sensing: A Historical Perspective,” *J. Lightwave. Technol.* Vol. 26, Issue 9, pp. 1064-1078, 2008.

[15] H. Y. Fu, H. Y. Tam, L. Y. Shao, X. Dong, P. K. A. Wai, C. Lu, and S. K. Khijwania, “Pressure sensor realized with polarization-maintaining photonic crystal fiber-based Sagnac interferometer,” *Appl. Opt.*, vol. 47, no. 15, pp. 2835–2839, 2008.

[16] Y. G. Lee, H. K. Jang, D. H. Kim, and C. G. Kim, “Development of a mirror mounted fiber optic inclinometer,” *Sens. Actuators A Phys.,* vol. 184, pp. 46–52, 2012.

[17] Y. Jiang, W. Jiang, B. Jiang, A. Rauf, C. Qin, and J. Zhao, “Precise measurement of liquid-level by fiber loop ring-down technique incorporating an etched fiber,” *Opt. Commun.*, vol. 351, pp. 30–34, 2015.

[18] C. Yang, S. Chen, and G. Yang, “Fiber optical liquid level sensor under cryogenic environment,” *Sens. Actuators A Phys.,* vol. 94, no. 1–2, pp. 69–75, 2001.

[19] A. N. Starodumov, L. A. Zenteno, D. Monzon, and E. De La Rosa, “Fiber Sagnac interferometer temperature sensor,” *Appl. Phys. Lett.,* vol. 70, no. 1, pp. 19–21, 1997.

[20] J. Zheng and S. Albin, “Self-referenced reflective intensity modulated fiber optic displacement sensor,” *Optical Engineering,* vol. 38, no. 2, pp. 227–232, 1999.

[21] M. Q. Feng and D. H. Kim, “Novel fiber optic accelerometer system using geometric moiré fringe,” *Sens. Actuators A,* vol. 128, no. 1, pp. 37–42, Mar. 2006.

[22] Y. Jung, T. P. Newson, M. Belal, Z. Song, and G. Brambilla, “Optical fiber microwire current sensor,” *Opt. Lett.* Vol. 35, Issue 18, pp. 3045-3047, 2010.

[23] A. Cruden, I. Andonovic, Z. J. Richardson, and J. R. McDonald, “Opticalcrystal based devices for current and voltage measurement,” *IEEE Trans. Power Deliv.,* vol. 10, no. 3, pp. 1217–1223, 1995.

[24] T. Bao, J. Wang, and Y. Yao, "A fiber optic sensor for detecting and monitoring cracks in concrete structures," *Sci. China Technol. Sci.,* vol. 53, no. 11, pp. 3045–3050, 2010.

[25] S. Liehr, P. Lenke, M. Wendt, K. Krebber, M. Seeger, E. Thiele, "Polymer optical fiber sensors for distributed strain measurement and application in structural health monitoring," *IEEE Sens. J.,* vol. 9, no. 11, pp. 1330–1338, 2009.

[26] D. Monzón-Hernández and J. Villatoro, "Low-Cost Optical Fiber Refractive-Index Sensor Based on Core Diameter Mismatch," *J. Lightwave. Technol.*, vol. 24, no. 3, pp. 1409, 2006.

[27] A. A. Velikosel'tsev, A. N. Tkachenko, A. M. Boronakhin, D. B. Pukhov, and A. A. Yankovskiĭ, "Fiber-optic rotation sensors for seismic measurements," J. Opt. Technol. Vol. 77, Issue 7, pp. 447-451, 2010.

[28] Y. Li, X. Wang, and X. Bao, "Sensitive acoustic vibration sensor using single-mode fiber tapers," *Appl. Opt.*, Vol. 50, Issue 13, pp. 1873-1878, 2011.

[29] B. Schyrr, S. Pasche, E. Scolan, R. Ischer, D. Ferrario, J. A. Porchet, and G. Voirin, "Development of a polymer optical fiber pH sensor for on-body monitoring application," *Sens. Actuators B Chem.,* vol. 194, pp. 238–248, 2014.

[30] J. B. Jensen, P. E. Hoiby, G. Emiliyanov, O. Bang, L. H. Pedersen, and A. Bjarklev, "Selective detection of antibodies in microstructured polymer optical fibers," *Opt. Express,* vol. 13, no. 15, pp. 5883–5889, 2005.

[31] R. Aneesh and S. K. Khijwania, "Zinc oxide nanoparticle based optical fiber humidity sensor having linear response throughout a large dynamic range," *Appl. Opt.* Vol. 50, Issue 27, pp. 5310-5314, 2011.

[32] H. Y. Fu, S. K. Khijwania, H. Y. Tam, P. K. A. Wai, and C. Lu, "Polarization-maintaining photonic-crystal-fiber-based all-optical polarimetric torsion sensor," *Appl. Opt.* Vol. 49, Issue 31, pp. 5954-5958, 2010.

[33] D. A. Krohn, T. MacDougall, and A. Mendez, "Fiber optic sensors: Fundamentals and applications: Fourth edition," *Fiber Opt. Sensors Fundam. Appl. Fourth Ed.,* pp. 1–317, 2015.

[34] D. McCarthy, S. O'Keeffe, E. Lewis, D. G. Sporea, A. Sporea, I. Tiseanu, P. Woulfe, and J. Cronin, "Radiation dosimeter using an extrinsic fiber optic sensor," *IEEE Sens. J.*, vol. 14, no. 3, pp. 673–685, 2014.

[35] P. M. Tracey, "Intrinsic Fiber-Optic Sensors," *IEEE Trans. Ind. Appl.,* vol. 27, no. 1, pp. 96–98, 1991.

[36] K. O. Hill and G. Meltz, "Fiber Bragg grating technology fundamentals and overview," *J. Lightwave. Technol.,* vol. 15, no. 8, pp. 1263–1276, 1997.

[37] A. Ghatak and K. Thyagarajan, "Introduction to Fiber Optics", *Cambridge University Press*, 2011.

[38] M. R. Shenoy, S. K. Khijwania, A. Ghatak, and B. P. Pal, "Fiber optics through experiments", *Viva Books*, 2009.

[39] A. Othonos, "Fiber Bragg gratings," *Rev. Sci. Instrum.,* vol. 68, no. 12, pp. 4309–4341, 1997.

[40] R. Kashyap, "Fiber Bragg Gratings", Second Edition, *Elsevier*, 2009.

[41] Y. J. Rao, "In-fibre Bragg grating sensors," *Meas. Sci. Technol.,* vol. 8, no. 4, p. 355, 1997.

[42] P. S. Reddy, R. L. Sai Prasad, D. Sen Gupta, M. Sai Shankar, K. Srimannarayana, U. K. Tiwari, and V. Mishra, "A simple FBG sensor for strain–temperature discrimination," *Microw. Opt. Technol. Lett.,* vol. 53, no. 5, pp. 1021–1024, 2011.

[43] Y. Zhao and Y. Liao, "Discrimination methods and demodulation techniques for fiber Bragg grating sensors," *Opt. Lasers Eng.,* vol. 41, no. 1, pp. 1–18, 2004.

[44] A. Méndez, "Fiber Bragg grating sensors: a market overview," *Proc. SPIE 6619*, Third European Workshop on Optical Fibre Sensors, vol. 6619, pp. 44–49, 2007.

[45] M. Majumder, T. K. Gangopadhyay, A. K. Chakraborty, K. Dasgupta, and D. K. Bhattacharya, "Fibre Bragg gratings in structural health monitoring—Present status and applications," *Sens. Actuators A Phys.,* vol. 147, no. 1, pp. 150–164, 2008.

[46] D. A. Jackson, L. Reekie, A. B. L. Ribeiro, and J. L. Archambault, “Simple multiplexing scheme for a fiber-optic grating sensor network,” *Opt. Lett. Vol. 18, Issue 14, pp. 1192-1194*, vol. 18, no. 14, pp. 1192–1194, 1993.

[47] A. D. Kersey, M. A. Davis, H. J. Patrick, M. LeBlanc, K. P. Koo, C. G. Askins, M. A. Putnam, and E. J. Friebele, “Fiber Bragg grating sensors,” *J. Lightwave Technol.* 15, 1442–1463, 1997.

[48] J. M. López-Higuera, L. R. Cobo, A. Q. Incera, and A. Cobo, “Fiber optic sensors in structural health monitoring,” *J. Lightwave. Technol.,* vol. 29, no. 4, pp. 587–608, 2011.

[49] P. M. Ferreira, M. A. Machado, M. S. Carvalho, and C. Vidal, “Embedded Sensors for Structural Health Monitoring: Methodologies and Applications Review,” *Sensors,* vol. 22, no. 21, p. 8320, 2022.

[50] B. O. Guan, H. Y. Tam, and S. Y. Liu, “Temperature-Independent Fiber Bragg Grating Tilt Sensor,” *IEEE Photon. Technol. Lett.,* vol. 16, no. 1, pp. 224–226, 2004.

[51] B. Yun, N. Chen, and Y. Cui, “Highly sensitive liquid-level sensor based on etched fiber bragg grating,” *IEEE Photon. Technol. Lett.*, vol. 19, no. 21, pp. 1747–1749, 2007.

[52] H. Yu, X. Yang, Z. Tong, Y. Cao, and A. Zhang, “Temperature-independent rotational angle sensor based on fiber Bragg grating,” *IEEE Sens. J.,* vol. 11, no. 5, pp. 1233–1235, 2011.

[53] M. Liu, W. Wang, H. Song, S. Zhou, and W. Zhou, “A High Sensitivity FBG Strain Sensor Based on Flexible Hinge,” *Sensors*, vol. 19, no. 8, p. 1931, 2019.

[54] Afroozeh, “Highly Sensitive FBG-Based Sensor for Temperature Measurement Operating in Optical Fiber,” *Plasmonics,* vol. 16, no. 6, pp. 1973–1982, 2021.

[55] J. Thomas, T. R. Rajanna, and S. Asokan, “Temperature Compensated FBG Displacement Sensor for Long-Range Applications,” *IEEE Sensors Lett.,* vol. 4, no. 1, 2020.

[56] Sun, D. Zhao, W. Zhang, J. Li, and B. Shen, “A High-sensitivity FBG Accelerometer Based on a Bearing,” *J. Lightwave. Technol.,* vol. 40, no. 1, pp. 228–236, 2022.

[57] V. R. Pachava, S. Kamineni, S. S. Madhuvarasu, K. Putha, and V. R. Mamidi, "FBG based high sensitive pressure sensor and its low-cost interrogation system with enhanced resolution," *Photonic Sensors,* vol. 5, no. 4, pp. 321–329, 2015.

[58] Sengupta, M. Sai Shankar, P. Saidi Reddy, R. L. N. Sai Prasad, and K. Srimannarayana, "Sensing of hydrostatic pressure using FBG sensor for liquid level measurement," *Microw. Opt. Technol. Lett.,* vol. 54, no. 7, pp. 1679–1683, 2012.

[59] X. G. Tian and X. M. Tao, "Torsion measurement using fiber Bragg grating sensors," Appl. Opt. 41, 248–253, 2001.

[60] J. Y. Guo, B. Shi, M. Y. Sun, C. C. Zhang, G. Q. Wei, and J. Liu, "Characterization of an ORMOCER®-coated FBG sensor for relative humidity sensing," *Measurement,* vol. 171, p. 108851, 2021.

[61] J. Janting, J. K. M. Pedersen, G. Woyessa, K. Nielsen, and O. Bang, "Small and Robust All-Polymer Fiber Bragg Grating Based pH Sensor," *J. Lightwave. Technol.,* vol. 37, no. 18, pp. 4480–4486, 2019.

[62] S. Campopiano, A. Cutolo, A. Cusano, M. Giordano, G. Parente, G. Lanza and A. Laudati, "Underwater Acoustic Sensors Based on Fiber Bragg Gratings," *Sensors*, vol. 9, no. 6, pp. 4446–4454, 2009.

[63] W. Liang, Y. Huang, Y. Xu, R. K. Lee, and A. Yariv, "Highly sensitive fiber Bragg grating RI sensors," *Appl. Phys. Lett.,* vol. 86, no. 15, pp. 1–3, 2005.

[64] H. Y. Au, S. K. Khijwania, H. Y. Fu, W. H. Chung, and H. Y. Tam, "Temperature-insensitive fiber Bragg gratings based tilt sensor with large dynamic range," *J. Lightwave Technol.* 29, 1714–1720, 2011.

[65] D. Benz, T. Botzelmann, H. Kück, and D. Warkentin, "On low cost inclination sensors made from selectively metallized polymer," *Sens. Actuators A Phys.,* vol. 123–124, pp. 18–22, 2005.

[66] H. Jung, C. J. Kim, and S. H. Kong, "A MEMS-based electrolytic tilt sensor," *Proc. IEEE Sensors,* pp. 1199–1202, 2006.

[67] C. H. Lee and S. S. Lee, “Study of Capacitive Tilt Sensor with Metallic Ball,” *ETRI J.,* vol. 36, no. 3, pp. 361–366, 2014.

[68] Z. W. Zhong, L. P. Zhao, and H. H. Lin, “Development and investigation of an optical tilt sensor,” *Opt. Commun.,* vol. 261, no. 1, pp. 23–28, 2006.

[69] J. Ni and P. S. Huang, “Angle measurement based on the internal-reflection effect using elongated critical-angle prisms,” *Appl. Opt.*, vol. 35, no. 13, pp. 2239–2241, 1996.

[70] W. Zhou and L. Cai, “Interferometer for small-angle measurement based on total internal reflection,” *Appl. Opt.* vol. 37, no. 25, pp. 5957–5963, 1998.

[71] H. Fan, R. Ivan, and Z. P. Fang, “Novel optical sensor for precise tilt angle measurement,” *9th Int. Conf. Control. Autom. Robot. Vision*, ICARCV ’06, 2006.

[72] L. B. Yuan, “Push–pull fiber optic inclinometer based on a Mach–Zehnder optical low-coherence reflectometor,” *Rev. Sci. Instrum.,* vol. 75, no. 6, pp. 2013–2015, 2004.

[73] J. S. Bajić, D. Z. Stupar, L. M. Manojlović, M. P. Slankamenac, and M. B. Živanov, “A simple, low-cost, high-sensitivity fiber-optic tilt sensor,” *Sens. Actuators A Phys.,* vol. 185, pp. 33–38, 2012.

[74] B. O. Guan, H. Y. Tam, and S. Y. Liu, “Temperature-Independent Fiber Bragg Grating Tilt Sensor,” *IEEE Photon. Technol. Lett.,* vol. 16, no. 1, pp. 224–226, 2004.

[75] H. Bao, X. Dong, L. Y. Shao, C. L. Zhao, and S. Jin, “Temperature-insensitive 2-D tilt sensor by incorporating fiber Bragg gratings with a hybrid pendulum,” *Opt. Commun.* 283, 5021–5024, 2010.

[76] H. Bao, X. Dong, C. Zhao, L. Shao, C. C. Chan, and P. Shun, “Temperature-insensitive FBG tilt sensor with a large dynamic range,” *Opt. Commun.* 283, 968–970, 2010.

[77] R. Yang, H. Bao, S. Zhang, K. Ni, Y. Zheng, and X. Dong, “Simultaneous measurement of tilt angle and temperature with pendulum-based fiber bragg grating sensor,” *IEEE Sens. J.* 15, 6381–6384, 2015.

[78] X. Dong, C. Zhan, K. Hu, P. Shum, and C. C. Chan, “Temperature-Insensitive Tilt Sensor With Strain-Chirped Fiber Bragg Gratings,” *IEEE Photon. Technol. Lett.* 17, 2394-2396, 2005.

[79] K. Ni, X. Dong, Y. Jin, and H. Xu, “Temperature-independent fiber Bragg gratings tilt sensor,” *Microw. Opt. Technol. Lett.* 52, 2250–2252, 2010.

[80] H. J. Chen, L. Wang, and W. F. Liu, “Temperature-insensitive fiber Bragg grating tilt sensor,” *Appl. Opt.* Vol. 47, 556–560, 2008.

[81] K. Li, Y. Zhao, Y. Li, G. Liu, and J. Li, “Fiber Bragg grating biaxial tilt sensor using one optical fiber,” *Optik (Stuttg).* 218, 164973, 2020.

[82] R. Aneesh, Meeth Maharana, Pathi Munendhar, H. Y. Tam, and Sunil K. Khijwania, "Simple temperature insensitive fiber Bragg grating based tilt sensor with enhanced tunability," *Appl. Opt.* 50, E172-E176, 2011.

[83] P. Munendhar, R. Aneesh, and Sunil K. Khijwania, "Development of an all-optical temperature insensitive nonpendulum-type tilt sensor employing fiber Bragg gratings," *Appl. Opt.* 53, 3574-3580, 2014.

[84] C. A. R. Díaz, A. Leal-Junior, C. Marques, A. Frizera, M. J. Pontes, P. F. C. Anutunes, "Optical Fiber Sensing for Sub-Millimeter Liquid-Level Monitoring: A Review," *IEEE Sens. J.*, vol. 19, no. 17, 7179-7191, 2019.

[85] K. Loizou and E. Koutroulis, “Water level sensing: State of the art review and performance evaluation of a low-cost measurement system,” *Measurement*, vol. 89, pp. 204–214, 2016.

[86] R. He, C. Teng, S. Kumar, C. Marques, and R. Min, “Polymer Optical Fiber Liquid Level Sensor: A Review,” *IEEE Sens. J.*, vol. 22, no. 2, pp. 1081–1091, 2022.

[87] H. Canbolat, “A novel level measurement technique using tree capacitive sensors for liquids,” *IEEE Trans. Instrum. Meas.*, vol. 58, no. 10, pp. 3762–3768, 2009.

[88] F. Reverter, X. Li, and G. C. M. Meijer, “Liquid-level measurement system based on a remote grounded capacitive sensor,” *Sensors Actuators A Phys.*, vol. 138, no. 1, pp. 1–8, 2007.

[89] S. C. Bera, J. K. Ray, and S. Chattopadhyay, “A low-cost noncontact capacitance-type level transducer for a conducting liquid,” *IEEE Trans. Instrum. Meas.*, vol. 55, no. 3, pp. 778–786, 2006.

[90] R. M. A. Azzam, “Light-Reflection Liquid-Level Sensor,” *IEEE Trans. Instrum. Meas.*, vol. IM–29, no. 2, pp. 113–115, 1980.

[91] R. Nie, W. Guo, Y. Luo, W. Li, M. Xia, and K. Yang, “Optical liquid-level sensor based on a designed light guide plate,” *Sens. Actuator A Phys.*, vol. 296, pp. 352–356, 2019.

[92] M. Lomer, J. Arrue, C. Jauregui, P. Aiestaran, J. Zubia, and J. M. López-Higuera, “Lateral polishing of bends in plastic optical fibres applied to a multipoint liquid-level measurement sensor,” *Sens. Actuator A Phys.*, vol. 137, no. 1, pp. 68–73, 2007.

[93] P. Antunes, J. Dias, T. Paixão, E. Mesquita, H. Varum, and P. André, “Liquid level gauge based in plastic optical fiber,” *Measurement*, vol. 66, pp. 238–243, 2015.

[94] K. Iwamoto and I. Kamata, “Liquid-level sensor with optical fibers,” *Appl. Opt. Vol. 31, Issue 1, pp. 51-54*, vol. 31, no. 1, pp. 51–54, 1992.

[95] N. Jing, C. Teng, J. Zheng, G. Wang, Y. Chen, and Z. Wang, “A liquid level sensor based on a race-track helical plastic optical fiber,” *IEEE Photonics Technol. Lett.*, vol. 29, no. 1, pp. 158–160, 2017.

[96] X. Zhang, W. Peng, Z. Liu, and Z. Gong, “Fiber Optic Liquid Level Sensor Based on Integration of Lever Principle and Optical Interferometry,” *IEEE Photonics J.*, vol. 6, no. 2, 2014.

[97] B. Dong, Q. Zhao, F. Lvjun, T. Guo, L. Xue, S. Li and H. Gu, “Liquid-level sensor with a high-birefringence-fiber loop mirror,” *Appl. Opt. Vol. 45, Issue 30, pp. 7767-7771*, vol. 45, no. 30, pp. 7767–7771, 2006.

[98] H. Gong, H. Song, S. Zhang, K. Ni, and X. Dong, “An optical liquid level sensor based on polarization-maintaining fiber modal interferometer,” *Sens. Actuators A Phys.*, vol. 205, pp. 204–207, 2014.

[99] W. Wang and F. Li, “Large-range liquid level sensor based on an optical fibre extrinsic Fabry–Perot interferometer,” *Opt. Lasers Eng.*, vol. 52, no. 1, pp. 201–205, 2014.

[100] T. Guo, Q. Zhao, Q Dou, H. Zhang, L. Xue, G. Huang and X Dong, “Temperature-insensitive fiber Bragg grating liquid-level sensor based on bending cantilever beam,” *IEEE Photonics Technol. Lett.*, vol. 17, no. 11, pp. 2400–2402, 2005.

[101] C. W. Lai, Y. L. Lo, J. P. Yur, and C. H. Chuang, "Application of Fiber Bragg Grating Level Sensor and Fabry-Pérot Pressure Sensor to Simultaneous Measurement of Liquid Level and Specific Gravity,” *IEEE Sensors J.*, vol. 12, no. 4, pp. 827-831, 2012

[102] K. R. Sohn and J. H. Shim, “Liquid-level monitoring sensor systems using fiber Bragg grating embedded in cantilever,” *Sens. Actuators A Phys.*, vol. 152, no. 2, pp. 248–251, 2009.

[103] H. J. Sheng, W. F. Liu, S. S. Bor, and H. C. Chang, “Fiber-liquid-level sensor based on a fiber bragg grating,” *Jpn. J. Appl. Phys.*, vol. 47, no. 4 PART 1, pp. 2141–2143, 2008.

[104] G. G. De Almeida, R. C. Barreto, K. F. Seidel, and R. C. Kamikawachi, “A Fiber Bragg Grating Water Level Sensor Based on the Force of Buoyancy,” *IEEE Sensors J.*, vol. 20, no. 7, pp. 3608–3613, 2020.

[105] Q. Jiang, D. Hu, and M. Yang, “Simultaneous measurement of liquid level and surrounding RI using tilted fiber Bragg grating,” *Sens. Actuators A Phys.*, vol. 170, no. 1–2, pp. 62–65, 2011.

[106] C. Mou, K. Zhou, Z. Yan, H. Fu, and L. Zhang, “Liquid level sensor based on an excessively tilted fibre grating,” *Opt. Commun.*, vol. 305, pp. 271–275, 2013.

[107] T. Osuch, T. Jurek, K. Markowski, and K. Jedrzejewski, “Simultaneous Measurement of Liquid Level and Temperature Using Tilted Fiber Bragg Grating,” *IEEE Sensors J.*, vol. 16, no. 5, pp. 1205–1209, 2016.

[108] H. Fu, X. Shu, A. Zhang, W. Liu, L. Zhang, S. He and I. Bennion, “Implementation and characterization of liquid-level sensor based on a long-period fiber grating MachZehnder interferometer,” *IEEE Sens. J.*, vol. 11, no. 11, pp. 2878–2882, 2011.

[109] S. W. James, S. Khaliq, and R. P. Tatam, “Fiber-optic liquid-level sensor using a long-period grating,” *Opt. Lett. Vol. 26, Issue 16, pp. 1224-1226*, vol. 26, no. 16, pp. 1224–1226, 2001.

[110] H. C. Hesse, “Optical fiber chemical sensor”, East German patent 106086, 1974.

[111] F. T. S. Yu and S. Yin, “Fiber Optic Sensors”, *Marcel Dekker*, 2002.

[112] P. S. J. Russell, J.L. Archambault, and L. Reekie, “Fibre gratings,” *Phys. World*, vol. 6, no. 10, pp. 41–48, 1993.

[113] M. Monerie, “Propagation in Doubly Clad Single-Mode Fibers,” IEEE Trans. *Microw. Theory Tech.,* vol. 30, no. 4, pp. 381–388, 1982

[114] [Online]. Available: http://www.microsensorcorp.com/

[115] R. E. Vermillion, “Derivations of Archimedes’ principle,” *Am. J. Phys.*, vol. 59, no. 8, pp. 761–762, 1991.

[116] J. Hannah and M. J. Hillier, *Appl. Mech.*, 3rd ed. London, U.K: Pearson Education, 1995.

[117] Corning SMF-28e+ Optical Fiber Datasheet. [Online]. Available: https://wwww.corning.com/media/worldwide/coc/documents/PI1463_07-14_English.pdf